An Experimental Study of Volcanic Tremor Driven by Magma Wagging

by

Vahid Dehghanniri

BSc, University of Tehran, 2010

MSc, K.N. Toosi University of Technology, 2013

A THESIS SUBMITTED IN PARTIAL FULFILLMENT OF THE REQUIREMENTS FOR THE DEGREE OF

Master of Science

in

THE FACULTY OF GRADUATE AND POSTDOCTORAL STUDIES

(Geophysics)

The University of British Columbia

(Vancouver)

January 2020

The following individuals certify that they have read, and recommend to the Faculty of Graduate and Postdoctoral Studies for acceptance, the thesis entitled:

An Experimental Study of Volcanic Tremor Driven by Magma Wagging

submitted by **Vahid Dehghanniri** in partial fulfillment of the requirements for the degree of **Master of Science** in **Geophysics**.

Examining Committee:

A. Mark Jellinek
Supervisor

Kelly Russell
Supervisory Committee Member

Valentina Radic
Supervisory Committee Member

Ali Ameli
Additional Examiner

Abstract

Pre-eruptive seismic tremor with similar spectral properties is observed at active volcanoes with widely ranging conduit geometries and structures. Accordingly, the "magma wagging" model introduced by Jellinek & Bercovici[21] and extended by Bercovici et al.[6] hypothesizes an underlying mechanism that is only weakly-sensitive to volcano architecture: Within active volcanic conduits, the flow of gas through a permeable foamy annulus of gas bubbles excites and maintains an oscillation of a central magma column through a well-known Bernoulli effect. In this thesis, we carry out a critical experimental test of this underlying mechanism for excitation. We explore the response of analog columns with prescribed elastic and linear damping properties to forced air annular airflows. From high speed video measurements of linear and orbital displacements and time series of accelerometer measurements we characterize and understand the excitation, evolution, and steady-state oscillating behaviors of analog magma columns over a broad range of conditions. We identify three distinct classes of wagging: **i**. rotational modes which confirms predictions for whirling modes by Liao et al.[26]; as well as newly-identified **ii**. mixed-mode; and **iii**. chaotic modes. We find that rotational modes are favored for symmetric, and high intensity forcing. Mixed-mode responses are favored for a symmetric and intermediate intensity forcing. Chaotic modes occur in asymmetric or low intensity forcing. To confirm and better understand our laboratory results, and also extend them to conditions beyond what is possible in the laboratory, we carry out complementary two-dimensional simulations of our analog experiments.

Our combined experimental and numerical results can be applied to make

qualitative predictions for natural testable in future studies of pre- and syn-eruptive volcano seismicity. Long before an eruptive phase, the total gas flux is low and we expect magma wagging in a chaotic mode, independent of the spatial distribution of the gas flux. At a pre-eruptive state signaled by gas flux increasing, if the distribution of gas flux is approximately symmetric, we expect a transition to mixed and possibly rotational wagging modes. During an eruption, fragmentation and explosions within the foamy annulus can cause spatial heterogeneity in permeability resulting in non-uniform gas flux that favors chaotic wagging behavior.

Lay Summary

Volcanic tremor with a period of about 1 s is a common feature of most explosive eruptions and a major component of volcanic forecasting algorithms. "Magma wagging" model predicts that a column of magma can oscillate within a thin annular layer of foamy magma in a volcanic conduit, producing the observed seismic phenomena. Differential gas flow through this foamy annulus gives rise to pressure forces that drive and maintain this oscillation continuously over hours to months. In this thesis, we use experiments and numerical simulations to confirm the basic wagging phenomena. We identify new classes of magma column oscillation, depending of the intensity and distribution of gas flows through the annulus. Our results predict an evolution in the character and spatial correlation of tremor properties that can be applied to eruption forecasting.

Preface

Chapter 1. Figures 1.2, 1.4, 1.5, 1.6, 1.7, 1.9, 1.10, 1.12, and 1.13 are used with permission from applicable sources.

This thesis is ultimately based on the experimental apparatus and numerical modeling. The hardware design in Chapter 2 was done primarily by M. Jellinek and myself. The construction and tests were performed by S. Tomassi and I. The data analysis in Chapter 2 and Chapter 3 and numerical modeling in Chapter 4 are my original work.

A version of this material has been disseminated in form of poster presentation at 27th International Union of Geodesy and Geophysics Conference, Montreal, Canada

Table of Contents

List of Tables

List of Figures

Acknowledgments

First and foremost, I would like to express my sincere gratitude and appreciation to my mentor and supervisor Prof. Mark Jellinek. Mark thanks for being so patient toward my painfully-naive questions. Thanks for guiding me to become a scientist and importantly being so knowledgeable and caring.

I would also like to thank the members of my advisory committee: Prof. Kelly Russell and Prof. Valentina Radic. Kelly! thanks for introducing the beautiful world of volcanoes to me. Valentina! thanks for showing me how to create something meaningful out of big bunch of data.

I would also like to thank Jorn Unger and Santiago Tomassi. Every time I had a problem with the experimental setup I came to Jorn and he helped me patiently. Santiago, Thanks for helping me to run more than 1000 experiments.

I would also like to thank my wonderful lab-mates in MJCJ research group for making my graduate life more enjoyable and fun.

I am especially grateful to my parents. I thank them for their endless support and unconditional love. This journey could have not been possible without their support. I also thank my siblings for encouraging me to follow my passion. I am thankful to all of them and forever grateful for having them in my life.

I would also like to thank my beautiful wife, Parisa. If it was not for you, I would not stand at this point.

Last but certainly not least, Id like to thank my new family for supporting me every step of the way.

Dedication

To my parents

for their unconditional love

Chapter 1

Introduction

Violent volcanic eruptions such as the $1980-86$ Mount Saint Helens event [12], the 1991 eruption of Mount Pinatubo [19], the $1995-2013$ eruption of Soufriere Hills [38], or the 2010 Eyjafjallajkull [17] event can be devastating to local populations and can disrupt air travel with profound economic consequences felt worldwide. With the current steady rise in the populations of cities on the flanks of active volcanoes and a growing reliance on international air travel to support an ever-increasing global economy, the need to reliably forecast catastrophic eruptions is paramount.

The rest of this chapter is organized as follows. We initially introduce volcanic tremors as a promising indicator of a volcanic eruption. Next, we briefly discuss existing models of the source mechanism of volcanic tremors and explain the reason that a universal model is needed. Later we explore the recently proposed "magma wagging" model and discuss main phenomena that magma wagging predicts carefully. Then, we address some of the cavities in the literature of magma wagging and knowledge gaps that are needed to be studied, and finally, we present our method to study magma wagging theory and improve it.

1.1 Volcanic tremor

An important tool for establishing dangerous impending volcanic unrest is monitoring of the volcanos seismic activity. A particular type of seismic activity called volcanic tremor almost always precedes the explosive volcanic eruptions that present the greatest danger to humans. Tremors persists for minutes to weeks and its seismic waveforms are characterized by a remarkably narrow band of frequencies from about 0.5 Hz to 7 Hz [24, 28, 29, 31]. Before major eruptions, tremor can occur in concert with increased gas flux and related ground deformation [12, 27, 35]. Tremor frequency can vary in time. An intriguing feature of tremor observed at several eruptions is "gliding" within the frequencies of evenly spaced spectral peaks vary systematically with time [20, 28] (see Fig. 1.1). McNutt and Nishimura [29] also show that around 90% of volcanic tremor decay exponentially at the end of eruptions. Also, some studies use volcanic tremor to estimate the Volcanic Explosivity Index (VEI), a numeric scale that measures the relative explosivity of eruptions, of eruption while it is in progress [1]. Consequently, volcanic tremor forms a major component of eruption forecasting algorithms [7, 35], and understanding its origin might be a great help to forecast explosive eruptions.

1.2 Volcanic tremor source mechanism

Although tremor is an empirically useful indicator of imminent volcanism, a clear understanding of the underlying physical process is elusive. Several studies indicate that volcanic tremors have a common excitation mechanism with a source that is repeatable, non-destructive, and at a fixed location [31]. Benoit & McNutt [5] have shown evidence of changing apparent source location in space and suggest that tremor source is linear in shape rather than a point source. Unglert and Jellinek [37] identify three main classes of volcanic tremor and discuss that there should be a generic relationship between spectral character and magma volcano characteristics, including magma viscosity, magma storage depth, and the physical properties of volcano edifices.

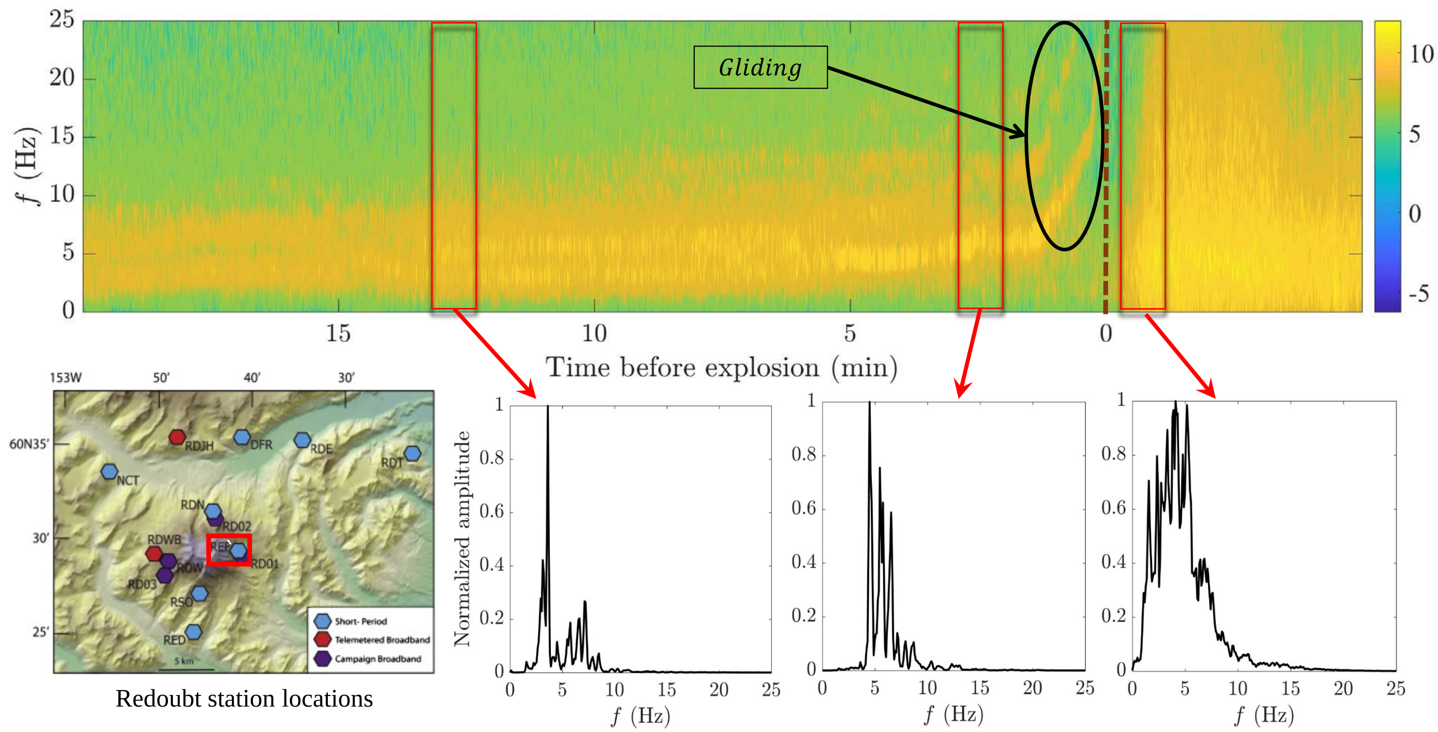

Figure 1.1: Time series of amplitude spectra prior to eruption on $2009 - March - 28\ 03 : 24$ at station REF, to the east of Redoubt Volcano [20]. The spectrogram is plotted on a common logarithmic color scale using a 2-second 50% overlapping window. Time is aligned to the approximate explosion onset at $t = 0$, and frequency is plotted up to the broadband Nyquist frequency of 25 Hz. Tremor during transitions from background volcanic unrest to eruption begins as a harmonic or nearly monochromatic ('narrow-band') signal. As the eruption progress, both the maximum frequency and the total signal bandwidth increase to become 'broadband'. Tremor gliding can be observed in the last three minutes prior to eruption.

1.2.1 Previously proposed mechanisms

Several models exist to explain aspects of the spectral properties volcanic tremor source mechanisms. For example, tremor can be a continuous oscillation that reflects either a natural mode of vibration excited in the volcanic conduit, analogous to an organ pipes response to airflow [10, 16]. Alternatively, tremors are caused by the elastic response of existing cracks to magma flow, i.e., the rapid opening and closing of fractures or "crack flapping" [7, 34]. Hellweg et al. [18] also propose an "eddy shedding" model in which conduit wall reaction to pressure fluctuations caused by eddies, which form behind obstacles, lead to volcanic tremor. "Pressure-cooker" and "soda-bottle" models [18, 22] explain periodic degassing and periodic ash release controlled by some valve mechanism might be a tremor cause. Other proposed tremor mechanisms include magma and water interactions, bubble growth and collapse in magma or water [25], and resonance of magma body under the ground [9]. All of these models explain the monochromatic properties of tremor frequency.

These approaches to understanding tremor focus only on the oscillation and do not address time-dependent properties of frequency or amplitude of tremor. Also, they involve very different physical phenomena. Furthermore, their success relies on an unrealistic assumption that all volcanoes worldwide are similar in terms of the geometry, structure, and constitution of volcanic conduit walls, as well as the gas content of the erupting magma. In addition to the initial mechanical structure of volcanic conduits being distinct, the evolutions of the magma-conduit system during eruptions will be different from one volcano to the next. Ultimately, it is surprising that tremor characteristics are so consistent among volcanoes worldwide, and the universality of tremor properties particularly related to explosive volcanism remains, thus, a major enigma[21].

1.3 Magma wagging theory

In a departure from the conventional focus on the geometric and structural properties of volcanic conduits to explain the physical process behind tremor, recent studies show that volcanic tremor may be a natural consequence of the flow dynamics of an ascending magma. The so-called "magma wagging" theory is proposed in [21], which employs the contemporary view of silicic volcanic systems that ascending viscous magmas with high concentrations of crystals and bubbles form a stiff columnar plug surrounded by a compressible layer of sheared foam (Fig. 1.2).

1.3.1 Magma wagging mechanism

In silicic eruptions, involving high viscosity magma, ascent speeds of gas bubbles are negligible compared with the rise speed of magma [35]. As a result, magma rises as a gas- and crystal-rich plug before and sometimes during an eruption. Shearing at the conduit causes bubbles, which have a much lower viscosity than the surrounding melt phase, to stretch, merge, and become interconnected [6]. Consequently, a vesicular, permeable, and compressible annulus of bubbly magma forms around the magma plug. Models [13, 32, 33, 35] as well as some observations of pumice with porosity ϕ_0 of $30 - 90\%$ from effusive and explosive eruptions represents of permeable tube-like matrix within the annulus [13, 35], see Fig. 1.2.

For most geologically-relevant conditions, the stiff magma column that is connected to a magma reservoir below and has an upper free surface will oscillate or "wag" laterally or azimuthally against a restoring gas-spring force of the compressible foam layer. When the magma column is displaced from its central resting position, the annulus is compressed in the direction of column displacement and is decompressed in the other direction. Through the ideal gas law, there will be net pressure force originated from permeable foamy-springy annulus pushing back the column toward its resting position, provided that the column displacement occurs over a time scale that is small compared to the time for compressed gas to drain by porous media flow. The columns inertia causes it to overshoot the resting position during an oscillation. Following an initial displacement, the column oscillates inside the annulus until viscous forces in the magma column damp it. Pressure forces imparted at conduit walls result in seismic energy being transmitted through

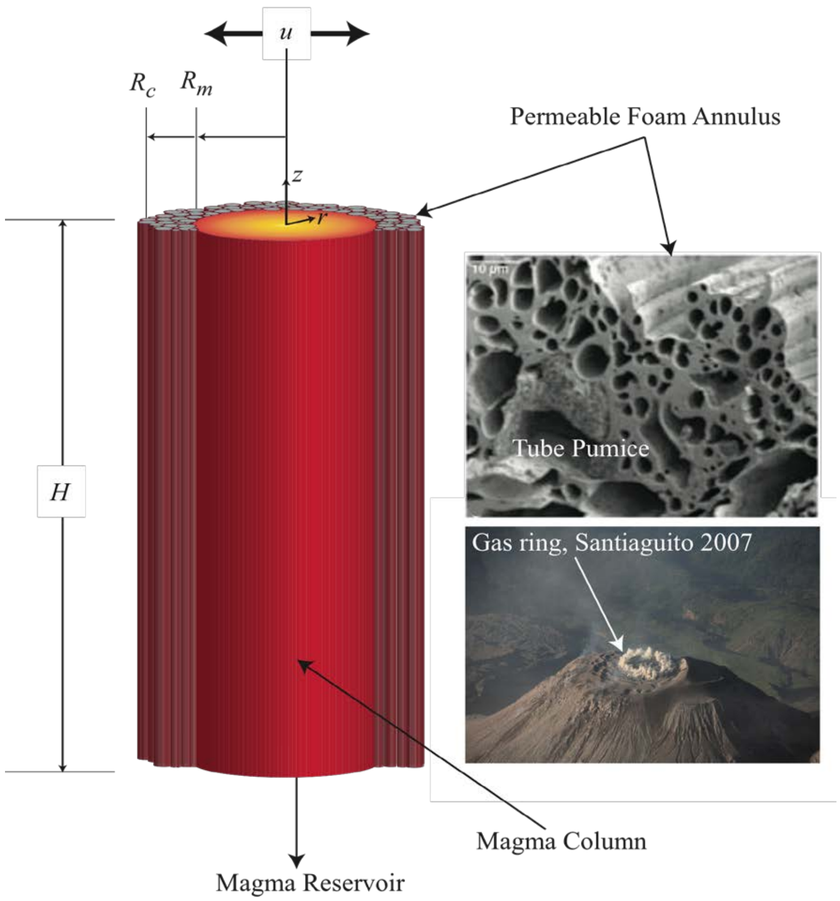

Figure 1.2: From [21] with permission. Sketch of the magma wagging model for volcanic tremor. Left panel: a very viscous magma column of radius R_m in a volcanic conduit of radius R_c is surrounded by a compressible permeable foam annulus. The annulus is composed of stretched and coalesced bubbles forming a tube-like matrix. Top right panel: an example of observed tube-like pumice [23]. Bottom right panel: an example of the observed gas ring at the edge of Santiaguito volcano, which suggests the permeable foam annulus. The depth H is typically of order 1 km [8, 15].

the conduit walls surrounding the wagging magma column and leading to the tremor signal observed on local seismic stations [6, 21].

1.3.2 2D magma wagging with an impermeable annulus

In the original model, Jellinek & Bercovici [21] make five simplifications. First, they assume that bubble- and crystal-rich magma, and the surrounding annulus foam layer rise together. Second, they assume that inner column of magma of radius R_m is cylindrically axisymmetric and initially at rest and centered inside a cylindrical conduit of radius R_c. Thus, the resting gap between the conduit wall and the inner column is $L = R_c - R_m$. Third, to facilitate analysis, they define the (linear) column instability to lateral displacements in polar coordinates such that when a column is displaced left or right by $u(z)$, the maximum gap width is $L + u$ and the minimum gap width is $L - u$ (see Fig. 1.3). Fourth, the annulus is assumed to be impermeable. Fifth, they neglect the elastic behavior of the column itself as the maxwell relaxation time is $\ll 10^{-1}$ s, for rhyolitic magmas with viscosities of $10^5 - 10^9$ Pa and shear moduli in the range of $10^{10} - 10^{11}$ Pa [2], is shorter than typical periods of volcanic tremor.

With these assumptions, the original equation of motion governing wagging is akin to that for a linearly damped harmonic oscillator [21]:

$$\frac{\partial^2 \vec{u}}{\partial t^2} = -\omega_0^2 \vec{u} + \nu_m \frac{\partial^3 \vec{u}}{\partial z^2 \partial t}, \tag{1.1}$$

where $\vec{u}$ is the displacement from column resting position, ν_m is the magma kinematic viscosity, z is the vertical direction along with the column height. The natural angular frequency [rad/s] of the wagging magma column ω_0 depends on a balance between gas pressure-force (the spring force) and the columns inertia and is:

$$\omega_0 = \sqrt{\frac{2\rho_0 C^2}{\phi_0 \rho_m (R_c^2 - R_m^2)}}, \tag{1.2}$$

where the ordinary frequency [Hz] is $\omega_0/2\pi$. Here C is the speed of sound

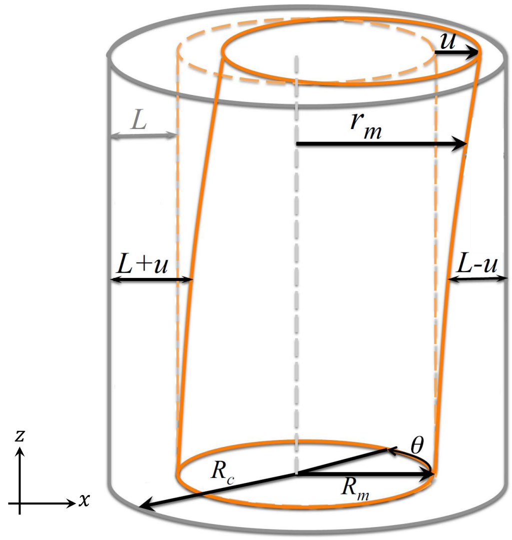

Figure 1.3: Sketch of 2D impermeable magma wagging model of volcanic tremor showing an initial displacement to the right. The column is assumed to have a free surface at the top and is coupled viscously to the magma system below. Assumed impermeable annulus prevents gas to rise relative to annulus and plug of magma. Variables displaced in the diagram are discussed in the accompanying text.

in gas (water vapor at magmatic temperature), ρ_0 and ϕ_0 are the density and volume fraction of the undisturbed gas in the annulus, ρ_m is the magma density, and R_c and R_m are the conduit and magma column radii, respectively. The left-hand side of (1.1) represents column acceleration. While on the right-hand side, the first term is the acceleration related to the restoring foam spring force in the annulus, and the second term is the deceleration arising in response to the production of vertical velocity gradient in the magma column as a result of viscous bending and wagging.

The fundamental frequency of wagging (1.2) implies that increasing bubble volume fraction ϕ_0 in the annulus decreases wagging frequency ($\omega_0 \propto \sqrt{1/\phi_0}$). Also, decreasing the column radius R_m for fixed R_c causes the wagging frequency to decrease ($\omega_0 \propto \sqrt{1/(R_c^2 - R_m^2)}$). Critically and in marked contrast to all other tremor models, ω_0 is only very weakly sensitive to conduit geometry through equation 1.2. Furthermore, this behavior leads to an important prediction consistent with Fig. 1.1. InSAR monitoring [27] as well as seismic data [11] show that volcanos gas-pressurize prior to eruption. The cause of volcano pressurization is increased gas content inside the magma. A resulting increase in the bubble concentration in the foamy annulus reduces magma viscosity locally and enhances the localization of shear deformation near the conduit walls [15], which leads to a narrower annulus, in turn. This progressive narrowing of the annulus width, $L = R_c - R_m$, causes the wagging frequency to climb.

All the variables in equation 1.2 are well constrained except the conduit geometry. Jellinek & Bercovici [21] show that using $C = 700$ m/s for a gas which is primarily water at about 1000 K, $\rho_m/\rho_0 = 100$, $30\% < \phi_0 < 90\%$, 10 m$\leq R_c \leq 100$ m, and $0.5 \leq R_m/R_c < 1$ the frequency of oscillation ranges from 0.1 Hz to 5 Hz which is in the range of known volcanic tremors. Figure 1.4 shows wagging ordinary frequency $\omega_0/2\pi$ [Hz] on the left y-axis (solid lines) and shear strain rate in the annulus on the right y-axis (dashed lines) versus annulus thickness on x-axis for several conduit radii. Wider columns wag in lower frequencies because of greater inertia forces they have.

Figure 1.4 also shows the evolution in shear strain rate as annulus thickness L decrease with increased gas concentration. The shear strain rate cannot increase to infinity: Eventually, the shear strain rate reaches a maximum at which the time scale for the accumulation of shear strain becomes shorter than time scale for viscoelastic relaxation of bubble walls, and sheared bubbles rupture catastrophically and fragment [15, 36]. Thus, fragmentation is associated with a minimum annulus thickness and maximum frequency. The solid black line in Fig. 1.4 represents the threshold for fragmentation, and arrows correspond to minimum annulus thickness and maximum tremor frequency.

Fragmentation is envisioned to cause the annulus to evolve rapidly from a foam composed of tube-like bubbles with a homogeneous, on average, permeability to a mixture of fractured tubes and shattered glass fragments with a permeability that is spatially heterogeneous [21]. A strong heterogeneity

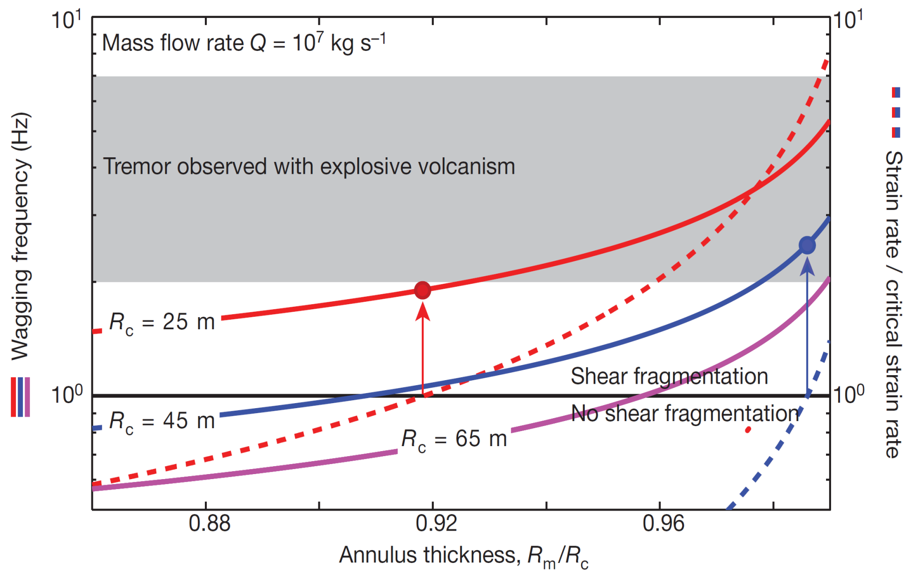

Figure 1.4: From [21] with permission. Wagging frequency and shear strain rate versus annulus thickness R_m/R_c for several conduit radii R_c. Wagging frequency is calculated using equation 1.2. Strain rate is $(Q/(\rho_m \pi R_c^2))/(R_c - R_m)$ and the critical strain rate is (cG/μ_m), where Q is a typical mass flow rate, G is the shear modulus of the melt, and c is a geometric constant. For more information see Fig. 3 in [21].

into the structure of the annulus causes gas volume fraction ϕ_0 in the annulus to vary in space [21], causing a broadening of the wagging frequency bandwidth because $\omega_0 \propto \sqrt{1/\phi_0}$.

1.3.3 2D magma wagging with a permeable annulus and gas flux variations

Because the viscous resistance of the magma column to bending, $(\nu_m \frac{\partial^3 \vec{u}}{\partial z^2 \partial t})$ in equation 1.1, will attenuate the oscillation over timescales as short as hours [6, 21], a driving mechanism to maintain the oscillation is necessary. Bercovici et al. [6] develop a hypothesis that the magma wagging model is a continuously self-excited system. They extend the magma wagging model to include a permeable annulus, which allows gas to move relative to magma and bubbles in the annulus (see Fig. 1.5) and allows for left-right variations in gas flux.

When the column is displaced, in the direction of displacement gas pressure increases and imposes a pressure force to restore the column displacement. At the same time, rise speed of compressed gas in the annulus increases through a nozzle effect. This increase in velocity on the compressed side causes a pressure drop which draws the column further in the direction of displacement through the well-known Bernoulli effect. In contrast, gas decompresses in the opposite direction, its pressure decreases and lead to a pressure force to oppose the column displacement. At the same time, rise speed of decompressed gas in the annulus decreases. This decrease in velocity on the decompressed side cause a pressure increase which draws the column further in the direction of displacement. Therefore, differential gas ascent speeds in annulus will induce lateral pressure variations that can excite relatively low frequency "Bernoulli mode" that potentially supplies energy to higher frequency wagging.

In more detail, as with the original model, Bercovici et al. [6] restrict wagging to be in 2D, in the $x-z$ plane in Fig. 1.3. Thus, when the column is displaced by $u(z)$ the maximum gap width is $L+u$, and the minimum gap width is $L-u$. They consider gas flow in the annulus is driven both by gas injected from below and modulated by left-right pressure variations arising from lateral displacement of the magma column. They also consider that the gas density, annulus porosity, and gas velocity are independent of radial distance r from the center of the conduit.

The greatest physical insight into 2D magma wagging model with permeable annulus is via the the equations of mass and momentum conservation in dimensionless form:

$$\frac{\partial \rho\varphi}{\partial t} + \frac{\partial \rho\varphi w}{\partial z} = 0, \tag{1.3}$$

$$\rho\phi(\frac{\partial w}{\partial t} + w\frac{\partial w}{\partial z}) = -\frac{\partial \rho}{\partial z} - \gamma(\beta(1-\phi) + \rho\phi), \tag{1.4}$$

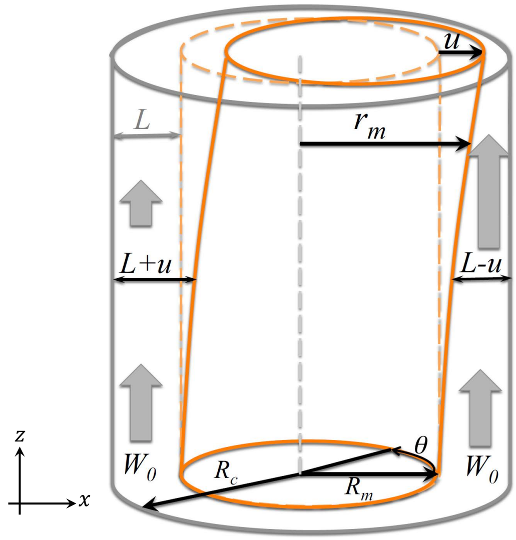

Figure 1.5: From [6] with permission. Sketch of the cylindrical annulus for the permeable magma wagging model showing a displacement to the right. An important different to Fig. 1.3 is that this displacement is driven as a result of a pressure difference from left to right related to higher gas speed on the right side (the Bernoulli's effect). The column is assumed to have a free surface at the top and is coupled viscously to the magma system below. Variables displaced in the diagram are discussed in the accompanying text.

$$\frac{\partial^2 u}{\partial t^2} = -\frac{2\lambda}{\beta\pi}\int_0^{2\pi} \rho(cos\theta + 2\lambda u\ cos(2\theta))d\theta + \eta\frac{\partial^3 u}{\partial z^2 \partial t}, \tag{1.5}$$

where

$$\varphi = \phi_0 - u\ cos\theta \qquad \text{and} \qquad \phi = \phi_0 - (1-\phi_0)u\ cos\theta,$$

and the dimensionless control parameters are:

$$\gamma = \frac{gU}{C^2},\ \beta = \frac{\rho_m}{\rho_o},\ \eta = \frac{\nu_m}{CU} \quad \text{and} \quad \lambda = \frac{U}{2R_m}, \tag{1.6}$$

where $U = (R_c^2 - R_m^2)/2R_m$ and $U \approx L$ in the limit of $L \ll R_c$. Hence,

γ represents the ratio of hydrostatic and dynamic gas pressure, β is the ratio of magma and gas densities, λ expresses the annulus thickness to the magma column width, and the most important, η represents the ratio of viscous forces arising in the magma column, depending on the rate of displacement, to the gas spring force in the annulus. Alternatively, η is the ratio of time scale to build up elastic spring forces U/C to the time scale of damp oscillations through viscous effects U^2/ν_m.

To understand the response of magma column to lateral pressure variations arising in response to gas flux variations, Bercovici et al. [6] investigate the linear and nonlinear stabilities of the 2D Cartesian magma wagging model (equations 1.3-1.5) analytically and numerically, respectively. At linear order displacement u, gas velocity w, and density ρ all scale as e^{ikz+st}, where k is wavelength and s is the growth rate of a small perturbation. They find the characteristics equation:

$$s^2 + \frac{\phi_0 \alpha^2 (s + ikM)^2}{k^2 + \phi_0 (s + ikM)^2} + \eta k^2 s = 0, \tag{1.7}$$

where $\alpha = 2\lambda/(\phi_0 \beta)$ and $M = W_0/C$ is gas injection Mach number. The unstable mode happens where $k \to \infty$ and where s is independent of k. In this case

$$s \approx \frac{\phi_0 \alpha^2 M^2}{\eta(1 - \phi_0 M^2)k^2} \tag{1.8}$$

and corresponds to a growing perturbation with a weak oscillation. This instability is associated with Bernoulli driving effect as growth rate depends on the square of gas injection speed M^2, which in turn governs dynamic pressure variations in gas that scale as ρw^2. Figure 1.6 shows oscillations in displacement of the top of the magma column for various values of M, λ and η. The oscillations are the superposition of two modes: **i**. initial dominant high frequency oscillation and **ii**. most unstable long period mode. For moderate Mach number $M = 0.1$, the high-frequency oscillations are dominant for a period of time and eventually exponential growth of the low-frequency oscillations becomes significant. But as M is increased, the low frequency oscillations grow faster before many of the high-frequency oscillations can

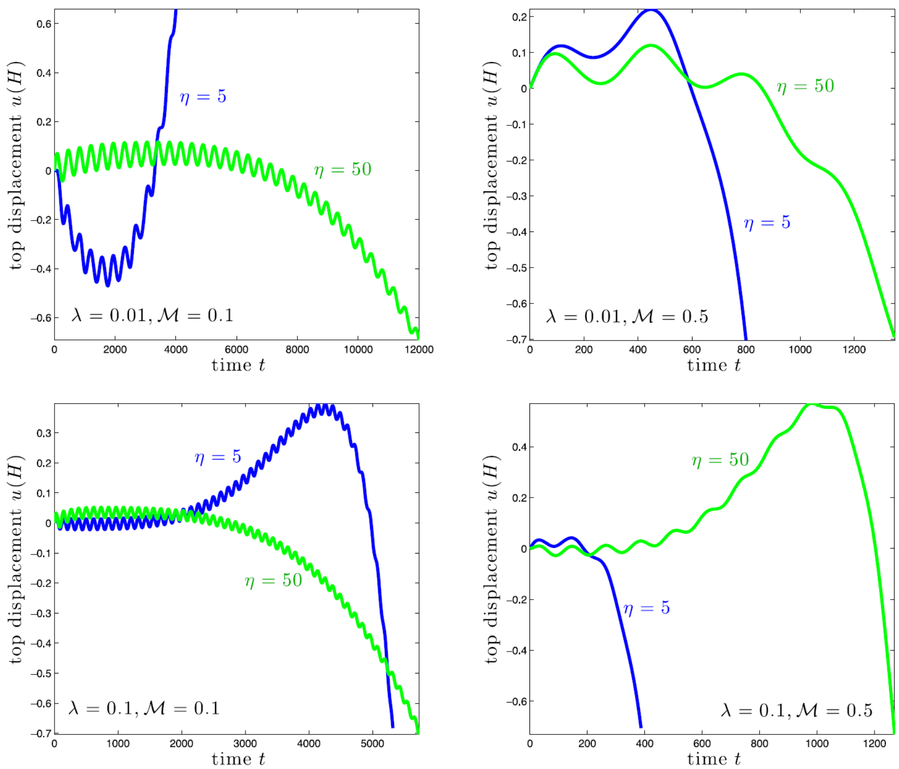

Figure 1.6: From [6] with permission. Oscillations in displacement u of the magma column at the column top, as predicted by the linear stability analysis. The oscillations are the superposition of only two modes, the fundamental mode and the least stable mode. Figures shown are for various values of M, λ and η as indicated. All frames have the same values of $\phi_0 = 0.7$, $\beta = 100$ and $\gamma = 0$.

occur.

Non-linear wagging stability analysis is investigated in [6] for various parameters, e.g. different gas flux injections and Mach numbers, by the same approach as linear analysis. The study [6] leads to qualitatively similar results as the linear stability analysis. They show depending on the parameters, the oscillation damping can be slow or moderately fast. As an example, Fig. 1.7 shows the top displacement of the column for different

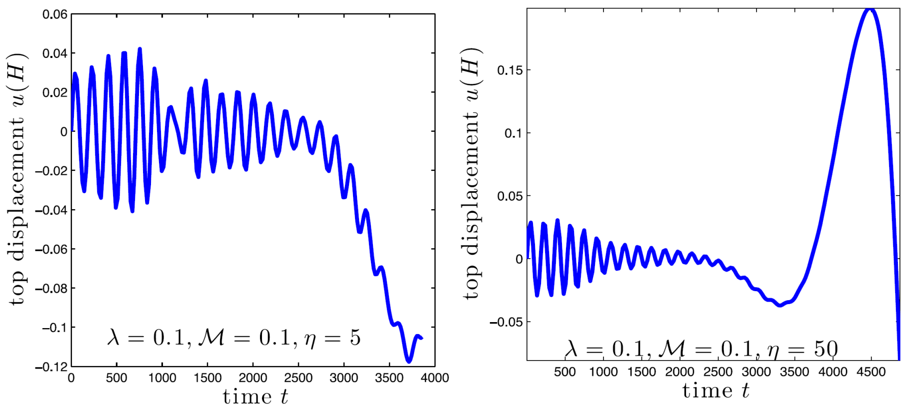

Figure 1.7: From [6] with permission. Oscillations in displacement u of the magma column at the column top, as predicted by the non-linear stability analysis. The oscillations are the superposition of only two modes, the fundamental mode and the least stable mode. Figures shown are for various values of M, λ and η as indicated. Both frames have the same values of $\beta = 100$ and $\gamma = 2 \times 10^{-5}$.

values of η, $\eta = 5,\ 50$. Higher η results in faster decay of high-frequency oscillations.

Observations of correlated tremor and gas flux variations show that short-period pulses in gas flux are nearly synchronous with tremors as audible chugging [5, 22] and longer-period signals of average tremor amplitude and gas flux are correlated with a nearly a minute lag [30] (see Figs. 1.8 and 1.9). Bercovici et al. [6] show that short-period pulses are due to density oscillations related to oscillations in column displacement since they provide the restoring force for the column wagging. Also, longer-period signals correspond to the Bernoulli effect of gas flux through the annulus at the end of the growing instability, which provides the driving mechanism to keep the tremor excited for long periods of time, see Fig. 1.6.

Figure 1.8 also shows the growing sequence of beating envelopes of tremor. Bercovici et al. [6] suggest that the addition of harmonics of oscillation causes these envelopes. "Non-linear interactions between oscillations

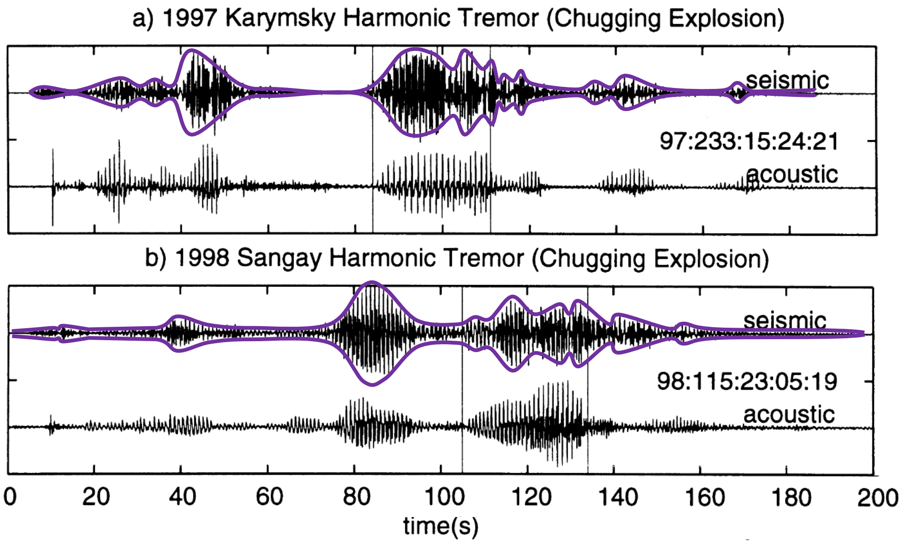

Figure 1.8: Seismic and Acoustic time series for Karymsky and Sangay volcanoes [22] show growing sequence of beating envelopes of tremor as well as correlated tremor and gas flux variations (acoustic time series).

of a given frequency lead to cascading of energy to higher harmonics, and given the presence of both odd and even non-linearities, all harmonics (both even and odd) are excited" [6]. The envelop structures are a superposition of these close frequencies/harmonics, and the intervals between these envelopes correspond to growth time for the unstable low frequency/Bernoulli mode, see Fig. 1.10.

When the magma column is displaced from its resting position, resulting gas pressure variations within the annulus are imparted to conduit walls and transmitted to seismometers. Two dimensional (linear) wagging is, thus, predicted to produce tremor signals on opposite sides of vent that are about 1/2 cycle out of phase. It generates compressive ground motion at the direction of displacement and tensile ground motion on the opposite side. The sign of ground motion around the volcanic vent will be reversed at half a period of oscillation later. Bercovici et al. [6] suggested that ground motion on opposite sides of a volcano should be spatially and temporally correlated.

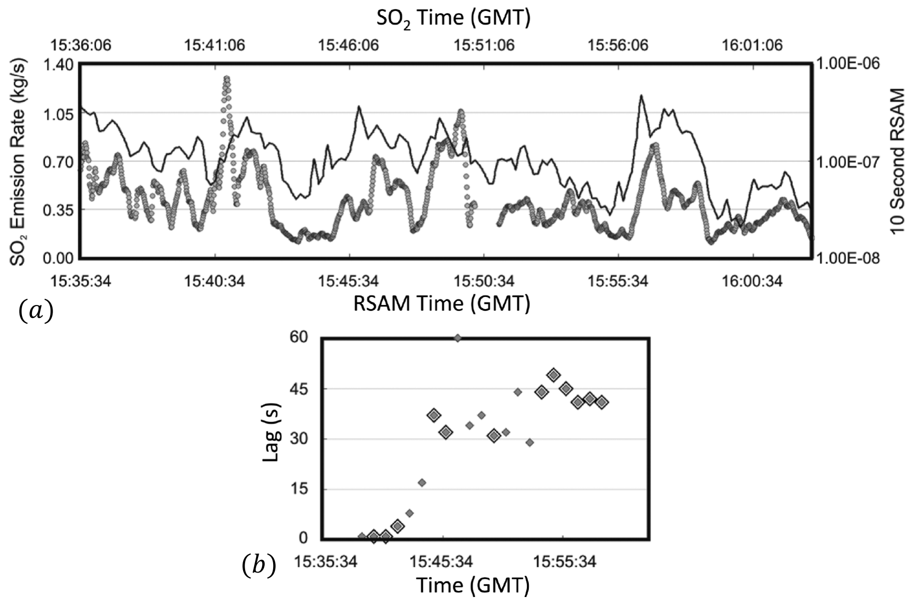

Figure 1.9: From [30] with permission. **a**. Time series for both 10-s averaged tremor amplitude, and SO_2 vent gas emission rate (in kg/s) for Fuego volcano in 2009. The top and bottom abscissa are offset by 32 s to compensate for overall lag. **b**. Evolution of the time lag between tremor and gas flux, where larger diamonds indicate correlation between time series larger than 0.65.

Cross-correlations of seismic signals measured at two stations across the Redoubt vent prior to its 2009 March eruption and showed that tremor signals are out of phase by approximately half the dominant oscillation period (see Fig. 1.11).

1.3.4 3D magma wagging model

Building on [6, 21], which are restricted to two-dimensional lateral wagging in Cartesian geometry, Liao et al. [26] extend the model to three dimensions, and column displacement can occur in any direction and plane, see Fig. 1.12. They identify new "whirling" regimes in the limit of very long vertical wavelength, i.e., $k \to 0$ and viscous damping is negligible [21]. In

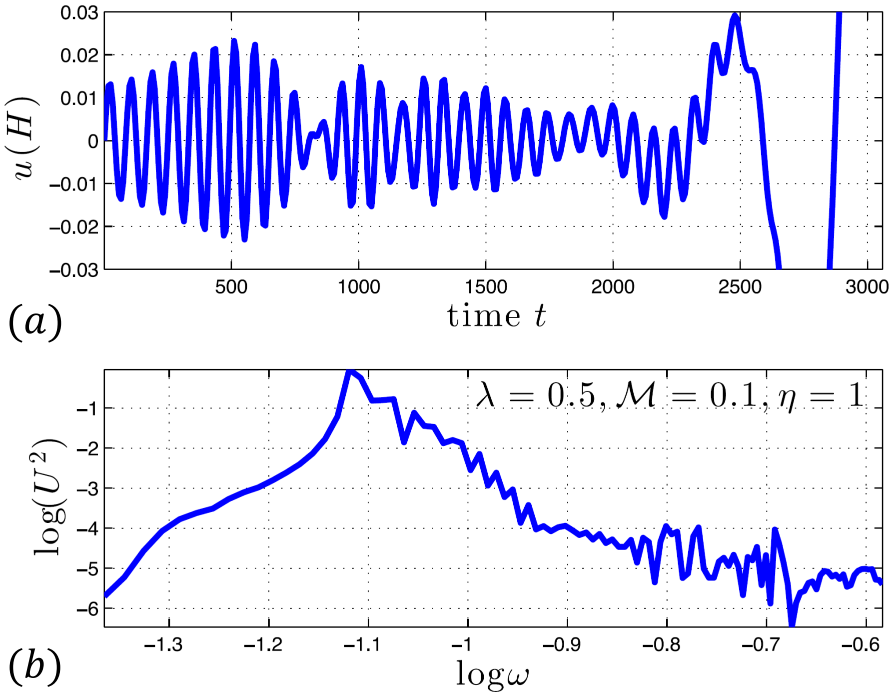

Figure 1.10: From [6] with permission. Time series and power spectrum for surface displacement for a case with $\lambda = 0.5$, $M = 0.1$, and $\eta = 1$. The power spectrum is from a Fourier analysis of the time series with the background growth removed; power is in terms of $U^2(\omega)$ where $U(\omega)$ is the discrete Fourier transform of $U(H)$, and ω is the discrete angular frequency.

this condition, displacement is continuous along the z direction, and at any arbitrary height, the horizontal section of the magma column orbits, circular or elliptical orbit, around the center of the conduit. The elliptical/circular orbit is an expression of conservation of specific energy E_0, and the shape of the orbit is determined by the ratio of the linear component of specific energy to the rotational component of specific energy ER (see §2.5). Once these energy components are determined, the solution can be found.

Before an eruption, the increasing rate of gas exclusion and driving force from the bubbles contribute to the total specific energy E_0 accumulation,

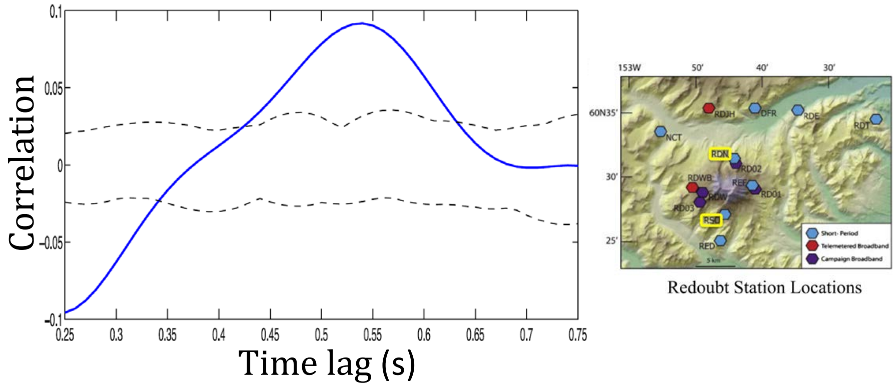

Figure 1.11: Unbiased cross-correlation function between signals from seismometers located north (RDN) and south (RSO) of Redoubt volcano prior to its eruption on 2009 March 22. There is a positive correlation between the signals with a time lag of 0.55 s. The time lag is approximately half the period of the period of the dominant signal (1 s). Dash lines show the 95% confidence interval for cross-correlation calculations.

which can modify linear and rotational components of energy and, in turn, the wagging orbits. Figure 2.11 shows different elliptical whirling orbits. When the ratio of linear kinetic energy to rotational kinetic energy is zero $ER = 0$, whirling happens with a circular orbit. Increasing ER changes wagging toward more elliptical orbits. At very high energy ratios, $ER \to \infty$, whirling orbit changes to a straight line and the two-dimensional magma wagging in a single plane is resolved.

Similar to two-dimensional magma wagging (where $ER \to \infty$), the radiation pattern of a seismic signal emanating from a three-dimensional magma wagging is correlated with motions of the magma column (see Fig. 1.13). Indeed, Liao et al. [26] suggested a method to identify the behavior of the magma column using the seismic data received from a series of seismic stations around a volcano. The approach is based on calculating the relative time-lag between seismic station pairs.

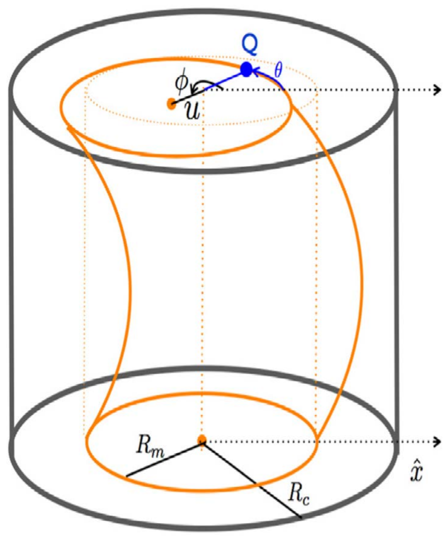

Figure 1.12: From [26] with permission. Sketch of the 3D magma wagging model. The column is assumed to have a free surface at the top and is coupled viscously to the magma system below. ϕ is the polar angle of the magma columns displacement, u is the radius displacement, or equivalently the displacement magnitude. R_c and R_m are the radii of the magma column and volcanic conduit, respectively.

1.3.5 Summary of magma wagging model predictions

On the basis of previous studies on magma wagging model, which is presented briefly in the previous section §1.3.1, in this section we list the predictions of magma wagging model that are testable and can be measured in data from field studies:

1. The fundamental frequency of oscillation of a magma column inside a foamy vesicular annulus corresponds to volcanic tremor frequency (see Fig. 1.4 and equation 1.2).

2. Increasing the annulus thickness causes the wagging frequency to decrease as $\omega_0 \propto (R_c^2 - R_m^2)^{-1/2}$ (see Fig 1.4).

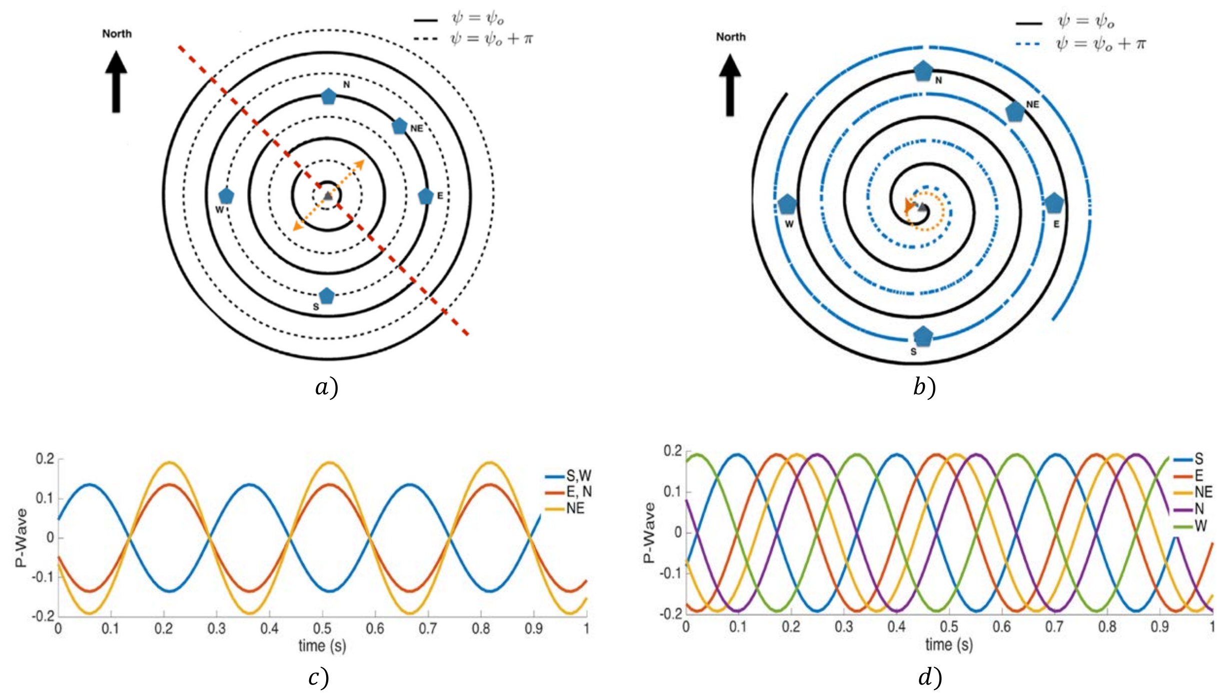

Figure 1.13: From [26] with permission. **a**. Contours of phase-shift of P-waves generated by a 2D wagging at a frequency of 3.3 Hz. Black lines and dashed lines are two groups of equal-phase contours which are out-of-phase with each other. Pentagons indicate the location of five virtual seismic stations. The orange dash line with arrowhead indicates the direction of the wagging plane.**b**. Contours of phase-shift of P-waves generated by a counter-clockwise wagging with circular whirling orbit at a frequency of 3.3 Hz. Black solid lines and blue dashed lines are two groups of equal-phase contours which are out-of-phase with each other. Pentagons indicate the location of five virtual seismic stations. The orange dash line with arrowhead indicates the counter-clockwise wagging direction. **c**. P-waves calculated at the five virtual stations in **a**, which are in-phase or out-of-phase with each other. Stations that are not in the same phase have half a period of oscillation $T_0/2 = 0.15$ s lag relative to each other.**d**. P-waves calculated at the five virtual stations in **b**.

3. Increasing bubble volume fraction in the annulus causes the wagging frequency to decrease as $\omega_0 \propto \sqrt{1/\phi_0}$.

4. Toward the onset of volcanism when fragmentation disturbs annulus and porosity ϕ_0 in the annulus vary in space, narrow band tremor signal changes to broadband tremor as $\omega_0 \propto \sqrt{1/\phi_0}$, where ϕ_0 varies in space.

5. Degassing and audible chugging and tremor signals should be correlated (Figs. 1.6 and 1.8).

6. Envelopes in tremor signals correspond to the superposition of modes that are excited due cascading of energy from wagging frequency to the higher harmonics (Figs. 1.10 and 1.8).

7. Ground motions and related pressure waves distributed around the volcano as the results of magma column displacements inside the volcano should be spatially and temporarily correlated (Figs. 1.11 and 1.13).

8. En route to the eruption magma column whirling orbit change because magma column energy changes, i.e., change in degassing behavior and gas flux in the annulus changes the energy components of magma column (Fig. 2.11).

1.4 Critical knowledge gaps

Jellinek & Bercovici [21] propose the magma wagging model and explore its properties in 2D while the gas flow is not allowed in the annulus. Later, Bercovici et al. [6] extend magma wagging studies by allowing gas to flow into permeable annulus and show how Bernoullis effect of gas flux can drive magma waging. These two studies restrict the motion of the magma column to a two-dimensional in a plane. Building on the work, Liao et al. [26] propose an extended magma wagging model in 3D with impermeable annulus that relaxes the 2D constraint and explore the spatial and temporal features of the seismic radiation pattern associated with tremor.

These studies are able to explain the ubiquity, persistence, and temporal behavior of pre- and syn-eruptive volcanic tremors observed at different volcanoes. Magma wagging theory is, thus, a potentially fully predictive model for explosive volcanic eruptions. A key knowledge gap, however, is experimental verification that the main underlying physical processes identified theoretically are an accurate and complete description of the phenomenon. Critically, whether the long period Bernoulli mode can continuously drive the predicted magma wagging is unclear. In this theory, the delivery of energy from long period Bernoulli modes to short period wagging is only hypothesized. This energy transfer to do the work of wagging against viscous dissipation must be shown before the model can be taken to be reliable. Furthermore, additional processional and possibly torsional modes may emerge together with the lateral wagging modes that are identified in 3D cylindrical geometries. Perhaps most important related to explosion and fragmentation is that porosity can be modified and lead to non-uniform gas flux around the magma column. With the aid of experiments, we can investigate how an inherent asymmetric distribution of gas flux modulates the Bernoulli mode and affects the wagging model, in turn.

1.5 Thesis objectives and outlines

The primary goal of this thesis is to test the magma wagging model experimentally. Next, we extend the model to explore spatially non-uniform gas flux, which is not tractable analytically and very challenging in 3D numerical simulations. To this end, we design and build an analog that captures the essential dynamics expressed through equations 1.1-1.6.

The outline of this work is as follows: in Chapter 2, we first introduce the experimental setup. Next, we discuss the mathematical modeling used for analyzing the experimental results. We finish the chapter with a discussion of the dynamic similarity between experiment and the model applied to real volcanoes and discuss the scaling in the problem. In Chapter 3, we present experimental results. We identify three regimes for the experiments and analyze the mechanical conditions favoring each class of wagging. We end this chapter with a discussion of the experimental results. In Chapter 4, to better understand and extend aspects of the experimental results, we carry out 2D Cartesian numerical simulations of our experiments. In Chapter 5 we discuss the implication of our work for real volcanic activities. Finally, we conclude in Chapter 6 with a summary of the main results from this thesis, further discussion of limitations of this study, and future work.

Chapter 2

Methods

In this chapter, we present the experimental setup and strategy. We then introduce some mathematical modeling we will use in this work to characterize experimental data. Finally, following this quantitative analysis of our experiment, we introduce dimensionless control parameters that we use to understand our results as well as their relevance to establish dynamic similarity with the magma wagging model.

2.1 Experimental setup

Our analog experiments are carried out in a 10.16 cm (4″) diameter × 180 cm long hollow acrylic cylinder, which simulates a volcanic conduit. We install a viscoelastic rubber column with physical properties, lengths, and diameters that we vary at the center of a manifold that forms the tank base. Whereas the top of the column is a free surface, the column is fixed at the base with a peg that prevents vertical, radial and azimuthal motions. The rubber columns are made of Smooth-On's "VytaFlex^{TM}" urethane rubbers in $50A$ and $60A$ shore hardness with physical properties given in table 2.1. In these experiments the balance between restoring gas spring and viscous damping force expressed through η equation 1.7 is captured through prescribed physical properties in our rubber column. This approach enables us to explore the essential physics of magma wagging at the laboratory scale. It is im-

Column	C1	C2	C3	C4
D (cm)	8.9	8.9	7.6	7.6
L (cm)	108	80	112	90
ρ (kg/m^3)	1040	1040	1040	1040
Shore hardness	60A	50A	50A	60A
$\mu^\star$ (Pa.s)	8.18e4	2.02e4	1.59e4	1.22e4
$E^\star$ (MPa)	1.13	0.50	0.23	0.10

Table 2.1: Physical properties of VytaFlex^{TM} columns used in the experiments. * comes from experiments, see §2.3.2

possible to capture both the elasticity of a permeable annulus and column inertia at the laboratory scale. Similarly, through this setup we capture the critical damping effects that enable us to explore whether a Bernoulli mode can sustain higher frequency wagging.

At the start of each experiment, we insert air at the base of the cylinder through the manifold with 12 equally-spaced 0.95 cm ($3/8''$) diameter holes positioned around an 8 cm circle. We explore the responses of columns with prescribed elastic and linear damping properties to variously forced annular airflows. We control the distribution of air and the flow rate from each hole using Panel-Mount flow-meters to measure the inflow. These flow-meters can quantify the flow in the range of $4.2 - 42$ SCFM ($1.982 - 19.82$ lit/sec) with 2% accuracy.

To characterize and understand quantitatively, the excitation, evolution, and steady-state oscillating behaviors of our columns over a broad range of conditions, we use three CANON EOS 80D cameras mounted normal to and above the columns, see Fig. 2.1. Each of these cameras records column movement with a rate of 29.97 frames per second. We put the hollow cylinder inside a rectangular tank and fill the volume between them with water. This approach removes the challenge imaging through a curved boundary as water and Acrylic glass have similar refractive indexes. Besides, we attach one Tri-Axis accelerometer on each side of the tank to capture the pressure variation induced by column movement during each experiment. We use the Arduino computing platform to control and record the accelerometers. The sampling rate of the data that these devices provide is around 90 Hz, see Fig. 2.1.

2.2 Column calibration

We carry out initial experiments to characterize the elastic and damping properties of each column. We also test the apparatus to ensure steady-state oscillation can be obtained. In doing this, we identify three column wagging regimes during each experiment: **i**. a transient startup with the onset of gas forcing, **ii**. a statistical steady-state; **iii**. and a transient decay when the forcing is removed.

We define the initial transient regime as the period from when the flow is introduced around the rubber column until a steady response of the column is established. The steady-state regime is marked by statistically stationary column behavior and is the period between the end of the transient regime until the cessation of forcing. Oscillations in the steady-state regime constrain the inertial and elastic forces and reflect a balance between power delivered by gas flux and column dissipation. The damping regime following cessation of forcing defines the viscous response of the column (Fig. 2.3). We use oscillation and displacement behavior in the damping regime to characterize the elastic and viscous properties of the rubber columns as they are expressed through (e-fold) damping time scale, T_d, for motions to cease and the natural frequency of oscillation, ω_n (§2.3.1). For example, Fig. 2.2 a. shows an evolution of a trajectory in $x - y$ plane of top of the column, which is captured by the camera installed above the experimental setup, normalized by the gap width between the hollow cylinder and rubber column δ in x and y direction. The data show a short initial transient, a sustained period of steady-state behavior and a transient decay in amplitude where gas forcing is turned off.

In Fig. 2.3 we highlight the initial transient and damping periods. Figure 2.3 a. and d. are examples of the trajectory of top of the column in the transient and damping regime, respectively. When input flow is introduced around the column, it displaces from the resting position, and the displace-

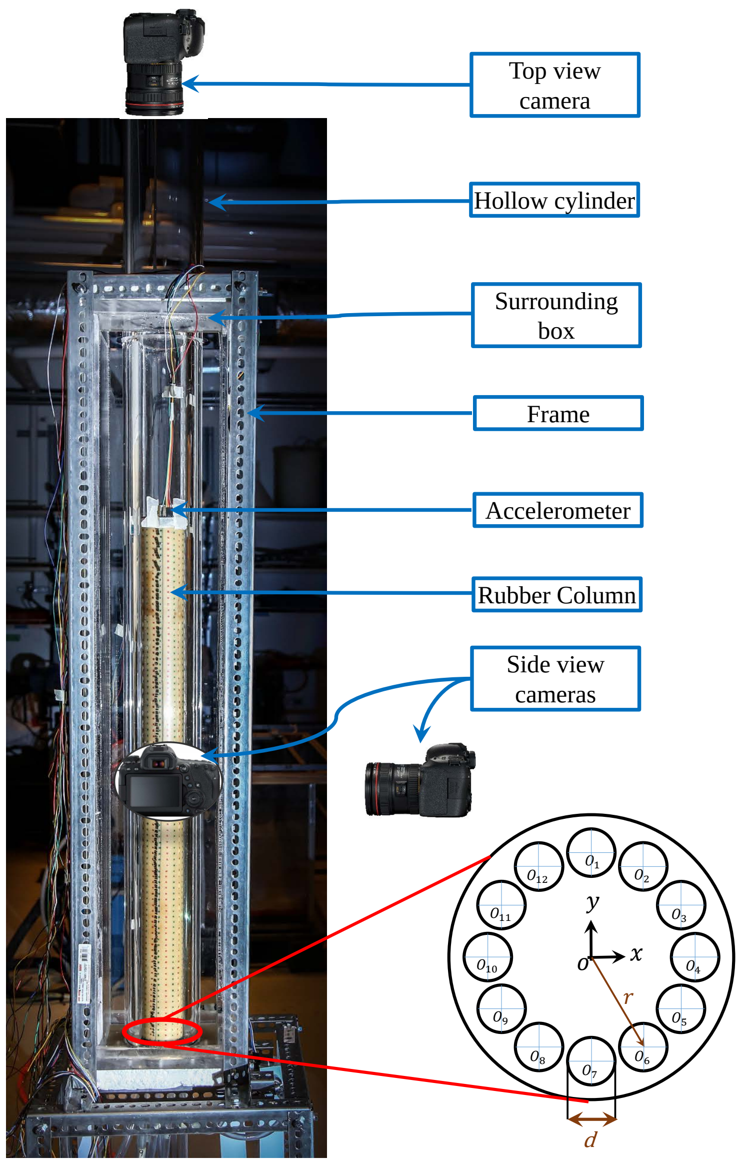

Figure 2.1: Experimental setup and the arrangement of inlets in the manifold. Hollow cylinder dimensions: 10.16 cm internal diameter × 180 cm long. Surrounding box dimensions: 20 cm×20 cm×125 cm. The top camera is fixed 20 cm above the apparatus, and the distance between side cameras and the tank surface is 150 cm. Distance between the center of the manifold and inlets r is 4 cm, and inlets diameter d is 0.95 cm.

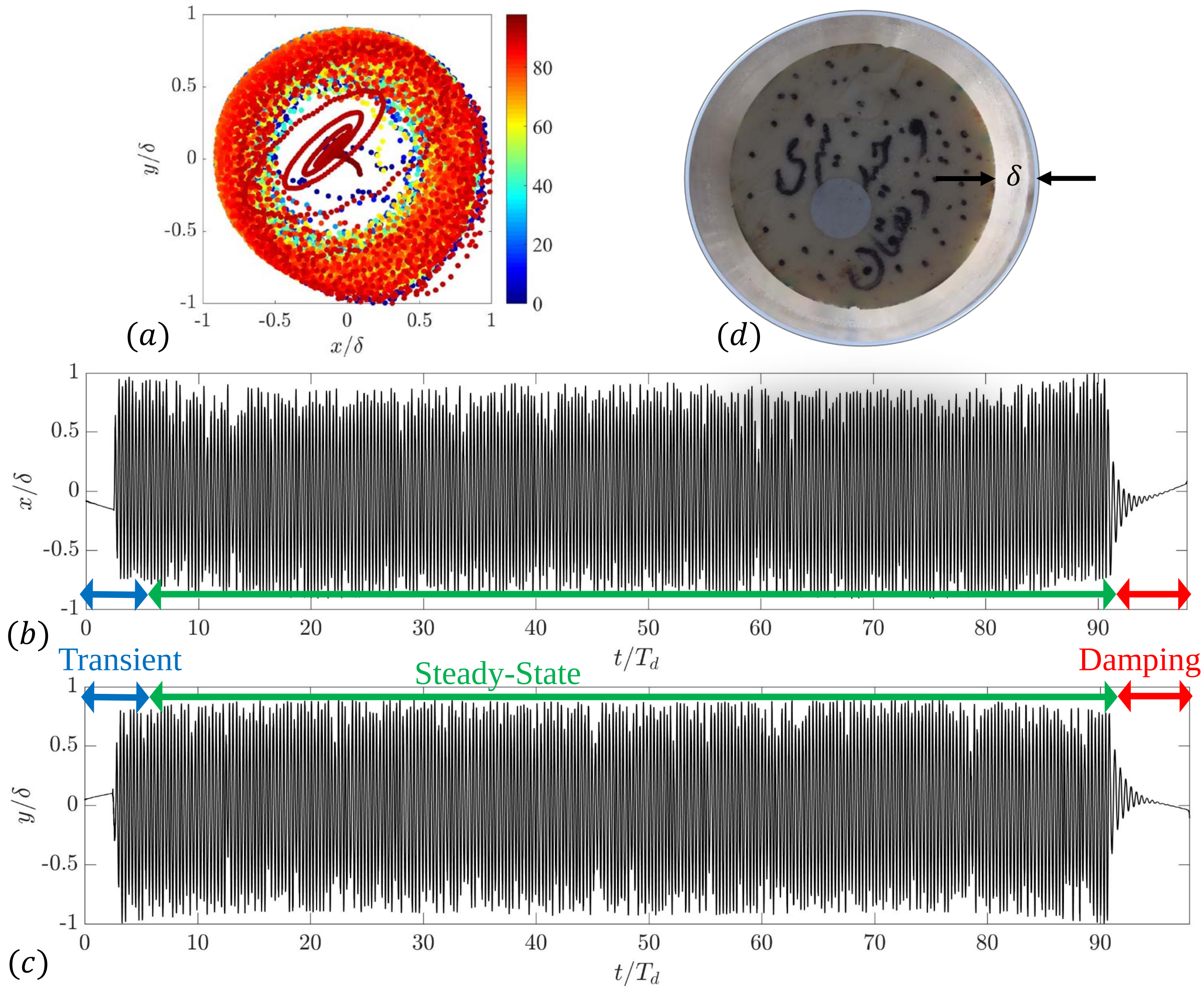

Figure 2.2: **a**. Example of trajectory of top of the column. Displacements in x and y directions are scaled by δ. Colorbar shows the dimensionless time t/T_d. **b**. The corresponding time series in x direction, and **c**. The corresponding time series in y direction. Transient-startup, steady-state, and damping regimes are defined in the text.

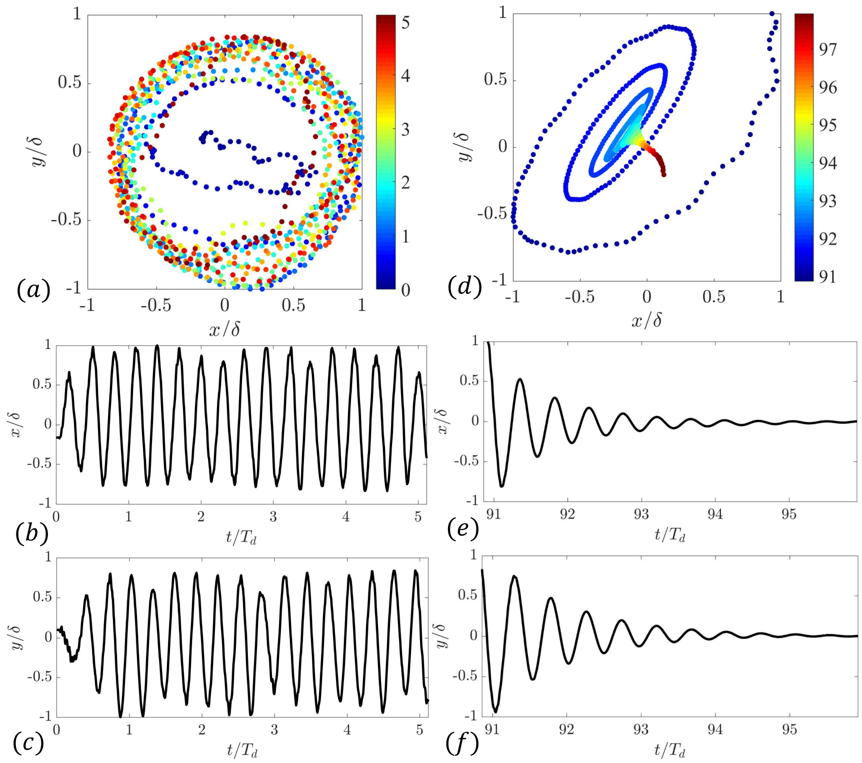

Figure 2.3: **a**. Example of trajectory of top of the column during the transient forcing, **b**. the corresponding time series in x direction, and **c**. the corresponding time series in y direction. **d**. Example of trajectory of top of the column during the damping regime, **e**. the corresponding time series in x direction, and **f**. the corresponding time series in y direction.

ment amplitude increases until the steady-state regime emerges. During the damping regime (Fig. 2.3), after airflow stops, oscillations decay in amplitude and column generally recovers a resting position. Therefore, it oscillates while the amplitude of oscillation decreases exponentially over time until it reaches the resting position. Corresponding time series to the transient and damping trajectories are shown in Fig. 2.3 b-c and e-f, respectively.

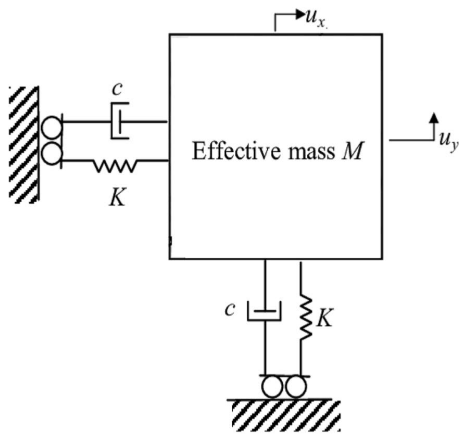

Figure 2.4: Schematic of simplified version of experiments viewed from top.

2.3 Calibrating the column response properties with mathematical models

2.3.1 2D mass-spring-damper model

From Fig. 2.2 and Fig. 2.3, the column has a characteristic damping time, T_d, and an oscillation frequency, ω_n, that are consistent during the initial, steady-state, and damping regimes. Thus, here we develop mathematical models for the response of the system to the imposed gas forcing to constrain the elastic properties of the column quantitatively. This exercise enable us to verify whether our experiments adequately captures the effect of η in equation 1.6.

When we look at the column from the top, we can simulate the system to a two degree of freedom mass-spring-damper system, see Fig. 2.4. In this system c is damping coefficient, K is spring constant, and M is the mass in the system. Newton's second law of column motion can be written,

$$\frac{d^2u}{dt^2} + \frac{c}{M}\frac{du}{dt} + \frac{K}{M}u = f, \tag{2.1}$$

where $u = u(x, y)$ is the displacement and f is the effective force per mass. equation 2.1 is usually written into the form of:

$$\frac{d^2u}{dt^2} + 2\zeta\omega_n \frac{du}{dt} + \omega_n^2 u = f, \tag{2.2}$$

where the damping ratio ζ and natural frequency ω_n of the system are:

$$\zeta = \frac{c}{2\sqrt{MK}} \qquad \text{and} \qquad \omega_n = \sqrt{\frac{K}{M}}.$$

For a free oscillation akin to the damping regime ($f = 0$), the solution of equation 2.2 is:

$$u = Ae^{-\zeta\omega_n t} cos(\omega_d t + \phi), \tag{2.3}$$

where the amplitude A and phase ϕ determine the behavior needed to match initial conditions, and the fundamental damped frequency ω_d is:

$$\omega_d = \omega_n (1 - \zeta^2)^{1/2}. \tag{2.4}$$

We non-dimensionalize equation 2.2 by selecting the gap width δ as the length scale and the column relaxation time $T_d = 1/\zeta\omega_n$ as the damping time scale. In this case we define $u(x, y) = u'(x, y)\delta$, $t = t'T_d$ and the equation of motion changes to (after dropping the primes):

$$\frac{d^2u}{dt^2} + 2\frac{du}{dt} + \gamma^2 u = f, \tag{2.5}$$

where the balance between elastic and restoring damping forces (akin to η in equation 1.6) is expressed through the ratio of time scales for damping and natural oscillation:

$$\gamma = T_d \omega_n. \tag{2.6}$$

We solve equation 2.5 during transient decaying regime where $f = 0$ by assuming $u(t) = e^{rt}$ and it results in:

$$u(t) = C_1 e^{(-1+i(\sqrt{\gamma^2-1}+\phi))t} + C_2 e^{(-1-i(\sqrt{\gamma^2-1}+\phi)t}, \tag{2.7}$$

where C_1, C_2, and ϕ are determined by imposing the initial conditions. It is to be observed from equation 2.7 that decaying constant is unity and the value of γ determines the behavior of system in the free oscillation:

- Overdamped $\gamma < 1$: The system exponentially decays to steady-state without oscillating.
- Critically damped $\gamma = 1$: The system returns to steady-state as quickly as possible without oscillating.
- Underdamped $\gamma > 1$: The system oscillates with a slightly different frequency than the natural frequency with the amplitude gradually decreasing to zero.

As we discussed in §2.2, we characterize the damping properties of rubber columns using the transient decaying regime. For more detail, assuming that the column damping is linear (equation 2.5 holds), the amplitude of oscillation will decay as $\exp(-t/T_d)$. From experimental fits to the displacement time series in the damping regime, we use an exponential fork envelop of the oscillation to find the decay rate of the amplitude in the free oscillation $1/T_d$ and the characteristic damping time.

Figure 2.5 a-b are examples of fitted curves to damping regime in x and y direction for one of the experiments. Calculated damping coefficients ($\zeta\omega_n$) is 0.20 in x and y direction. Figure 2.6 shows the distribution of the damping coefficient calculated from all the fitted curves to damped regimes during experiments. Solid lines are fitted Gaussian curve to the distributions. The mean values of damping coefficients $\overline{\zeta\omega_n}$ and its standard deviation σ, for different columns can be read from this figure and is reported in Table 2.2.

From spectral analysis of time series of the damping regime we also find, in turn, the fundamental damped frequency ($\omega_d = 2\pi f_d$). Figures 2.7 a. and b. show the frequency spectrum of damping time series in Figs. 2.5 a. and b., respectively. Both time series demonstrate peak frequency at 0.29 Hz.

Figure 2.8 shows the distribution of fundamental damped frequency calculated from all the damped time series during experiments. Solid lines are fitted Gaussian curve to the distributions. The values of damped frequencies

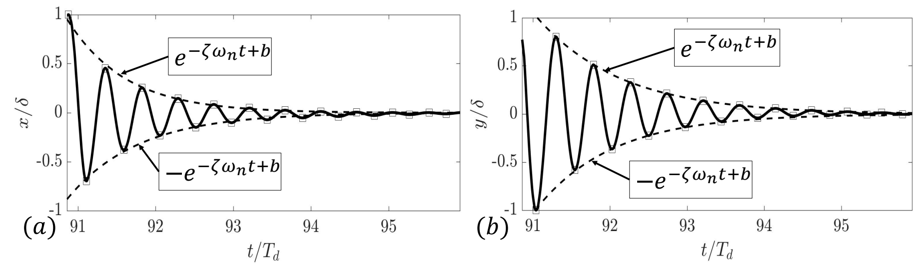

Figure 2.5: **a**. The trajectory of top of the column in x direction, **b**. The trajectory of top the column in y direction. Dashed lines present envelopes fitted to trajectories to calculate damping coefficient.

Column	$\overline{\zeta\omega_n}$	σ
C1	0.42	0.2
C2	0.38	0.15
C3	0.15	0.03
C4	0.2	0.19

Table 2.2: Values of damping coefficients and its standard deviation for different columns.

($\bar{\omega}_d$) and its standard deviation (σ) for different columns can be read from this figure and is reported in Table 2.3.

With the linear damping we can calculate the natural frequency of free

Column	$\bar{\omega}_d$	σ
C1	3.38	0.61
C2	4.33	0.17
C3	2.10	0.17
C4	1.62	0.20

Table 2.3: Values of fundamental damped frequency and its standard deviation for different columns.

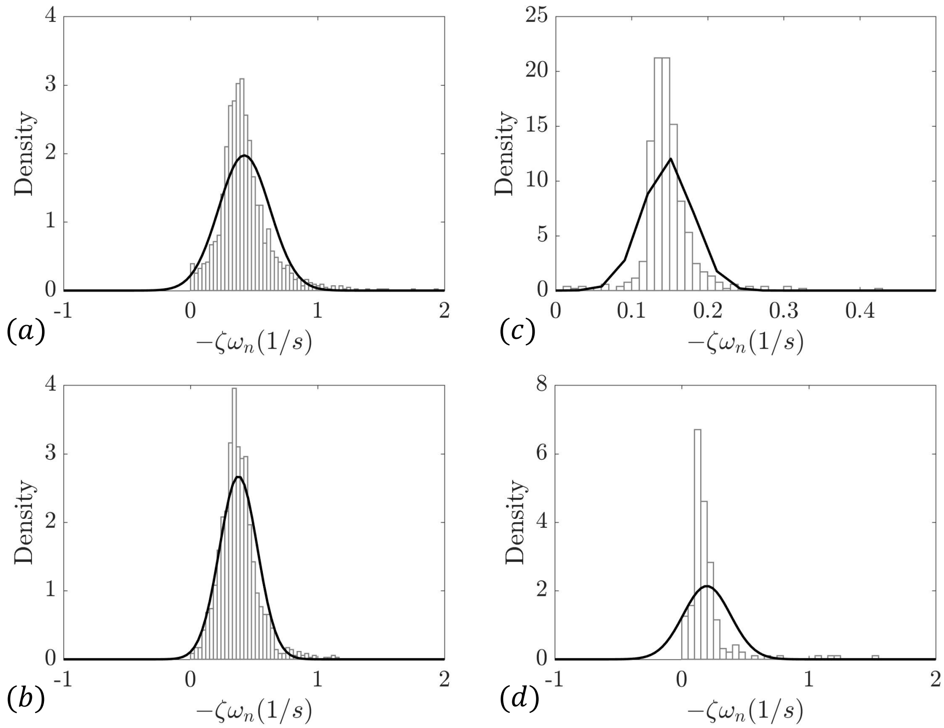

Figure 2.6: Histograms of damping coefficient ($\zeta\omega_n$ in 2.3) calculated from damped time series. Solid lines represents the fitted Gaussian curves. **a**., **b**., **c**., and **d**. correspond to C1, C2, C3, and C4 respectively.

oscillation ω_n by substituting $T_d = 1/\zeta\omega_n$ in equation 2.4 and rearranging it in the form of:

$$\omega_n^2 = \omega_d^2 + \frac{1}{T_d^2}. \tag{2.8}$$

We have used two-dimensional mass-spring-damper model to characterize relaxation time, T_d, and oscillation frequency, ω_n, of columns used in experiments. The values of T_d, ω_n, and γ for different rubber columns used in our experiments are shown in Table 2.4. Note that the transient-startup regimes usually takes between 1 to 3 relaxation times, e.g., see Figs. 2.2 and 2.3 but we find statistically stationary steady-state is related to experiments

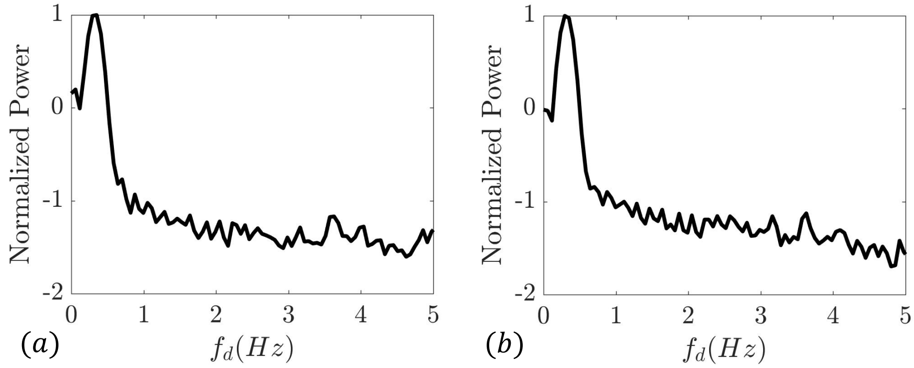

Figure 2.7: **a**. power spectrum of Fig. 2.5 a., **b**. power spectrum of Fig. 2.5 b.

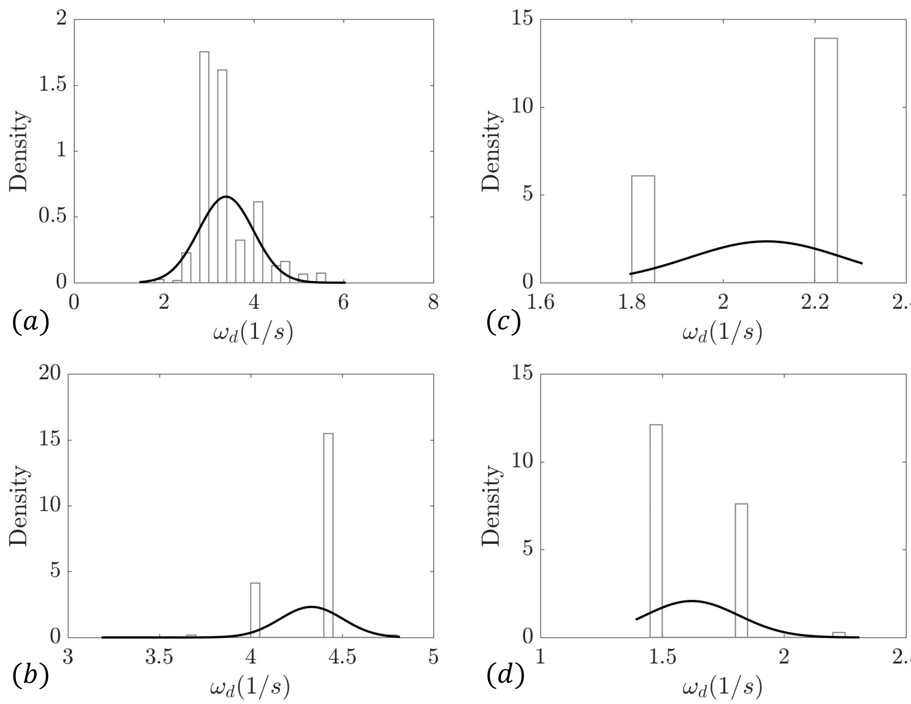

Figure 2.8: Histograms of damped angular frequency (ω_d) calculated from damped time series. Solid lines represent the fitted Gaussian curves. **a**., **b**., **c**., and **d**. correspond to C1, C2, C3, and C4 respectively.

Column	$\bar{T}_d$	$\bar{\omega}_n$	γ
C1	2.38	3.40	8.16
C2	2.63	4.35	11.53
C3	6.66	2.10	14.08
C4	5.00	1.63	8.15

Table 2.4: Values of relaxation time, natural frequency of the system, and column's characteristics number.

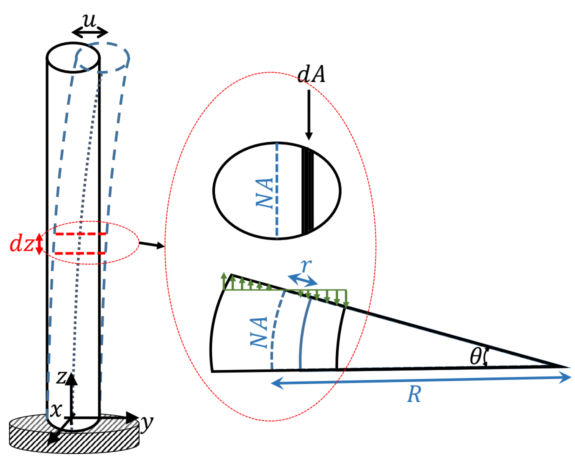

Figure 2.9: Schematic of simplified version of experiments from side view.

after 5 relaxation times T_d, in particular.

2.3.2 Cantilever beam model

Whereas equation 2.5 provides insight into relaxation time and natural frequency of the column, we need to study column's bending to understand the elastic properties of column and to constrain the effective viscosity and Young's modulus of the column.

When we look at the column from side, we can simulate it to a viscoelastic cantilever beam. We solve cantilever beam problem to characterize the viscous properties of the column and its elastic response to the forcing. To govern the equation of motion for the column, we consider a viscoelastic beam that has a cross-sectional area A, moment of inertia I, Young's modulus of elasticity E, material density ρ, and efficient viscosity μ. Now consider an element of the length dx of the beam that is bent on one side, e.g. Fig. 2.9. Here, the column is compressed at the right side of neutral axis NA and is decompressed at the left side of NA. Strain ϵ at distance r from NA can be written,

$$\epsilon = \frac{(R-r)\theta - R\theta}{R\theta} = \frac{r}{R}, \tag{2.9}$$

where R is the radius of bending curvature. We use KelvinVoigt model consists of a Newtonian damper and elastic spring connected in parallel to model viscoelasticity of the material. Stress σ related to strain ϵ in this model can be written,

$$\sigma = E\epsilon + \mu\dot{\epsilon}, \tag{2.10}$$

where $\dot{\epsilon}$ is the strain rate and from equation 2.9 it can be written,

$$\dot{\epsilon} = -\frac{r}{R^2}\dot{R}. \tag{2.11}$$

From the definition of stress σ we have:

$$df = \sigma \ dA, \tag{2.12}$$

where df is the force applied to the area dA, and the partial bending moment dM from this force is:

$$dM = r \ df, \tag{2.13}$$

now we can find bending moment M by integrating dM across the area A:

$$M = \int \sigma r dA = \int (\frac{E}{R} - \frac{\mu}{R^2}\dot{R}) r^2 dA = (\frac{E}{R} - \frac{\mu}{R^2}\dot{R}) I. \tag{2.14}$$

Assuming small deflections along the column, bending curvature R can be written,

$$\frac{1}{R} = \frac{\partial^2 u(z,t)}{\partial z^2}, \tag{2.15}$$

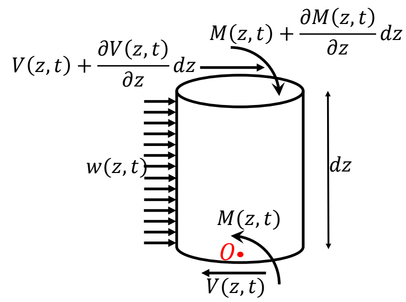

Figure 2.10: Free body diagram for an element of column. w is externally distributed load, V is shear force, and M is bending moment.

Where $u(z,t)$ is column deflection at distance z and time t, hence,

$$-\frac{\dot{R}}{R^2} = \frac{\partial^3 u(z,t)}{\partial t \partial^2 z}, \tag{2.16}$$

where t represents time. Then substituting equation 2.15 and equation 2.16 in equation 2.14 gives the relation between bending moment and deflection in viscoelastic beams,

$$M(z,t) = EI\frac{\partial^2 u(z,t)}{\partial z^2} + \mu I\frac{\partial^3 u(z,t)}{\partial t \partial z^2}. \tag{2.17}$$

A free body diagram for an element of column is shown in Fig. 2.10. If we derive Newton's second law for this element we have:

$$\rho A dz\frac{\partial^2 u(z,t)}{\partial t^2} = w(z,t)dz + \frac{\partial V(z,t)}{\partial z}dz, \tag{2.18}$$

then for the element, neglecting rotary inertia, taking moments about O:

$$\frac{\partial M(z,t)}{\partial z} = -V(z,t), \tag{2.19}$$

$$\frac{\partial V(z,t)}{\partial z} = -\frac{\partial^2 M(z,t)}{\partial z^2}, \tag{2.20}$$

finally substituting equation 2.17 and equation 2.20 into equation 2.18 leads to the governing equation of motion for a viscoelastic cantilever beam under a distributed load $w(z)$:

$$\frac{\partial^4 u(z,t)}{\partial z^4} + \frac{\mu}{E}\frac{\partial}{\partial t}\frac{\partial^4 u(z,t)}{\partial z^4} + \frac{\rho A}{EI}\frac{\partial^2 u(z,t)}{\partial t^2} = \frac{w(z,t)}{EI}. \tag{2.21}$$

We non-dimensionalize equation 2.21 by choosing the gap width δ as the length scale for y direction, column height L as the length scale for z direction, and T_d as the time scale. We define $u = u'\delta$, $z = z'L$, $t = t'T_d$ and the equation of motion changes to (after dropping the primes):

$$\frac{\partial^4 u(z,t)}{\partial z^4} + \frac{\mu}{ET_d}\frac{\partial}{\partial t}\frac{\partial^4 u(z,t)}{\partial z^4} + \lambda^4\frac{\partial^2 u(z,t)}{\partial t^2} = w(z,t), \tag{2.22}$$

where,

$$\lambda^4 = \frac{\rho A L^4}{EIT_d^2} \tag{2.23}$$

and λ is the characteristic of the column.

We are now going to solve equation 2.22 during transient decaying regime when $w(z,t) = 0$ by multiplying it by e^{ikz} and integrating with respect to z. Taking the Fourier transform with respect to z, for each fixed t, of $u(z,t)$ by:

$$\hat{u}(k,t) = \int_{-\infty}^{+\infty} u(z,t)e^{-ikz}dz, \tag{2.24}$$

and applying this solution to equation 2.22,

$$\lambda^4\frac{\partial}{\partial t^2}\hat{u}(k,t) + k^4\frac{\mu}{ET_d}\frac{\partial}{\partial t}\hat{u}(k,t) + k^4\hat{u}(k,t) = 0, \tag{2.25}$$

we can solve equation 2.25 by trying $\hat{z}(k,t) = e^{rt}$, which r can be a complex number, and it results in,

$$\hat{u}(k,t) = e^{-\alpha t}e^{\pm i\omega_d t}, \tag{2.26}$$

where

$$\alpha = \frac{k^4}{2\lambda^4}\frac{\mu}{ET_d} \qquad \text{and} \qquad \omega_d^2 = 2\alpha\frac{ET_d}{\mu} - \alpha^2,$$

so the general solution to equation 2.25 is:

$$\hat{u}(k,t) = \hat{U}_1(k)e^{-\alpha t}e^{+i\omega_d t} + \hat{U}_2(k)e^{-\alpha t}e^{-i\omega_d t}, \tag{2.27}$$

where $\hat{U}_1(k)$ and $\hat{U}_2(k)$ are arbitrary constants. Taking the inverse Fourier transform of equation 2.27 we obtain a linear ODE for $u(z)$:

$$\frac{\partial^4 u}{\partial z^4} - 2\alpha\frac{ET_d}{\mu}\lambda^4 u = 0, \tag{2.28}$$

and the general solution to the beam equation equation 2.28 is:

$$u = C_1 \cos \lambda' z + C_2 \sin \lambda' z + C_3 \cosh \lambda' z + C_4 \sinh \lambda' z, \tag{2.29}$$

where

$$\lambda'^4 = \frac{2\alpha ET_d\lambda^4}{\mu}, \tag{2.30}$$

and constants C_1, C_2, C_3, and C_4 are determined from boundary conditions. Applying the boundary condition for the cantilever beam:

$$u = 0, \qquad \frac{du}{dz} = 0 \quad \text{at} \quad z = 0,$$

$$\frac{d^2u}{dz^2} = 0, \qquad \frac{d^3u}{dz^3} = 0 \quad \text{at} \quad z = 1,$$

non-trivial solutions are found to exist only if $\cosh(\lambda')\cos(\lambda') + 1 = 0$ or:

$$\lambda' = 1.875, 4.694, 7.885, \ldots .$$

which different λ' correspond to different modes of oscillation.

As we mentioned at the beginning of this section the ultimate goal here is to characterize the viscoelastic properties of the column, and we know that time dependent solutions for equation 2.5 and equation 2.22 for the first mode of oscillation must be the same. By comparing equation 2.7 and equation 2.27 we have:

$$\alpha = 1 \quad \text{and} \quad \omega_d^2 = \gamma^2 - 1, \tag{2.31}$$

hence effective viscosity μ and Youngs' modulus can be found by comparing equation 2.23, equation 2.30, and equation 2.31,

$$\mu = 2\frac{\rho A L^4}{I T_d}\frac{1}{1.875^4} \quad \text{and} \quad E = \frac{\mu\gamma^2}{2T_d}, \tag{2.32}$$

where ρ is column density. Calculated values of E and μ for different columns are presented in Table 2.1. Note that if the column was pure elastic $\mu = 0$, decay constant vanishes $\alpha = 0$, the oscillation frequency becomes the natural frequency $\omega_n^2 = \frac{\lambda^2 EI}{\rho A L^4}$ and equation 2.27 changes to:

$$\frac{\partial^4 u(z,t)}{\partial x^4} - \lambda^4 u(z,t) = 0, \tag{2.33}$$

which can be solved as equation 2.28.

2.4 Scaling considerations

For each experiment, different inflows are introduced from each of the 12 inlets to the cylinder. Columns respond differently with respect to the total inflow and the arrangement of inflows. To characterize the symmetry and intensity properties of these different forcing scenarios and the mechanical response of the column, we define 2 parameters: a forcing eccentricity e and Deborah number De. We use

$$e = \frac{r'}{r}, \tag{2.34}$$

as a metric for the asymmetry of the flow around the column. Here, r is the distance between the manifold center and the inlet center, $r = |O_i - O|$, Fig. 2.1. The position r' is the distance between weighted average position of all inlets and the center of the manifold:

$$r' = \sqrt{\bar{x}_c^2 + \bar{y}_c^2},$$

where

$$\bar{x}_c = \frac{\Sigma_{i=1}^{12} Q_i x_i}{\Sigma_{i=1}^{12} Q_i} \qquad \text{and} \qquad \bar{y}_c = \frac{\Sigma_{i=1}^{12} Q_i y_i}{\Sigma_{i=1}^{12} Q_i}.$$

Here (x_i, y_i) and Q_i are the i^{th} inlet position and its flow rate. On the basis of this definition, e changes between 0 and 1, 0 presents the perfect symmetric forcing and 1 is the most asymmetric forcing, e.g. there is only one active inlet.

To characterize the amplitude of forcing for a specified eccentricity e and column damping we use a Deborah number:

$$De = \frac{T_d}{T_e}, \tag{2.35}$$

where T_d is the viscoelastic relaxation time of the rubber column and T_e is the time scale for the build up of elastic stresses in response to the forcing. Balancing the power delivered to an oscillation as a result of an imposed flow at mean velocity $\bar{v}$ with the build up of elastic potential energy gives us:

$$\frac{\Delta KE}{\Delta t} \sim \frac{PE}{T_e}, \tag{2.36}$$

where $KE = \rho_0 \bar{v}^2/2$ is the flow kinetic energy density, Δt is a timescale for delivery of this energy to do the work of orbiting an oscillation, and PE is the column elastic potential energy density related to the build up of strain (δ/L). The average velocity $\bar{v}$ of the flow around the column is given by:

$$\bar{v} = \frac{\Sigma_{i=1}^{12} Q_i}{A}, \tag{2.37}$$

where A is the area between rubber column and hollow cylinder:

$$A = \frac{\pi}{4}(D^2 - (D - \delta)^2), \tag{2.38}$$

and D is the internal diameter of hollow cylinder. If we take the advective time as $\Delta t = v/L$ then:

$$\frac{\Delta KE}{\Delta t} = \frac{1}{2}\frac{\rho_0 v^3}{L}. \tag{2.39}$$

To find PE we assume that column is under a constant distributed load such as maximum deflection on top of the column is δ. The corresponding load w will be:

$$w = \frac{8EI\delta}{L^4}, \tag{2.40}$$

bending moment M along the column due to distributed load w is:

$$M = \frac{w(L-z)^2}{2}, \tag{2.41}$$

where z is the distance from the fixed side. Then bending energy U stored in the column can be calculated from:

$$U = \int_0^L \frac{M^2}{2EI} dz \; = \; \frac{8EI\delta^2}{5L^3}. \tag{2.42}$$

Now we can find the column elastic potential energy density PE by:

$$PE = \frac{U}{V}, \tag{2.43}$$

where V is the volume of the column. Combining equation 2.39, equation 2.42, and equation 2.43, the elastic time scale is,

$$T_e = \frac{64}{5\pi} \frac{E}{\rho_0} \frac{I\delta^2}{L^3 D^2 \bar{v}^3}. \tag{2.44}$$

equation 2.44 shows that elastic response time of the column T_e is proportional to its Young's modulus of elasticity E and represents the importance of spring behavior of the column. On the other hand, relaxation time T_d is proportional to effective viscosity of the column μ and shows the importance of viscous damping. As a result, Deborah number $De = T_d/T_e$ indicates the importance of viscous forces in the column to elastic behavior of the column which is similar to the key dimensionless number $\eta = \nu_m/(CU)$ in the wagging model, equation 1.6, which is a metric for importance of viscous damping in the magma column to the gas spring force in the annulus in the original theoretical magma wagging model. In previous studies [6, 21] η varies in range of $5 - 50$. In this study, Deborah number changes between

$10 - 3 \times 10^4$. There is a notable difference between ranges of De and η because of their different definitions. De is a function of column properties and gas velocity ($De \propto \bar{v}^3$), however, η is defined by column properties and constant sound velocity in the gas.

2.5 Energetic contributions to column top trajectories

In Chapter 3, we will show that the trajectory of top of the column varies significantly for different airflow forcing. Following Liao et al. [26], we characterize steady-state trajectories in terms of contributions from linear and rotational kinetic energy as well as elastic potential energy.. Here, we use energetic components to define an energy ratio ER, which we apply later as a means to distinguish between different column behaviors. At steady-state where the power delivered through the injected air is balanced by dissipation as a result of linear damping, equation 2.22 reduces to,

$$\frac{d^2u}{dt^2} = -\omega_n^2 u, \tag{2.45}$$

In cylindrical-polar coordinate, equation 2.45 can be recast as two coupled evolution equations, for the radial and azimuthal displacement, respectively[3]

$$\frac{d^2u}{dt^2} - u\frac{d\phi}{dt}\frac{d\phi}{dt} + \omega_n^2 u = 0, \tag{2.46}$$

$$u\frac{d^2\phi}{dt^2} + 2\frac{du}{dt}\frac{d\phi}{dt} = 0, \tag{2.47}$$

We define specific energy E_0,

$$E_0 = KE_{Lin} + KE_{Rot} + PE, \tag{2.48}$$

where

$$KE_{Lin} = \frac{1}{2}(\frac{du(t)}{dt})^2$$

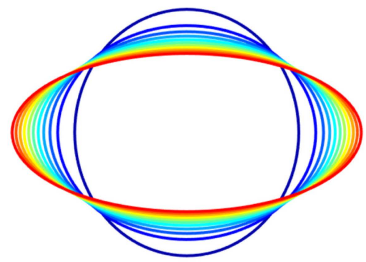

Figure 2.11: Different elliptical whirling orbits corresponding to different $ER = KE_{Lin}/KE_{Rot}$ values. Circular orbit corresponds to $ER = 0$. When $ER \to \infty$ orbit changes to a straight line.

is linear kinetic energy,

$$KE_{Rot} = \frac{1}{2}u(t)^2(\frac{d\phi(t)}{dt})^2$$

is rotational kinetic energy, and

$$PE = \frac{1}{2}\omega_n^2 u(t)^2$$

is potential energy. By definition at steady-state the total energy is conserved and the ratio of linear kinetic energy KE_{Lin} to rotational kinetic energy KE_{Rot} determines the shape of column trajectory.

$$ER = \frac{\overline{KE}_{Lin}}{\overline{KE}_{Rot}}, \tag{2.49}$$

where $\overline{KE}_{Lin}$ and $\overline{KE}_{Rot}$ are time-averaged for each experiment. Figure 2.11 shows experiments of different elliptical whirling orbits. Pure rotational motion/circular orbit occurs when $ER = 0$. By increasing ER, orbits become more elliptical. And, two-dimensional wagging oscillation is recovered in the limit of $ER \to \infty$.

Chapter 3

Experimental Results and Discussion

A given column displacement depends on the intensity and asymmetry of the air forcing from below. Here we study the displacement properties of each column to imposed forcing eccentricity e and intensity De for roughly 1000 individual experiments by using methods introduced in Chapter 2. In this chapter, we first characterize trajectories of the top of columns qualitatively in the steady-state regime into three cases of response of the column, depending on $e - De$ conditions; "rotational", "chaotic", and "mixed-mode". We then use the energy ratio ER to define the rationale for each response. Next, we examine the time series of the top trajectory spectrally and investigate the correlation and coherence between time series of acceleration captured by accelerometers for each response. Finally, we show all 1000 experiments on one regime diagram to investigate the effects of intensity and asymmetry of the airflow to the column responses.

3.1 Rotational, mixed-mode, and chaotic column responses

Here, we introduce "rotational", "chaotic", and "mixed-mode" responses for column trajectories and displacement in the steady-state regime.

Figure 3.1 is an example of a rotational motion that emerges for a symmetric airflow condition around the column with eccentricity $e = 0$ and a forcing intensity of $De = 1.4 \times 10^4$. The top of the column in rotational response follows a circular orbit with an approximately constant radius, see Figs. 3.1 a, c, d., and Fig. 3.2. In addition to this motion of the column top, continuous vertical deflections over the column length occur during each orbit (Fig. 3.1 b).

By contrast, Fig. 3.3 is an example of mixed-mode motion. In this example, the airflow distribution around the column is slightly asymmetric comparing to Fig. 3.1 and Fig. 3.2 with forcing eccentricity $e = 0.08$ and forcing intensity $De = 6.8 \times 10^3$. Under these $e-De$ conditions the trajectory of the column top orbits changes continuously over time (Fig. 3.3) with shifts in direction. The column's top follows predominantly circular trajectories with radial explosions over time scales $< T_d$ as well as time scales $\gg T_d$ (Fig. 3.4). Averaged over the full length of the experiments, column motions are, time varying combinations of rotational and linear displacements. The column intermittently ends up in rotational trajectories, but these responses are transient and variable in their longevity. In addition, vertical deflections of the column over its length during each orbit can be continuous or periodic. Finally, the amplitude of oscillations in $x/\delta \ - \ y/\delta$ space are not constant and characterized by emergent beating envelopes, Figs. 3.3 c. and d.

Figure 3.5 is an example of a chaotic displacement response. In this example the airflow around the column is highly asymmetric comparing to Fig. 3.1 and Fig. 3.3 with $e = 1$ and $De = 75$. Trajectories shift continuously over time scales $< T_d$, $\sim T_d$, and $\gg T_d$ with mainly linear displacements that are stochastic in time (Figs. 3.5 & Fig. 3.6). Vertical deflections of the column are chaotic and quasi-periodic in space and similarly stochastic in time. Similar to Fig. 3.3 the amplitude of oscillation in $x/\delta - y/\delta$ space are not constant, generally smaller than in rotational and mixed-mode responses with beating envelopes that are complex in their shape, where they exist at all.

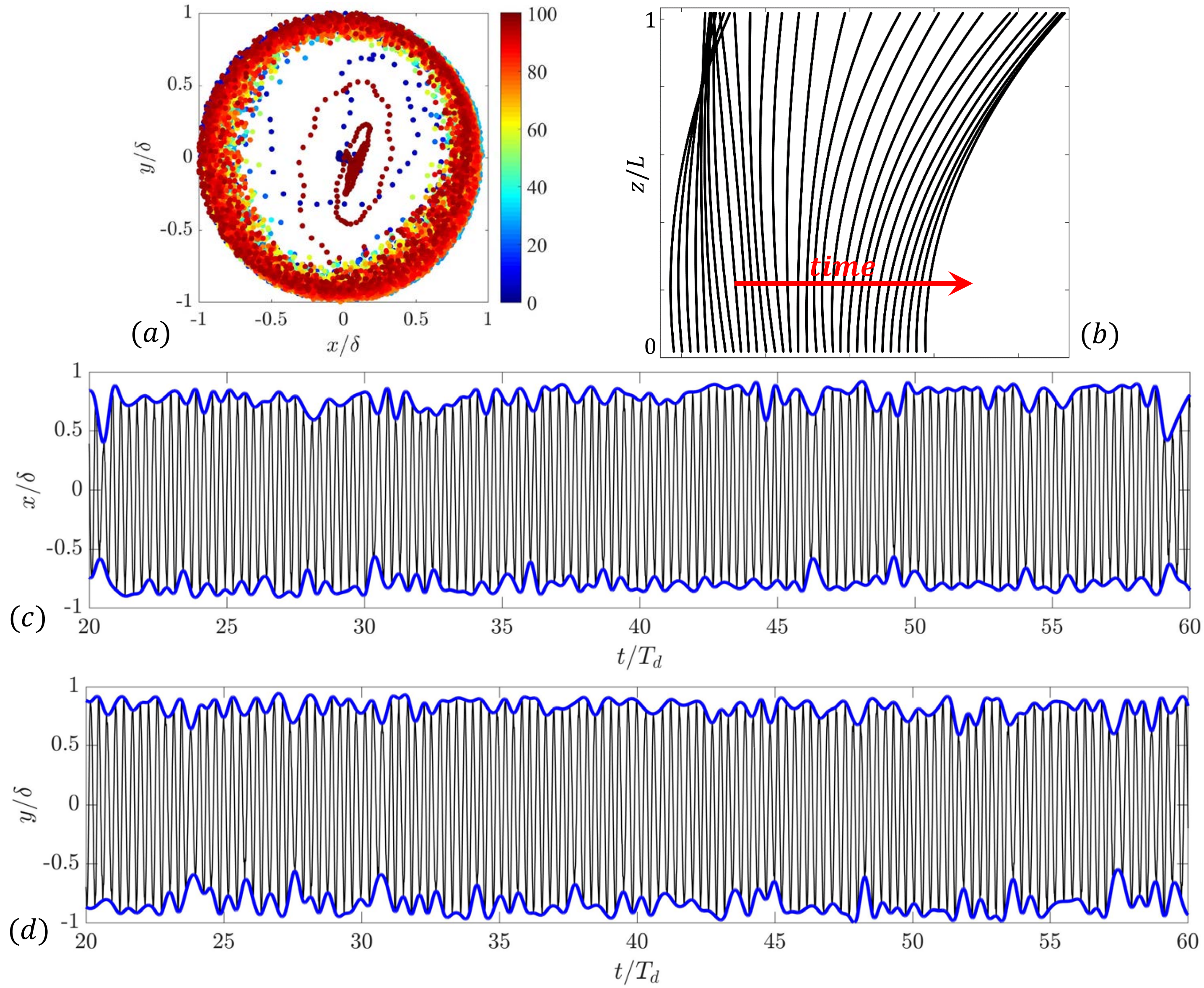

Figure 3.1: Rotational response; **a**. The trajectory of top of the column. Displacements in x and y directions are scaled by δ. The colorbar is the dimensionless time t/T_d. **b**. Snapshots of column deflection during an orbit. **c**. The corresponding time series in x direction, and **d**. The corresponding time series in y direction. Blue lines are upper and lower peak envelops of displacement time series.

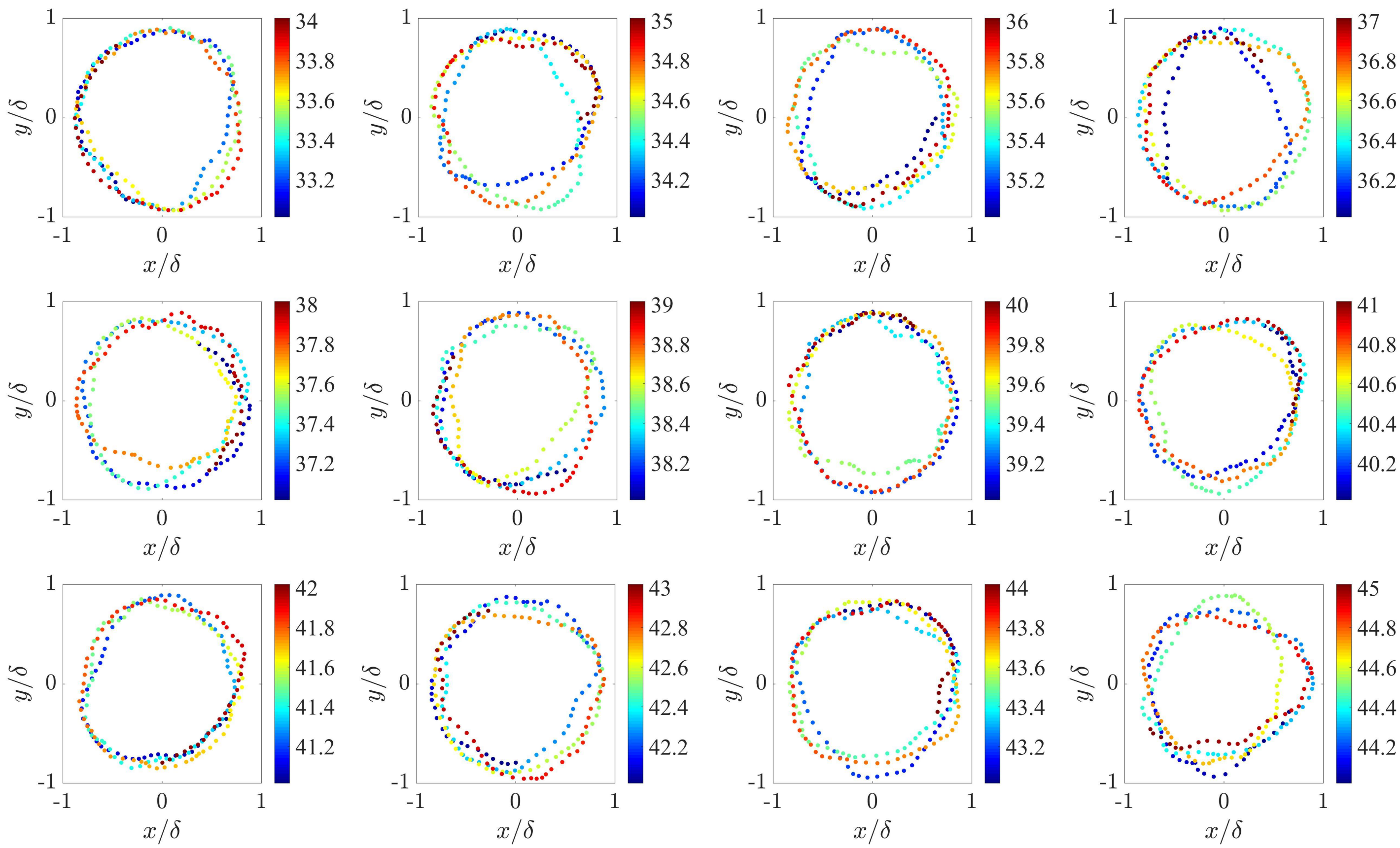

Figure 3.2: Trajectory of top of the column in a rotational response. Here flow is evenly distributed around the column $e = 0$ and Deborah number is $De = 1.4 \times 10^4$. Each subplot shows the trajectory during one dimensionless time T_d, and the colorbar shows the corresponding time. The column follows approximately constant orbits 2 to 3 times in each time window. Trajectories are similar to each other in each subplot, and the ones in other subplots in terms of radius and aspect ratio. The direction of rotation is constant, i.e. it moves clockwise.

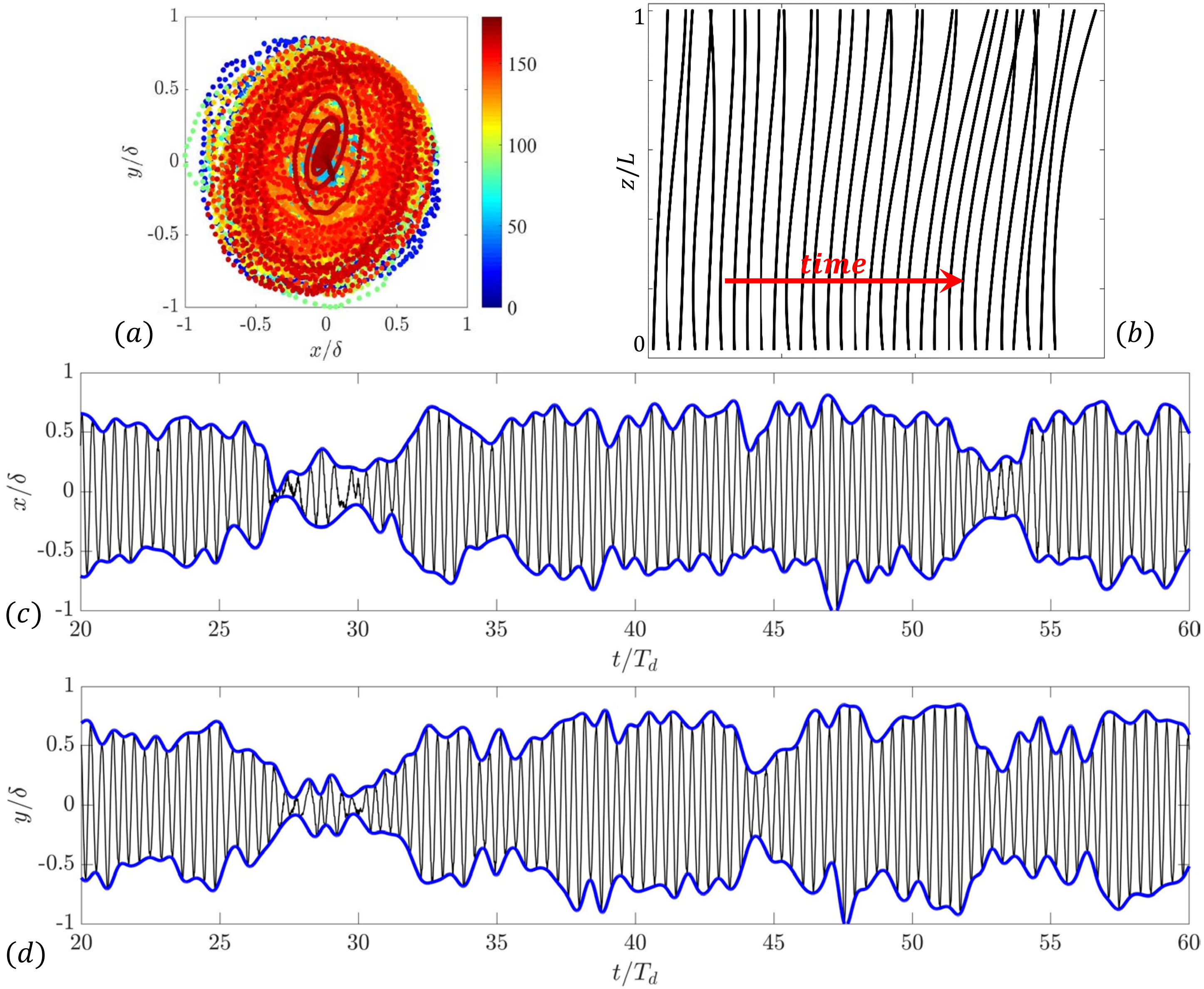

Figure 3.3: Mixed-mode response; **a**. The trajectory of top of the column. Displacements in x and y directions are scaled by δ. The colorbar is the dimensionless time t/T_d. **b**. Snapshots of column deflection during an orbit. **c**. The corresponding time series in x direction, and **d**. The corresponding time series in y direction. Blue lines are upper and lower peak envelops of displacement time series.

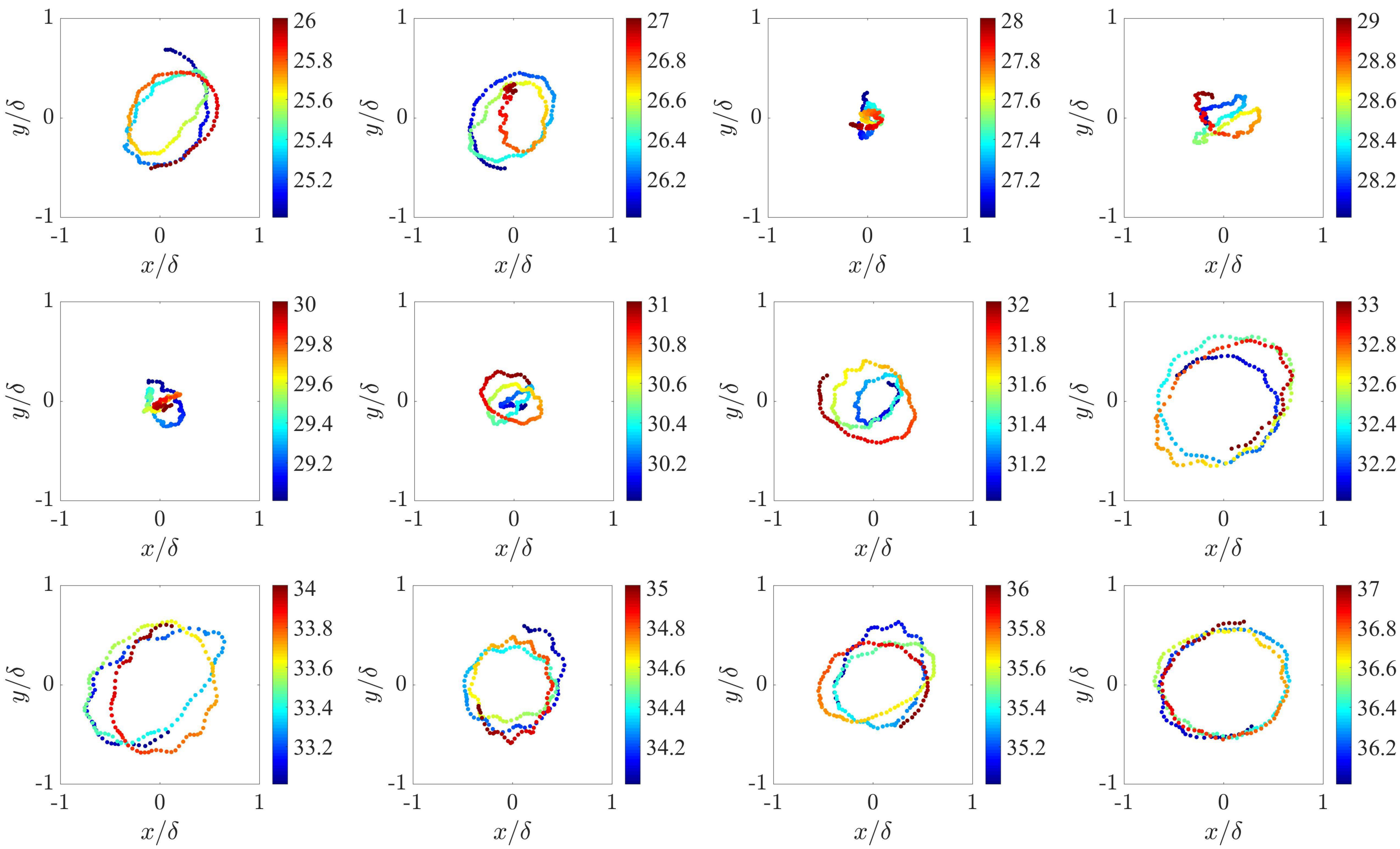

Figure 3.4: Trajectory of top of the column in a mixed-mode response. Flow distribution around the column is approximately even $e = 0.08$ and Deborah number is $De = 6.8 \times 10^3$. Each subplot shows the trajectory during one dimensionless time T_d and colorbar shows the corresponding time. The column mainly follows elliptical and circular orbits, e.g. $t = 25,\ 26,\ 33$ are elliptical orbits while $t = 34$ and 36 are circular. Aspect ratios and radius of ellipses and circles are different from time to time, e.g. the evolution of trajectory from $t = 30$ to $t = 33$ as the orbits are enlarging. Sometimes we observe linear movements, e.g. $t = 28$. Although trajectories change over time but the direction of motion is always the same, i.e. for this example column moves in clockwise direction.

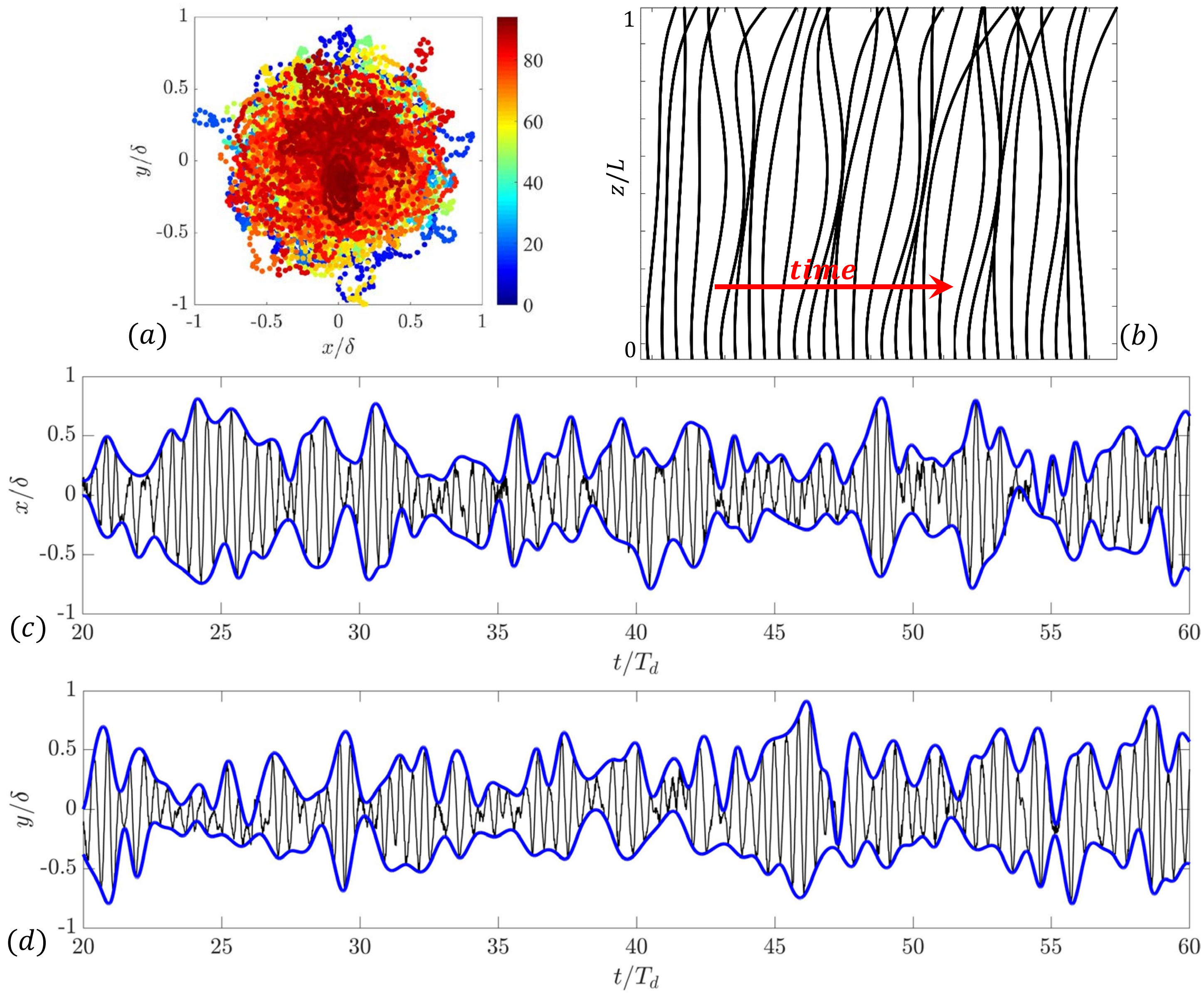

Figure 3.5: Chaotic response; **a**. The trajectory of top of the column. Displacements in x and y directions are scaled by δ. The colorbar is the dimensionless time t/T_d. **b**. Snapshots of column deflection during a cycle. **c**. The corresponding time series in x direction, and **d**. The corresponding time series in y direction. Blue lines are upper and lower peak envelops of displacement time series.

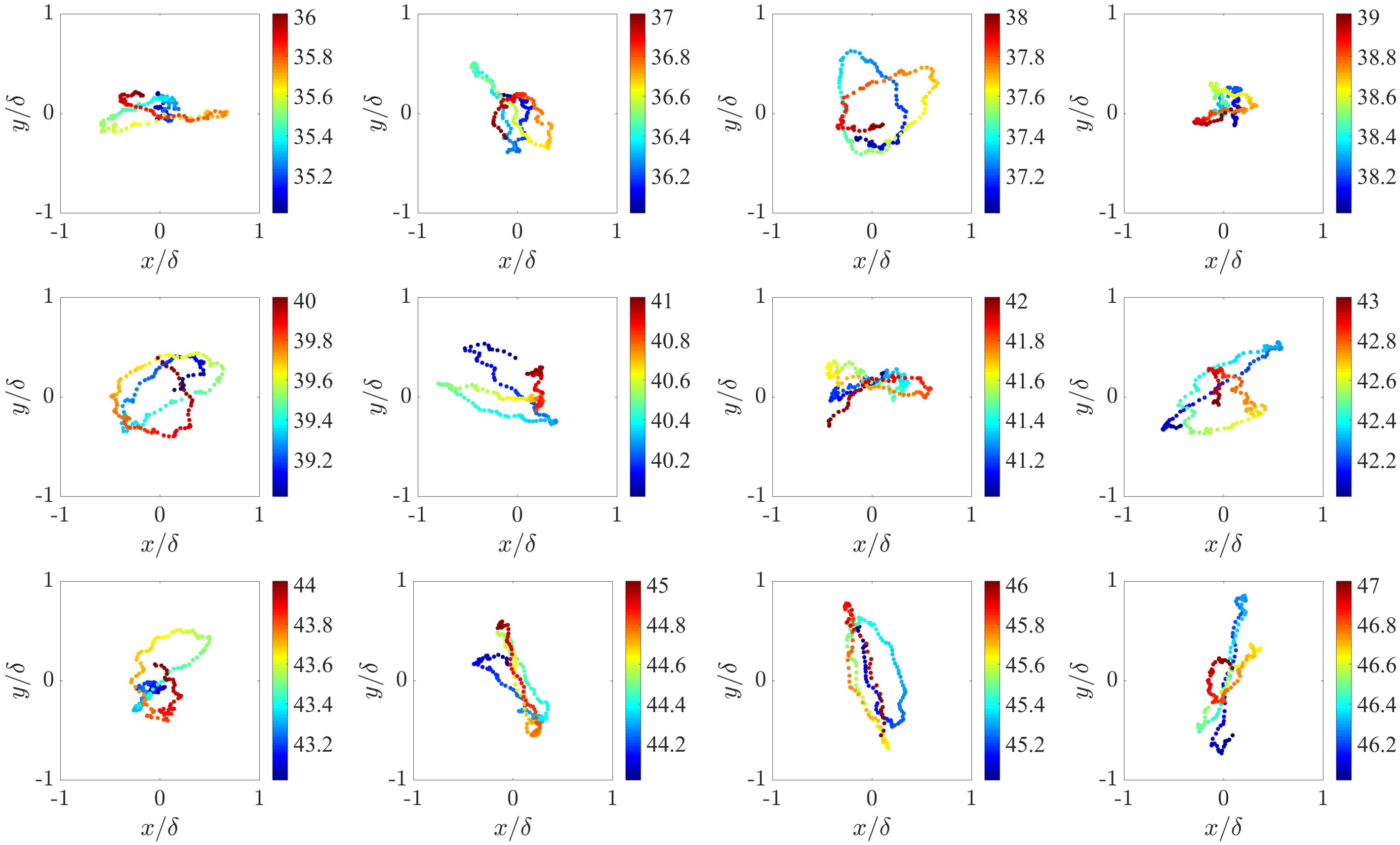

Figure 3.6: Trajectory of top of the column in a chaotic response. Flow distribution around the column is highly uneven $e = 1$ and Deborah number is $De = 75$. Each subplot shows the trajectory during one dimensionless time T_d and colorbar shows the corresponding time. Linear trajectories are the most observed pattern in this figure while the direction of linear trajectories are different, e.g. trajectory at $t = 41$ is parallel to x axis while at $t = 46$ is parallel to y axis. At $t = 40$ and $t = 44$ we see that direction of linear motion changes. There are two elliptical trajectories at $t = 37$ and $t = 39$ while the orientation and size of ellipses are different. Other trajectories are a combination of linear and circular movements in small scales as we see at $t = 36$ or $t = 43$.

3.2 Energy distribution

In this section, we characterize steady-state column motions in terms of the time-varying partitioning of rotational, kinetic, and potential energy (definition in §2.5) in rotational, chaotic, and mixed-mode responses. Our goals are to: **i**. characterize each response in greater detail, **ii**. identify a quantitative metric for end-member rotational and chaotic motions as well as the distinctive properties of the mixed-mode regime.

Figure 3.7 shows time series of these three components of the specific energy E_0 for different motions. During a rotational response (Fig. 3.7 a., the total specific energy and its different components are statistically stationary, fluctuate around an approximately constant value, consistent with predominantly rotational trajectories (Fig. 3.1), KE_{Rot} has the highest contribution to E_0 while KE_{Lin} is the smallest component of the specific energy.

During a mixed-mode response, by contrast, the total specific energy, as well as each energetic component, varies significantly over T_d as well as over much longer time scales. In general, KE_{Lin} is the smallest component of E_0 over time scales $\sim T_d$ and $\gg T_d$ while energy is partitioned approximately equally between PE and KE_{Rot}. A feature of the mixed-mode response is that the column intermittently enters protracted periods marked by rotational motions that are also statistically stationary. For example, over the time interval $39 \leqslant t \leqslant 44$ motions are predominantly rotational and KE_{Rot} is maximized.

Finally, all three components of energy are comparable in magnitude during a chaotic response (Fig. 3.7 c). A marked difference to the rotational and mixed-mode responses is that the contribution of KE_{Lin} can exceed KE_{Rot}.

We use histograms of the distribution of specific energy components for all the experiments in rotational, mixed-mode, and chaotic response respectively, to distinguish the time-averaged properties of each response, Figs. 3.8 a, b, c. During rotational responses, KE_{Rot} is the dominant component of energy with an average of 64% of total specific energy in a range of $55\% < KE_{Rot} < 76\%$. The stored PE is 32% on average with a range of

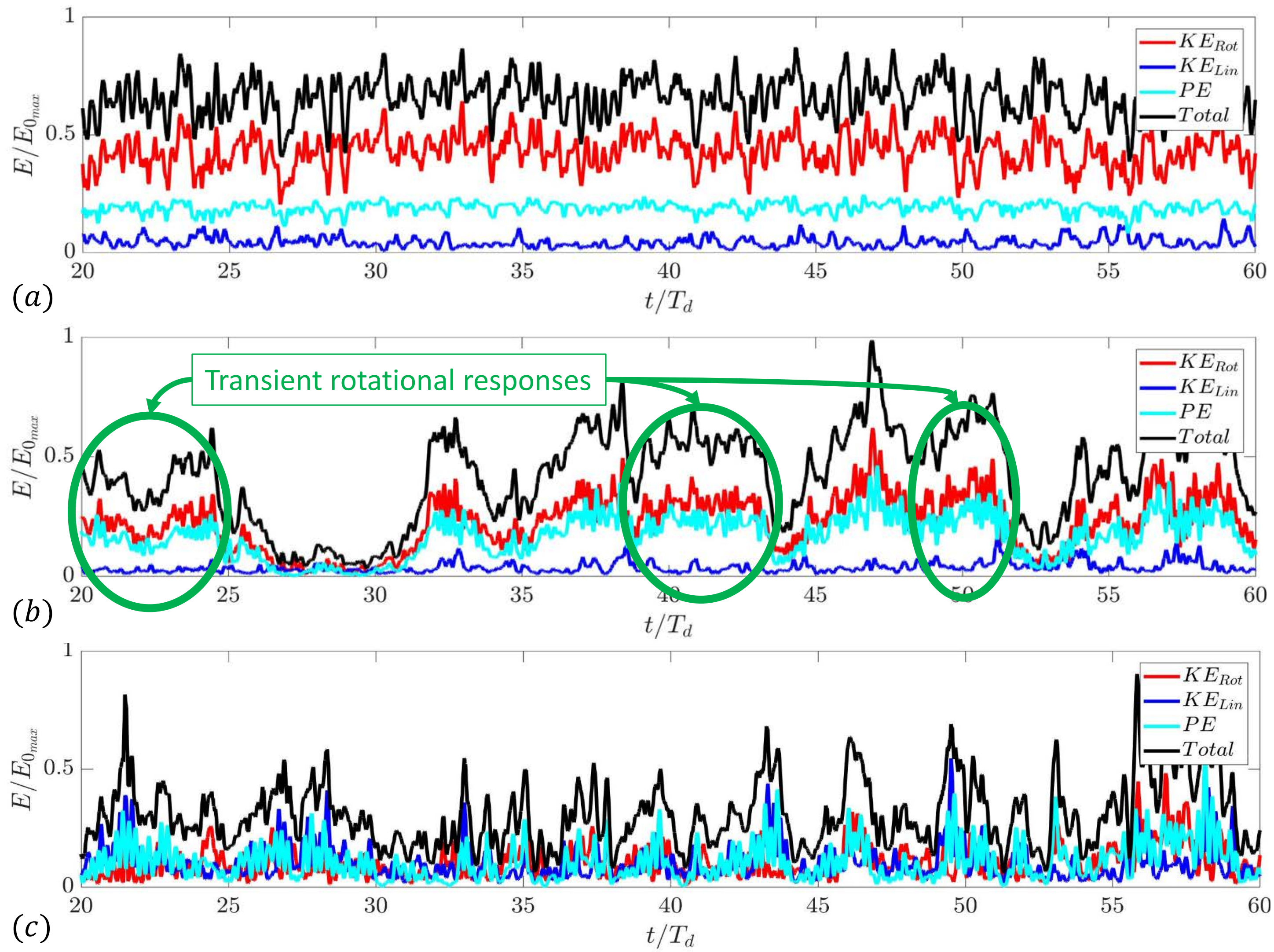

Figure 3.7: **a**. Energy time series in a rotational response. Flow conditions are $e = 0$ and $De = 1.4 \times 10^4$., **b**. Energy time series in a mixed-mode response. Flow conditions are $e = 0.08$ and $De = 6.8 \times 10^3$., **c**. Energy time series in a chaotic response. Flow conditions are $e = 1$ and $De = 75$. Time is scaled with T_d and rotational kinetic energy KE_{Rot}, linear kinetic energy KE_{Lin}, potential energy PE, and total specific energy E_0 are normalized by the maximum of specific energy $E_{0_{max}}$ during each experiment.

Response	$\overline{KE_{Lin}}$	$\sigma_{KE_{Lin}}$	$\overline{PE}$	σ_{PE}	$\overline{KE_{Rot}}$	$\sigma_{KE_{Rot}}$
Rotational	0.04	0.02	0.32	0.06	0.64	0.06
Mixed-mode	0.10	0.01	0.29	0.05	0.61	0.05
Chaotic	0.32	0.07	0.18	0.09	0.50	0.07

Table 3.1: The average and standard deviation of time-averaged energy components for all experiments in each response.

$18\% < PE < 45\%$. The contribution from linear kinetic energy KE_{Lin} 4% on average with a range of $1\% < KE_{Lin} < 8\%$ (Fig.3.8 a).

In a mixed-mode response, similar to the rotational mode, energetic components are distinct in mixed-mode response and KE_{Rot} is the dominant component of energy with an average of 61% in a range of $51\% < KE_{Rot} < 68\%$. The stored PE is 29% on average with a range of $22\% < PE < 40\%$. The linear kinetic energy KE_{Lin} contributes 10% on average and varies in $7\% < KE_{Lin} < 12\%$ (Fig.3.8 b).

In contrast to the rotational and mixed-mode responses, energetic components of a chaotic modes are comparable to each other. The rotational kinetic energy KE_{Rot} with an average of 50% varies in $21\% < KE_{Rot} < 71\%$. The potential energy PE with the average of 18% changes between $1\% < PE < 68\%$. The kinetic linear energy KE_{Lin} contributes 33% on average with a range of $10\% < KE_{Line} < 47\%$ (Fig.3.8 c). We present the average value and standard deviation for time-averaged components of specific energy during all experiments in each mode in Table 3.1.

To summarize, we observe in §3.1 that circular orbits are the main pattern in rotational responses and linear displacement is the dominant motion in chaotic motions. In addition, consistent with these kinematic observations we show that the contribute of linear kinetic energy to total motion increases form rotational to chaotic responses while rotational components of energy are still the dominant energy components. To quantify this behavior we now use ER, defined in §2.5, as a metric to distinguish between different responses. Figure 3.8 d. shows energy ratio $ER = KE_{Lin}/KE_{Rot}$ distribution for three responses and dashed lines represents the fitted Gaussian curves

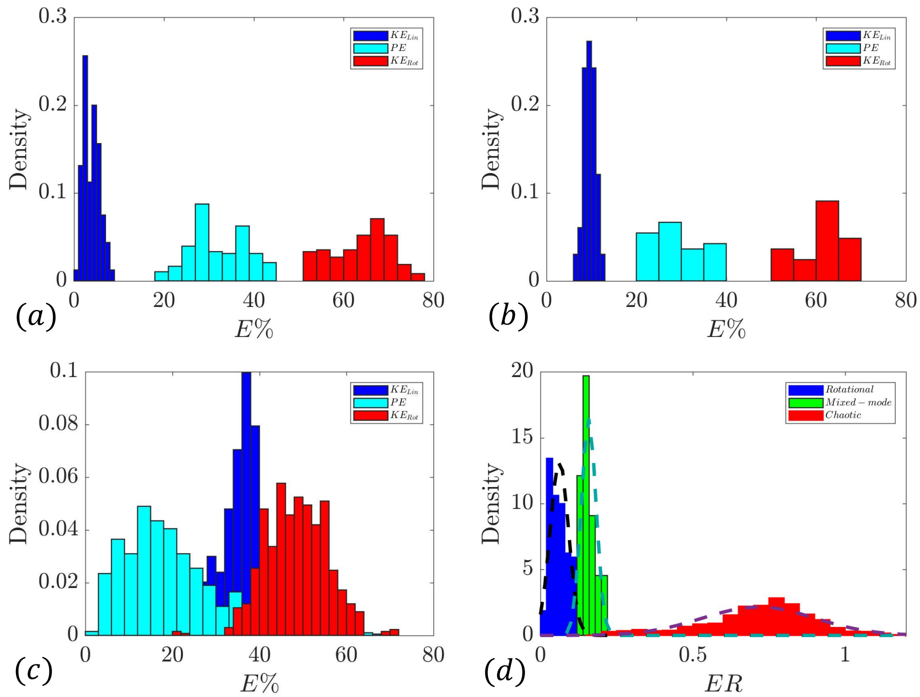

Figure 3.8: Distribution of time-averaged specific energy components for all the experiments in **a**. rotational responses, **b**. mixed-mode responses, and **c**. chaotic response. **d**. Distribution of energy ratio ER for different motions. Dashed lines are fitted Gaussian curves to ER distributions, detail in Table 3.2.

to the ER distribution in each one. The energy ratio ER for rotational motions varies in $0.01 < ER < 0.12$ with the average of 0.06. Mixed-mode response is observed with ER in the range of $0.12 < ER < 0.22$ and its mean value is 0.16. Chaotic modes occur over a broad range of energy ratio $ER > 0.20$. The average of ER for chaotic motions in our experiments is 0.71. The mean value and standard deviation corresponding to the fitted curves is represented in Table 3.2.

Response	$\overline{ER}$	σ
Rotational	0.06	0.03
Mixed-mode	0.16	0.02
Chaotic	0.71	0.19

Table 3.2: The average value of energy ratio ER and its standard deviation for different responses.

3.3 Spectral analysis

The time series of trajectories in §3.1 and energetic analysis in §3.2 show that rotational as well as linear oscillations occur in response to the forced airflow. Accordingly, in this section, we use spectral analysis of both displacement and accelerometer time series to characterize the periodic parts of the motions in all three responses.

Figure 3.9 shows the normalized power spectrum of time series of trajectory and normalized power spectrum of time series of accelerometer data for three examples in different responses in black and red color, respectively. We normalize the frequency axis with the damped natural frequency of the column, f_d, to make clear the damping natural frequency (see Fig. 2.7) and the higher frequency oscillation related to the air forcing. The frequency response characteristics of accelerometers preclude our ability to resolve frequencies as low as the damped frequency of columns f_d. Consequently, to capture the full column response, we combine both time series. We record videos of top displacement with a rate of 29.97 fps. Therefore, its Nyquist frequency is 15 Hz, while accelerometers record 90 samples in a second, and its Nyquist frequency is 45 Hz. And they can record higher frequency vibrations than what a video can capture.

Figure 3.9 shows that periodic motions exist in all three examples. There are three peak frequencies that are roughly at $1 \times f_d$, as well as $10 \times f_d$, and $25 - 30 \times f_d$. Note, f_d is the natural frequency of the system (Fig. 2.7). For all the responses, the second and third peaks have lower power than the first peak, but the ratio of second and third peak power to the first peak for chaotic response is greater than mixed-mode and rotational response.

Figure. 3.10 shows the normalized power spectrum of all the experiments in each response, a. rotational, b. mixed-mode, and c. chaotic. In rotational responses, the first peak corresponding to f_d occurs at $1-2 \times f_d$. On average, the second higher frequency peak related to the air forcing is approximately 10% of the first peak power (Fig. 3.10 a). Similar to rotational mode, in a mixed-mode response, the damped natural frequency is at $1-2 \ \times f_d$ and, on average, the second peak power is approximately 15% of the first peak power (Fig. 3.10 b). The damping natural frequency in chaotic responses is broader compared to rotational and mixed-mode regimes, and the second peak power is,on average, is 30% of the first peak power which has a higher value than the other two responses.

3.4 Regime diagram

We introduced rotational, mixed-mode, and chaotic response to different airflow conditions in §3.1. Then we explored differences between these motions in terms of the energy content of top trajectories in §3.2. Here we investigate the column response in terms of the trajectory of top of the column and its energy content to the airflow eccentricity e and intensity De.

Figure 3.11 summarize the response characteristics of all the experiments carried out with four columns in our study in terms of trajectory type and energy ratio ER to the airflow eccentricity e and intensity De. For symmetric forcing $e = 0$, as De is increased, initially chaotic mode is dominant, transition to mixed-mode response emerge at $De > 6 \times 10^3$, and the column response evolve to be predominantly rotational for $De > 10^4$. If forcing eccentricity is increased to 0.5, $e < 0.5$, the transition from chaotic response to mixed-mode and rotational remains similar to symmetric forcing, $e = 0$, with gradual increase in De threshold for a predominantly rotational response. For high forcing eccentricities, $e > 0.5$, all trajectories are in chaotic response. In general, energy ratio ER at a fixed e increases by decreasing De.

As we discussed in Chapter 2, we run experiments using four different

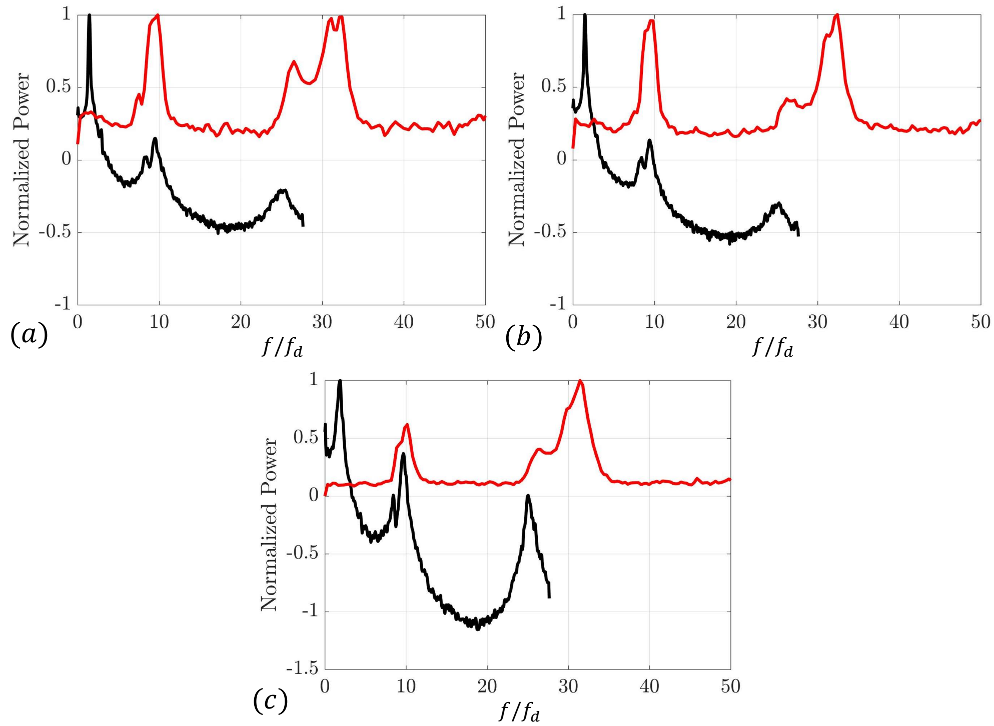

Figure 3.9: Example of Power spectrum for **a**. rotational, **b**. mixed-mode, and **c**. chaotic response. Red lines are from spectral analysis of accelerometers data and black lines come from spectral analysis of trajectory time series. The frequency is normalized by the damped frequency of the column f_d.

columns with different elastic and damping properties, Table(2.4). Figures 3.12, 3.13, 3.14, and 3.15 show the individual responses of columns $C1$, $C2$, $C3$, and $C4$ to different forcing scenarios, respectively. Note, we have defined a characteristics number for each column as $\gamma = T_d\omega_n$, see equation 2.6, representing the ratio of damping and natural oscillation time scales. In our experiments, the lowest value of $\gamma = 8.15$ belongs to columns $C1$ and $C4$ while $C1$ has the shortest relaxation time, $T_d = 2.38$ s, and $C4$ has the longest oscillation time, $2\pi/\omega_n = 3.85$ s. The column $C2$ has the shortest oscillation time, $2\pi/\omega_n = 1.44$ s. The maximum value of $\gamma = 14.1$

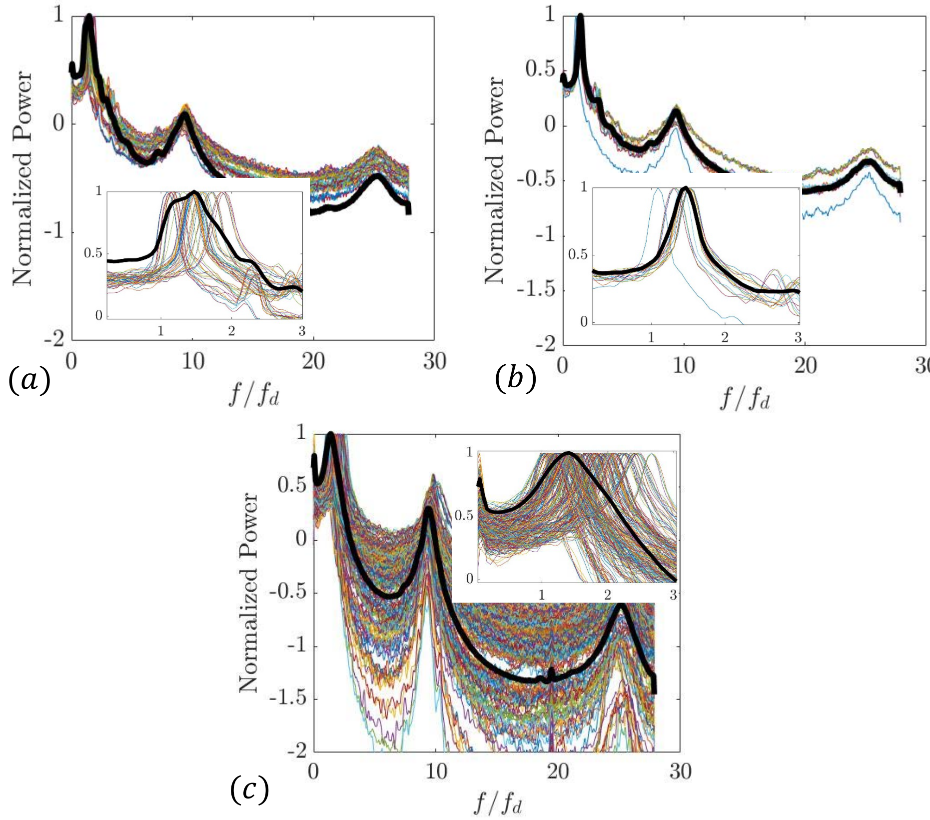

Figure 3.10: Power spectrum of all the experiments in **a**. rotational, **b**. mixed-mode, and **c**. chaotic response. The solid black line represents the average value power spectrum for all the experiments in each mode. The frequency is normalized by the damped frequency of the column f_d.

and relaxation time, $T_d = 6.66$ s, belongs to column $C3$.

The response of the column with the shortest relaxation time ($C1$) to airflow with high eccentricities $e > 0.5$ is chaotic while in low eccentricities $e < 0.5$ all three responses are observed (Fig. 3.12). Rotational solutions are more favorite for high De and low eccentricity e while some mixed-mode solutions occur for mid-range values of eccentricity $0.15 < e < 0.45$ and mid-range forcing intensity $7 \times 10^3 < De < 1.8 \times 10^4$. For experiments at

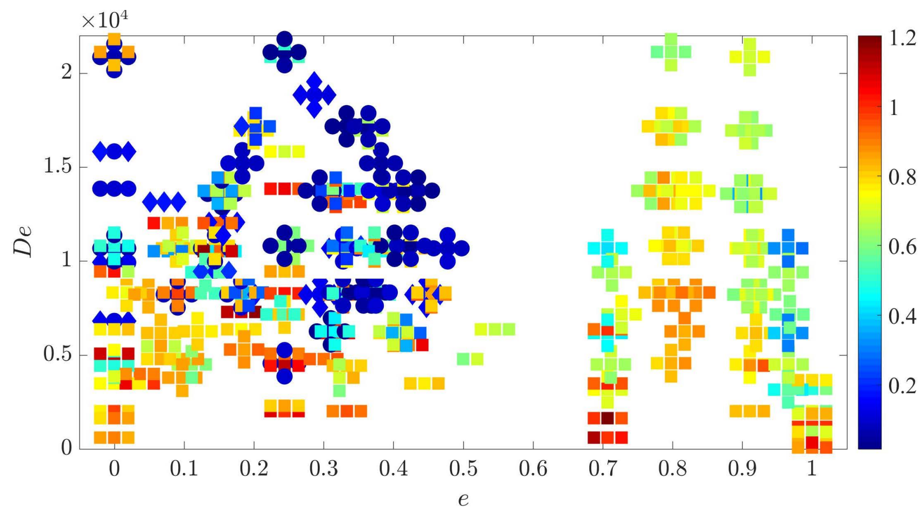

Figure 3.11: Effects of forcing eccentricity e and intensity De on column responses. Shapes represents responses as: ◯ is rotational, ◇ is mixed-mode, and □ is chaotic response. The colorbar shows the value of ER.

the area of $e > 0.5$ the energy ratio ER decreases by increasing De for a constant e.

Similar to column $C1$, all the responses of column with the shortest oscillation time ($C2$) for high airflow eccentricity $e > 0.5$ are chaotic and ER decreases by increasing flow intensity De by fixing flow eccentricity e. Rotational solutions are observed in a limited forcing properties of $0.2 < e < 0.5$ and $De > 0.5 \times 10^4$. In contrast to column $C1$, all $C2$'s motion at symmetry forcing $e = 0$ are chaotic.

Rotational responses for the column with longest damping time ($C3$) occur only at $e = 0,\ De = 1.4 \times 10^4$ and $e = 0, De = 1 \times 10^4$ (Fig. 3.14) and mixed-mode responses are observed by slight increase in eccentricity $e = 0.09,\ De = 1.3 \times 10^4$ or decrease in intensity of forcing $e = 0,\ De = 0.7 \times 10^4$ compared respectively to rotational responses. ER increases from its minimum at low eccentricity $e = 0$ and high intensity $De = 1.4 \times 10^4$ to its maximum at high eccentricity $e > 0.7$ and low intensity $De < 0.3 \times 10^4$.

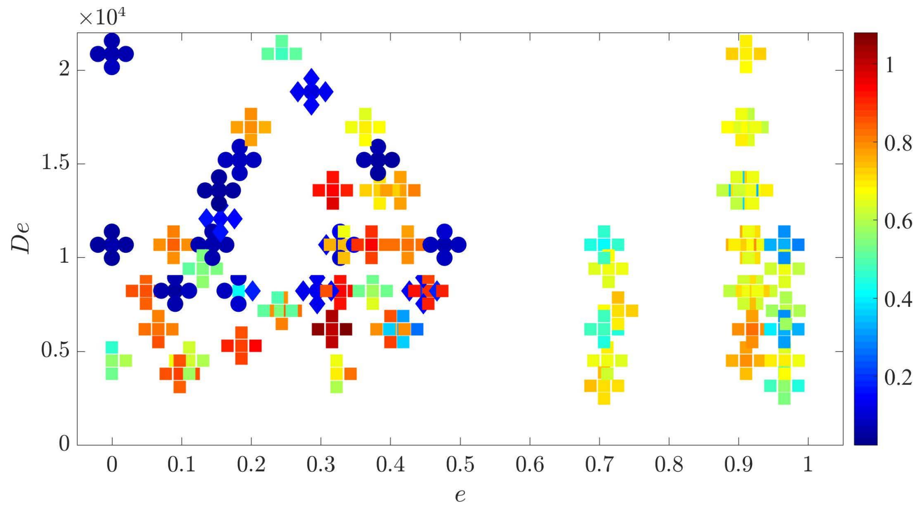

Figure 3.12: Effects of forcing eccentricity e and intensity De on C1 responses. Shapes represents responses as: ◯ is rotational, ♢ is mixed-mode, and □ is chaotic response. The colorbar shows the value of ER.

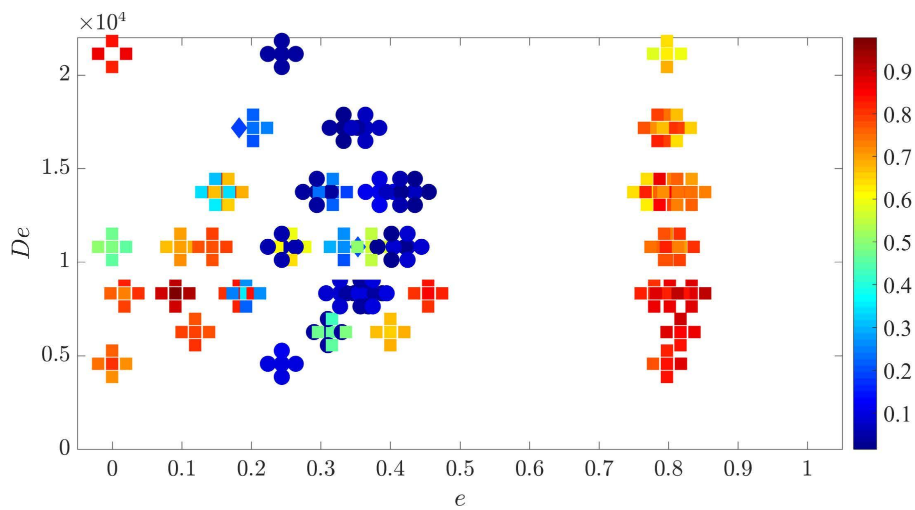

Figure 3.13: Effects of forcing eccentricity e and intensity De on C2 responses. Shapes represents responoses as: ◯ is rotational, ♢ is mixed-mode, and □ is chaotic response. The colorbar shows the value of ER.

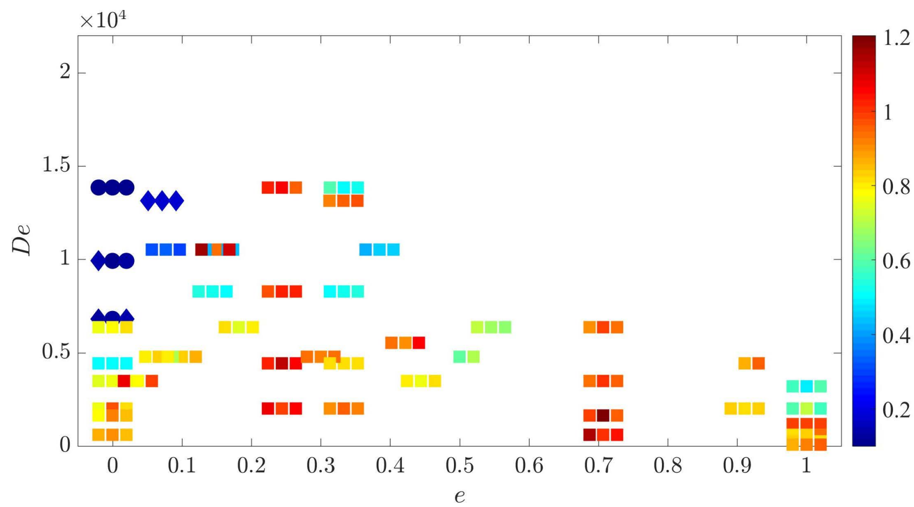

Figure 3.14: Effects of forcing eccentricity e and intensity De on C3 responses. Shapes represents responses as: ◯ is rotational, ♢ is mixed-mode, and □ is chaotic response. The colorbar shows the value of ER.

Similar to column $C3$, the column with longest oscillation time ($C4$) responses chaotically to different airflows except at symmetry airflow $e = 0$ and high forcing intensity $De = 1.6 \times 10^4$ which its response is rotational/mixed-mode and at $e = 0.15$ and $De = 1 \times 10^4$ which its response is mixed-mode.

3.5 Discussion of experimental results

In this discussion we first overview different classes of responses and their properties. We then address: **i**. the significant role of airflow eccentricity e in dictating the class of column response; **ii**. the effect of De on the column response for a symmetric airflow with $e = 0$; and **iii**. some unexpected results observed in Fig. 3.11 where there are chaotic responses with symmetric airflow and high De.

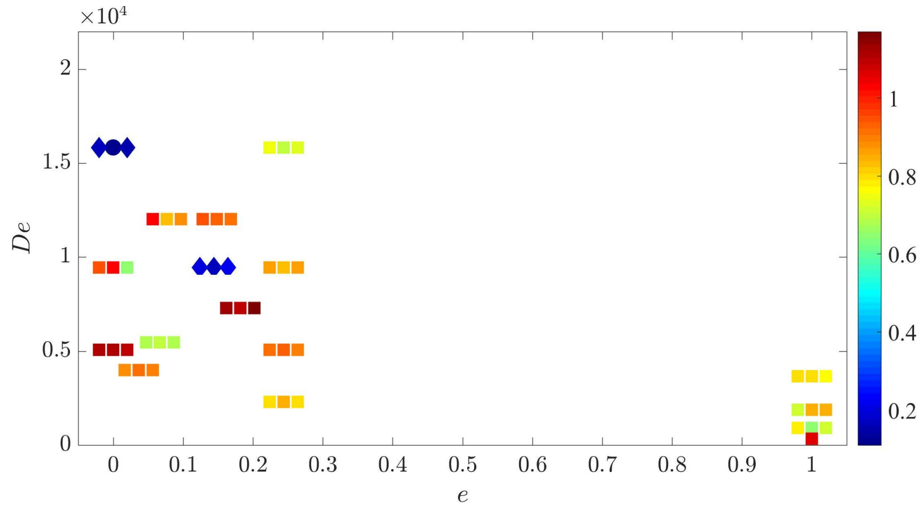

Figure 3.15: Effects of forcing eccentricity e and intensity De on C4 responses. Shapes represents responses as: ◯ is rotational, ◇ is mixed-mode, and □ is chaotic response. The colorbar shows the value of ER.

3.5.1 Overview

In this chapter, we first introduced rotational, chaotic, and mixed-mode responses. Next we characterized different classes of responses based on characteristic differences in displacement, acceleration, and specific energy time series. A column in a rotational mode follows approximately constant orbits, has low energy ratios, $ER < 0.1$, and its energetic components are statistically stationary. In contrast to rotational responses, a column with a mixed-mode response follows orbits that shift and change over a range of time scales, and is marked by higher energy ratios than rotational mode, $0.1 < ER < 0.2$. The energetic content of top trajectory in a mixed-mode response vary over short and long time scales with some intermittent periods of statistically stationary. A chaotic response mainly consists of linear displacements with large variations in the amplitude of oscillation. A wide range of energy ratios, $ER > 0.2$, is observed in a chaotic response while corresponding energetic components of top trajectory vary significantly over time scales of $\sim T_d$.

Vertical deflections along the column are distinct for each mode. Whereas, the deflection is monotonic in a rotational response (Fig. 3.1 b), it is spatially periodic for a mixed-mode response (Fig. 3.3 b) and is complex during a chaotic regime(Fig. 3.5 b). Comparing the time series of top displacement of rotational, mixed-mode, and chaotic responses (Figs. 3.1 c,d, 3.3 c,d, 3.5 c,d) shows that a rotational response has the largest total amplitude of the deflection, while the variability of the amplitude is minimized. On the other hand, chaotic responses occur with the minimum amplitude of the deflection and maximum variability of amplitude.

Comparing spectral analyses of displacement time series at steady-state regime (Figs. 3.9 and 3.10) with corresponding time series in damping regime (Fig. 2.7) shows that mechanical energy is transferred to the column at frequencies which are higher than the damped natural frequency of the column. To sustain the varied classes of motion in steady-state regimes, this energy is transferred to lower frequency, longer wavelength wagging (a reverse energy cascade).

We define the ratio Π of the power of the higher frequency second peak ($f \approx 10f_d$) to the first peak ($f \approx f_d$) corresponding to the damped natural frequency. Whereas for a rotational response $\Pi \approx 0.1$, for mixed-mode and chaotic responses, $\Pi \approx 0.15$ and $\Pi > 0.3$, respectively. This difference in Π reflects the efficiency of energy exchange from higher frequency to lower wagging frequency. That it is maximized for the rotational mode, consistent with low energy ratio ER, indicating virtually all available kinetic energy is transferred to drive rotational orbits.

3.5.2 Effects of forcing eccentricity e on column response

A key result from Figs. 3.11-3.15 is that wagging motions are always chaotic for $e > 0.5$. Furthermore, for $e < 0.5$, natural rotational modes are only preferred for High De. Thus, the key control over the character of wagging is e. We now discuss aspects of the underlying mechanics.

Figure. 3.16 shows a column in symmetric airflow, if the column is in resting position flow is distributed evenly adjacent to the column and the imposed restoring pressure force is equal in every direction. When the column is displaced from its balance position to its left, the symmetric airflow is disturbed and because of the conservation of volume air speeds up at the left side of the column while it decreases at the right side. Consequently, from conservation of energy expressed through Bernoulli equations applied at specified heights on the left and right sides

$$p_l + \frac{1}{2}\rho_0 v_l^2 = p_r + \frac{1}{2}\rho_0 v_r^2, \tag{3.1}$$

where p and v represents flow pressure and velocity and subscripts l and r correspond to the left or right of the column, causes the pressure to decrease at the left side and increase at the right side of the column. This pressure difference introduces a net force to the left side (the Bernoulli effect) and pushes the column further until elastic potential energy stored in the column balances the flow-induced kinetic energy. An oscillation to the right occurs, in response, where the resulting elastic force drives the column back beyond its initial resting position. Through this column movement, velocity increases at the right side and decreases at the left side, causing the net pressure pushing the column to the right. Again, the column deflects to the right until elastic potential energy in the column balances the flow-induced kinetic energy. The symmetric inflow implies a symmetric restoring pressure-force and leads to similar column displacements for both sides of the column.

In this symmetric airflow condition if initial displacement of the column occurs in two perpendicular directions, two independent simultaneous oscillations of the same frequency occur. The superposition of these simple harmonic motions can produce elliptical or circular shapes depending on the difference in amplitude and phase of the oscillations [14]. If the initial phase difference is $\pi/2$ or $3\pi/2$, the motion is circular for the oscillations with same amplitude. The initial phase difference of 0, π, or 2π results in a linear motion. For other values of phase differences an elliptical trajectory is gained. Consequently, maintaining these oscillations produce rotational responses.

Where asymmetric airflow is imposed at the tank base, by contrast, the flow distribution around the column and resulting net pressure force at its resting position is not uniform. In Fig. 3.17, the pressure at the right side of the column is higher than the column's left side due to its lower flow velocity through equation 3.1. The resultant net pressure force pushes the column to the left and the resting position of the column moves to the left. If the column displaces from the new resting position, similar to symmetric airflow condition, column will oscillate. Since the column oscillation center is on the left of the channel centerline, the amplitude of column displacement from its original resting position is greater in the left direction than the other.

Extending asymmetric airflow condition problem to three dimensions can result in different trajectories [14]. In this case, the superposition of top column displacement at two perpendicular directions with amplitudes, and phases can lead to variety of trajectories.

3.5.3 Effects of forcing intensity De on column response

We have observed from time series and top trajectories (e.g., Fig.2.3) that after shutting down the airflow, the column is prone to oscillate in a rotational response. When the asymmetric airflow is exerted to the column at the base, it introduces a linear net pressure force which can break the rotational pattern leading to motions that include contributions from linear and rotational displacements. Consequently, column oscillates in a chaotic regime. By contrast, with a symmetric air flux forcing the net pressure force is approximately zero (depending on physical noise). In this special case, neutralized radial pressure forces act to maintain rotational motions. However, we observe rotational, mixed-mode, and chaotic responses with symmetric forcing $e \to 0$. When $e < 0.5$, low airflow intensities (0.6×10^4) favor chaotic responses, and high De leads to an increasing probability of mixed-mode ($De < 10^4$) and rotational modes ($De > 10^4$).

To build understanding, we revisit the steady-state form of the equation of motion for a viscoelastic cantilever beam (equation 2.21) representing

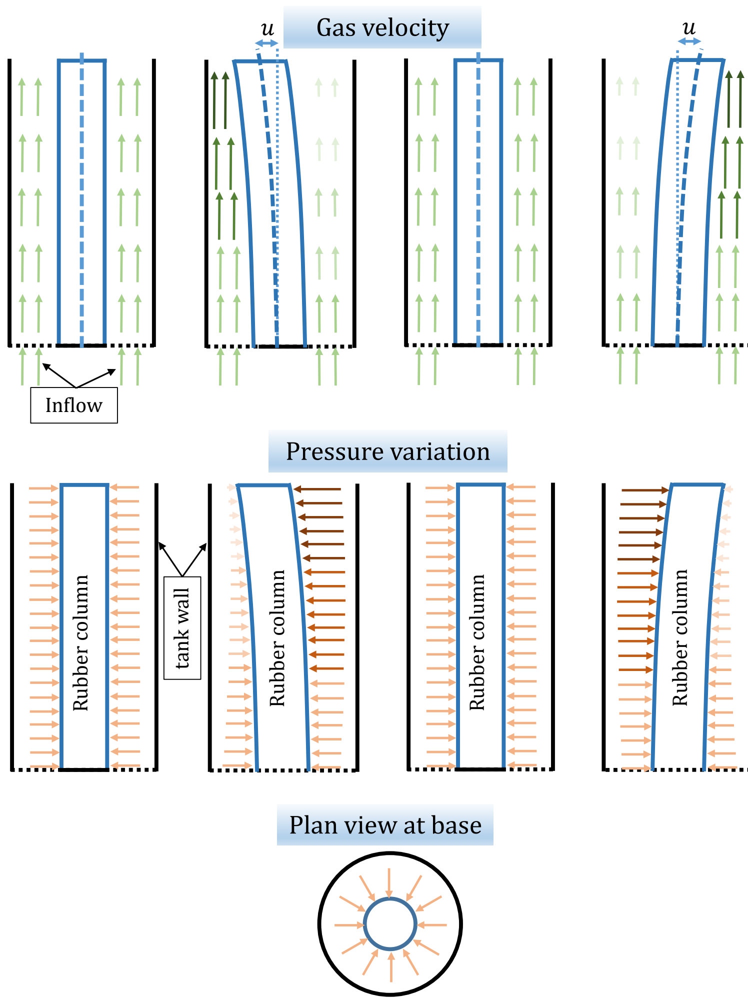

Figure 3.16: Schematic of gas velocity and pressure variation around rubber column, and imparted pressure at the inlet for a symmetric airflow condition. Longer arrows and darker colors represent bigger magnitude of flow velocity and pressure forces. Note, imposed gas pressure force at base acting on a deflected column is always symmetric.

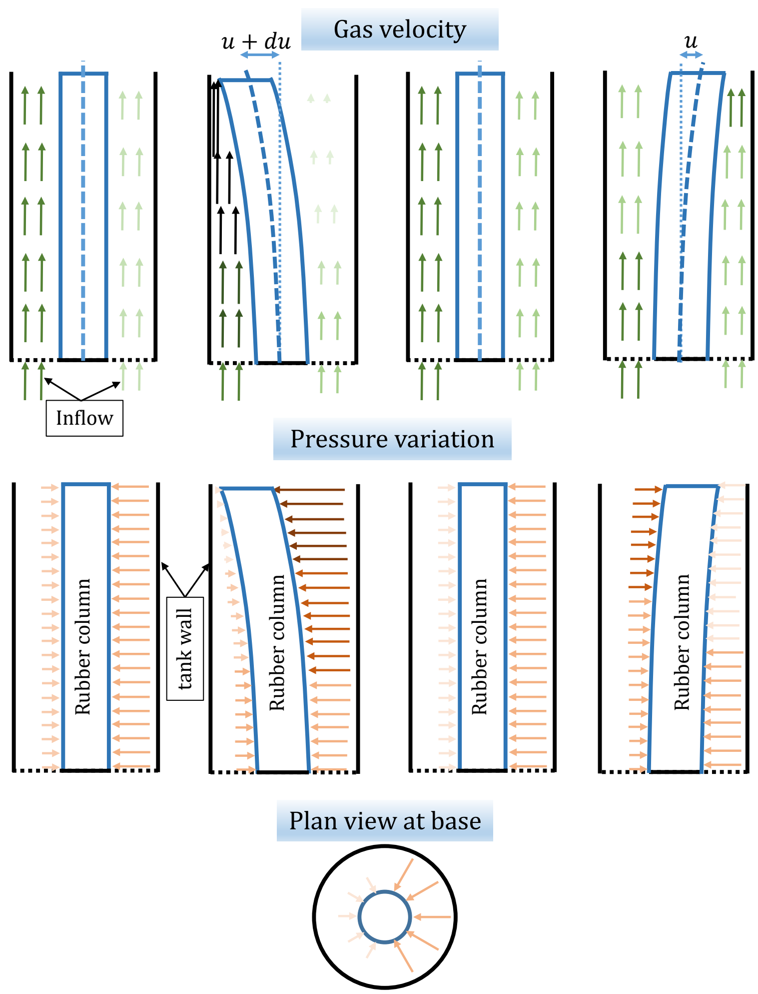

Figure 3.17: Schematic of gas velocity and pressure variation around rubber column, and imparted pressure at the inlet for an asymmetric airflow condition. Longer arrows and darker colors represent bigger magnitude of flow velocity and pressure forces. Note, pressure variations imparted at base are not symmetric. Even if the column would prefer a rotational mode, this inlet condition always perturbs the column away from axi-symmetry.

the experimental model. In the steady-state regime the equation of motion reduces to:

$$\frac{\partial^4 u(z,t)}{\partial z^4} + \frac{\rho A}{EI}\frac{\partial^2 u(z,t)}{\partial t^2} = \frac{w\prime(z,t)}{EI} \tag{3.2}$$

where $w\prime$ is the symmetric forcing driven as a result of difference between the time-averaged and spatially uniform supply of mechanical energy to the column and dissipation. We non-dimensionalize equation 3.2 by selecting the gap width δ as the length scale for deflection, column height L as the length scale for z direction along the column, $T = L/V$ as the advective time scale for gas flow where V is the average vertical velocity of the airflow. Defining $u = u'\delta$, $z = z'L$, $t = t'T$, the equation of motion becomes (after dropping the primes):

$$\frac{\partial^4 u}{\partial z^4} + \Omega\frac{\partial^2 u}{\partial t^2} = w\ \frac{L^4}{\delta}, \tag{3.3}$$

Where

$$\Omega = (\frac{AL^2}{I})(\frac{\rho V^2}{E}). \tag{3.4}$$

Ω is proportional to the ratio of total kinetic energy in the flow ($\propto V^2$) to the elastic potential energy ($\propto E$), and to the Deborah number $\Omega \propto De$. In the limit of high De, equation 3.3 reduces to

$$\frac{\partial^2 u}{\partial t^2} = w\ \frac{L^4}{\delta\Omega}, \tag{3.5}$$

which represents column acceleration. In this case, the flow time scale is shorter than the time scale for the column to react, oscillations can grow and a rotational response which corresponds to maximized amplitude of the oscillation occurs. In the limit of low De, by contrast, equation 3.3 reduces to

$$\frac{\partial^4 u}{\partial z^4} = w\ \frac{L^4}{\delta}, \tag{3.6}$$

which represents a bend in the column. In this case, the flow time scale is larger than the column reaction time scale and the kinetic energy delivered to the column is stored as elastic potential energy that is not released over an advective time scale. Consequently, a chaotic response with $e \to 0$ and low De is a superposition of a series of arbitrary free oscillations of columns with initial bending produced over T.

3.5.4 Some unexpected results in $e - De$ space

Figure 3.13 shows that column $C2$'s response is chaotic when airflow is symmetric $e = 0$ although we expect to have rotational responses for $e = 0$ and high intensity flows. To answer this contradiction, we consider that in order to have symmetric airflow, not only the flow should be distributed evenly at the base also the gap width between the column and hollow cylinder δ when the flow is not introduced to the cylinder should be equal in all directions. Second investigations show that for most of the experiments run by column $C2$, the column was not standing straight in the center of the hollow cylinder, and δ was different for different directions. This also can explain why rotational responses are observed at eccentricities in the ranges of $0.2 < e < 0.5$; even though input flow is not perfectly symmetric, but the initial deflection of the column cause flow to be distributed evenly around the column and rotational responses are recovered.

Chapter 4

Numerical Simulations

To better understand and extend aspects of our experimental results related to the control of gas flux intensity and symmetry in forcing, we carry out 2D Cartesian numerical simulations. In particular, consistent with previous studies on the magma wagging model [6, 21] and the result in Chapter 3 we observe two main frequencies: the natural frequency of column oscillation and the higher Bernoulli frequency related to the gas flux forcing. The steady-state regimes for rotational, mixed-mode, and chaotic modes imply also that energy is transferred from the Bernoulli mode to damped natural frequency f_d of wagging, confirming a hypothesis in [6]. Using two-dimensional numerical simulations to complement these results, we explore the effects of total gas flux, physical column properties, and spatial asymmetry in the distribution of gas flux on the spectral properties of wagging behavior.

In this chapter, we first present the governing equations for a 2D elastic column vibrating in response to an imposed gas flow and define related dimensionless control parameters. We then briefly explain the numerical modeling strategy we implement using the COMSOL Multiphysics finite element software package. We present a case study to address the applicability of 2D simulations for understanding wagging frequencies and driving Bernoulli mode. Next, we investigate the effect of different defined dimensionless parameters on the column deflection and pressure and velocity variations around the column. Finally, we present a summary of the chapter.

4.1 Numerical model

To model our experiments, we implement the Fluid-Structure Interaction module of the COMSOL Multiphysics finite element software. The geometry in this study consists of two domains: fluid and solid mechanics domains (Fig. 4.1). The software provides continuity for the displacement and offers a conforming mesh at the coupled interface between flow and solid domains. We solve the initial value-boundary value problem using the $Time - Dependent$ solver to solve unsteady/time-transient problems. The results are post-processed with MATLAB.

We restrict calculations to perfectly elastic column in 2D because the goal is to capture the modes of oscillation generally, the inclusion of damping precludes modes with a period higher than damping time. We discuss this limitation briefly at the end of the chapter.

4.1.1 Geometry and parameters

Figure 4.1 shows a schematic of the geometry of our numerical model. An elastic column with a density of ρ, Young's modulus of elasticity of E, and Poisson's ratio of ν is fixed at the bottom and placed in the middle of a channel. When the column is at rest, the gap width between the column and channel wall is constant and equal to δ at its right and left side. Air with a density of ρ_0 and viscosity of μ enters the channel with the average velocity of V_R and V_L from the right and left inlets and leave the channel from above where its pressure is balanced with the atmosphere. Table 4.1 lists the parameters for each model.

4.1.2 Equations and dimensionless parameters

Elastic column equations:

As with the development of equation 3.2, if we neglect the viscous damping term in equation 2.21, to focus on the oscillation at steady-state regime, as

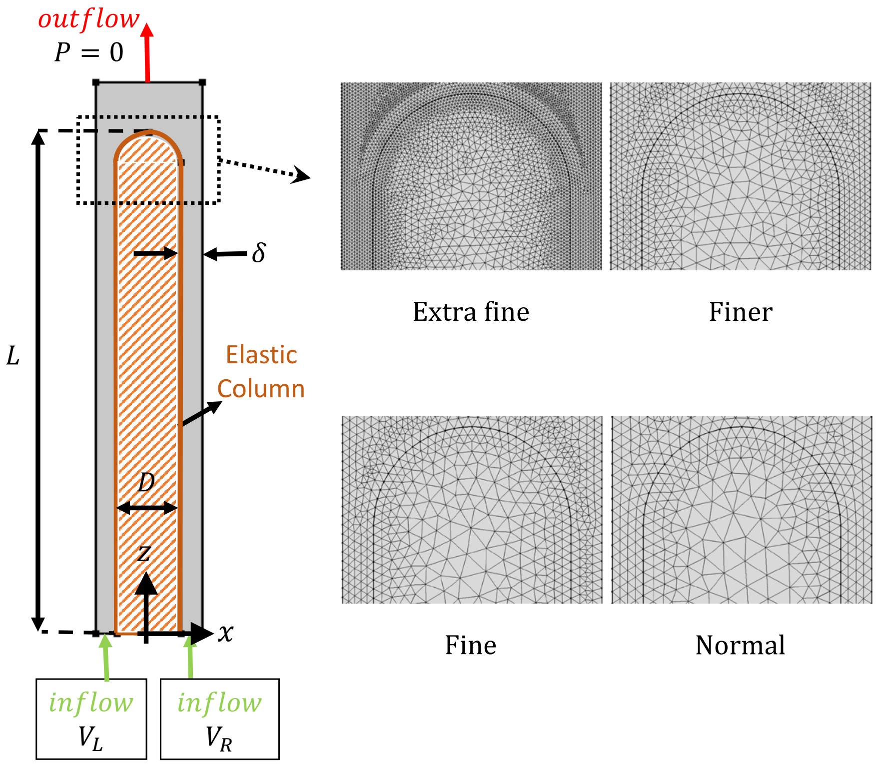

Figure 4.1: Schematic of the model used in COMSOL Multiphysics. An elastic column in dimensions of $D \times L$ is fixed at the bottom. The initial gap width between the elastic column and the surrounding wall is δ. Different types of mesh used in this study, with a number of elements, extra fine mesh: 93940, finer mesh: 22550, fine: 15654, and normal: 9968.

well as effects related to column buoyancy, the equation of motion for an elastic column is [4]:

$$\frac{\partial^2 u(z,t)}{\partial t^2} + \frac{EI}{\rho A}\frac{\partial^4 u(z,t)}{\partial z^4} = w(z,t), \tag{4.1}$$

where ρ is column's density, A is cross-sectional area of column, E is Young's modulus, $I = \pi D^4/64$ is the second moment of inertia, u is deflection of the column, z is the vertical distance along the column from the base, and

Parameter	Descripton
L	Column's height
D	Column's diameter
δ	Gap width
ρ	Column's density
E	Column's Elasticity
ρ_0	Fluid density
μ_0	Fluid viscosity
V_L	Left inlet velocity
V_R	Right inlet velocity

Table 4.1: List of parameters set in the model.

w is force per unit mass applied to the column. We non-dimensionalize equation 4.1 by selecting the gap width δ as the length scale for x direction, column height L as the length scale for z direction, $T = L/V$ as the advective time scale for gas flow where $V = (V_R + V_L)/2$ is the average of input velocities,. In contrast to our treatment of equation 3.2, we also introduce and explicit scale for pressure $\rho_0 V^2$ that enables us to couple the response of the column to the imposed gas flow we discuss next. Defining $u = u'\delta$, $z = z'L$, $t = t'T$, $w = w'\rho_0 V^2/(\rho D)$, the equation of motion becomes (after dropping the primes):

$$\frac{\partial^2 u}{\partial t^2} + K_G \frac{\partial^4 u}{\partial z^4} = w(z)\ \frac{1}{m\epsilon\varepsilon}, \tag{4.2}$$

Where

$$K_G = (\frac{E}{\rho V^2})(\frac{I}{AL^2}), \tag{4.3}$$

is column bending rigidity and indicates the importance of elastic stress (or energy) to the dynamic pressure (kinetic energy) introduced from fluid flow to the column. In this development, note that $K_G = 1/\Omega$ (equation 3.4). $m = \rho/\rho_0$ is the density ratio between column and fluid, and $\epsilon = \delta/L$ and $\varepsilon = D/L$ are aspect ratios in our model. We explicitly non-dimensionalized equation 4.1 in this way to enable m to emerge on the right hand side of the equation as one of the functions of solid-fluid interaction.

Flow equations:

We solve the Navier-Stokes equation and continuity for the fluid phase in our model. The incompressible Navier-Stokes equation and the continuity equation can be written as:

$$\frac{\partial \bar{\mathbf{u}}}{\partial t} + (\bar{\mathbf{u}}.\nabla)\bar{\mathbf{u}} - \frac{\mu_0}{\rho_0}\nabla^2\bar{\mathbf{u}} = -\frac{1}{\rho_0}\nabla P, \tag{4.4}$$

$$\nabla.\bar{\mathbf{u}} = 0, \tag{4.5}$$

where $\bar{\mathbf{u}}$ is the fluid velocity vector, P is the fluid pressure, ρ_0 is the fluid density, μ_0 is the dynamic viscosity, ∇ indicates the gradient differential operator, and ∇^2 is the Laplacian operator. We non-dimensionalize equation 4.4 and equation 4.5 by selecting V and ϵV as the velocity scale in z and x direction, the gap width δ as the length scale for x direction, column height L as the length scale for z direction, $T = L/V$ as the time scale, and $\rho_0 V^2$ for the pressure scale . In this case we define $u_z = u'_z V$ where u_z is flow velocity component in z direction, $u_x = u'_x \epsilon V$ where u_x is flow velocity component in x directions, $x = x'\delta$, $z = z'L$, $t = t'T$, and $P = P'\rho_0 V^2$. if we non-dimensionalize equation 4.4 and equation 4.5 and write them in separate equations for z and x directions we have:

$$\frac{\partial u_z}{\partial t} + u_z\frac{\partial u_z}{\partial z} + u_x\frac{\partial u_z}{\partial x} - \frac{\epsilon}{Re}(\frac{\partial^2 u_z}{\partial z^2} + \frac{1}{\epsilon^2}\frac{\partial^2 u_z}{\partial x^2}) = -\frac{\partial P}{\partial z}, \tag{4.6}$$

$$\epsilon^2(\frac{\partial u_x}{\partial t} + u_z\frac{\partial u_x}{\partial z} + u_x\frac{\partial u_x}{\partial x}) - \frac{\epsilon}{Re}(\epsilon^2\frac{\partial^2 u_x}{\partial z^2} + \frac{\partial^2 u_x}{\partial x^2}) = -\frac{\partial P}{\partial x}, \tag{4.7}$$

$$\frac{\partial u_z}{\partial z} + \frac{\partial u_x}{\partial x} = 0, \tag{4.8}$$

where $Re = \rho_0 V\delta/\mu_0$ is the Reynolds number. If we assume $\epsilon \ll 1$ and $Re \gg 1$, then equation 4.6 and equation 4.7 can be reduced to:

$$\frac{\partial u_z}{\partial t} + u_z\frac{\partial u_z}{\partial z} + u_x\frac{\partial u_z}{\partial x} - \frac{1}{\epsilon Re}(\frac{\partial^2 u_z}{\partial x^2}) = -\frac{\partial P}{\partial z}, \tag{4.9}$$

Parameter	equation	C1	C2	C3	C4
ε	D/L	0.08	0.11	0.07	0.09
ϵ	δ/L	0.006	0.008	0.011	0.014
m	ρ/ρ_0	850	850	850	850
Re	$\rho_0 V D/\mu_0$				
K_G	$EI/(\rho A L^2 V^2)$				
χ	V_R/V_L				

Table 4.2: List of non-dimensional parameters set corresponding to experiments.

$$0 = \frac{\partial P}{\partial x}. \tag{4.10}$$

Final set of equations needed to be solve by COMSOL to find elastic column deflection and flow properties at each time are equations 4.2, 4.8, 4.9, and 4.10. On the basis of these equations, we use non-dimensional parameters listed in Table 4.2 as inputs of each simulation. Also, we introduce $\chi = V_R/V_L$ as the ratio between two inlet velocities. Then COMSOL calculates the corresponding parameters set (Table 4.1) automatically using non-dimensional parameters. The value of each non-dimensional parameter corresponding to viscoelastic rubber column used in experiments is given in Table 4.2.

4.1.3 Boundary conditions

We define two *Inlet*s at the bottom of the channel and introduce a parabolic velocity profile with an average velocity of V_R and V_L for the right and left inlets, respectively. The top of the channel is *Outlet* and is in atmospheric pressure ($P_0 = 0$). The condition at the walls of the channel, as well as the elastic column, is *no slip* condition. The only limitation to elastic column is a *Fixed Constraint* at its bottom which is attached to the channel (see Fig.4.1).

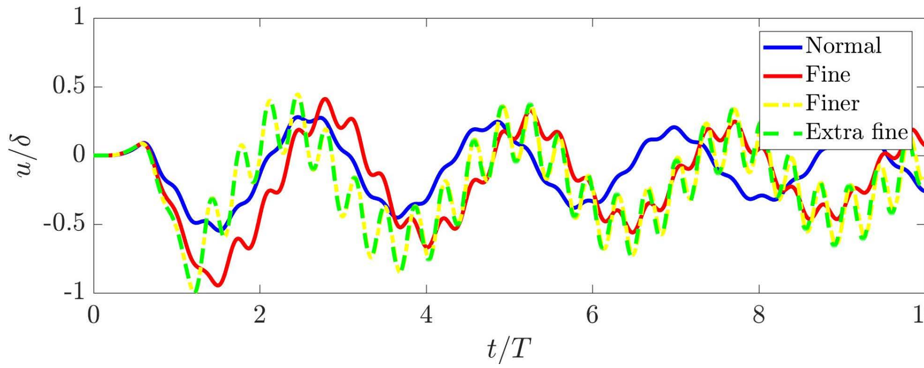

Figure 4.2: Top displacement of the column with 4 different mesh settings. In this model $K_G = 10$, $Re = 1000$, $m = 850$, and $\chi = 0.5$. The time required for each simulation was 45, 125, 224, and 410 min for *Normal*, *Fine*, *Finer*, and *Extra Fine* mesh settings, respectively.

4.1.4 Mesh selection

We use COMSOL's built-in "physics mode" to optimize the mesh design. One of the most important factors to provide an accurate solution is the spatial resolutions of displacements within the column and the column-gas stress coupling. However, mesh density trades with the time required for each simulation. Consequently, we ran a model with four different mesh size settings, *Normal*, *Fine*, *Finer*, and *Extra Fine* (see Fig. 4.2). Based on the results, *Finer* settings and *ExtraFine* settings results are similar, but simulation with *Finer* setting is roughly two times faster than *Extra Fine* simulation. Our choice for the rest of the models will be *Finer* settings.

4.1.5 Solvers and convergence

COMSOL automatically chooses a solver suitable for the modeled physics. In our analysis, the solver is *Fully Coupled* with *Direct Linear Solver*. The linear solver was *MUMPS*, and all the internal parameters of the solver are set automatically.

The time-step for time-dependent analysis was fixed as $dt = T_3/10$ where

$T_3 = 2\pi/\omega_3$ is the period of third natural frequency of the elastic column. This time-step is short enough to capture all the oscillations occur with first three modes of oscillations. COMSOL will take additional steps in between the defined time steps if necessary, e.g., CFL condition.

4.2 Results

In this section, we first present the results of one specific simulation. We then do a parametric study to investigate how defined non-dimensional parameters affect the model and solutions.

For all the simulations we show in this study, we perturb the elastic column from its original resting position in following way; we increase right (or left) inlet velocity from 0 at $t = 0$ to $\approx 2 \times V_R$ (or $2 \times V_L$ for the left inlet) at $t = 0.5 \times T$, where $T = L/\bar{V}$ and $\bar{V} = (V_R + V_L)/2$, then decrease it gradually to a steady value of V_R (or V_L) at $t = T$. We run each simulation for $10T$. Also in this set of simulations we only study dynamic dimensionless variables of Re, χ, m, and K_G, and aspect ratios remain constant as $\varepsilon = 0.07$, and $\epsilon = 0.011$.

4.2.1 A case study

Figure 4.3 shows column displacement at different heights as a function of time. The column vibrates with two distinct frequencies: a high-frequency and low-frequency oscillations. The amplitude of both oscillations increase with height above the column base. Whereas the high-frequency period is $\approx 2T/7$, the low-frequency oscillation period is $\approx 2 \times T$. In general, the column tends to bend toward the left side where the average inlet velocity is two times greater than the average inlet velocity at the right side (note that $\chi = V_R/V_L$).

Figure 4.4 shows the average velocity of the flow at two sides of the elastic column for locations with $L/3$, $2L/3$, and L distant from the inlet. The same oscillations observed in column displacement are observed here while the oscillation amplitude is minimum at the bottom of the channel; it reaches its maximum value around the middle. It then decreases toward

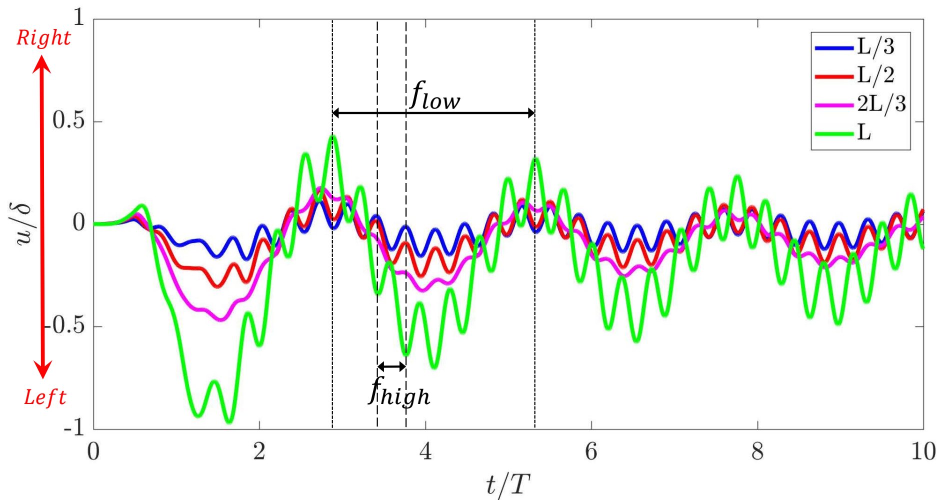

Figure 4.3: Column displacement at $L/3$, $L/2$, $2L/3$, and L distances from the fixed side where L is length of the elastic column. Arrows and dash lines show the period of low- and high-frequency oscillations. Non-dimensional parameters for this simulation are $K_G = 0.1$, $Re = 100$, $m = 850$, and $\chi = 0.5$. y axis is scaled by gap width δ and time is scaled by $T = L/V$.

the top of the channel. Also, after inlet airflow becomes steady ($t = T$), the maximum velocity in one side of the column coincides with the minimum of the velocity on the other side of the column.

Figure 4.5 shows the pressure variation in the flow at two sides of the elastic column for locations with $L/3$, $2L/3$, and L distant from the inlet. Pressure variations that are caused by flow velocity oscillations have the same frequencies as velocity time series. The amplitude of oscillation in pressure time series decrease by moving from base of channel to column top on left or right sides. Pressure variations at a distance of L are minimal in amplitude, and it is very close to atmospheric pressure. Similar to the velocity time series, the maximum of the pressure on one side of the column coincides with the minimum of pressure on the other side of the column.

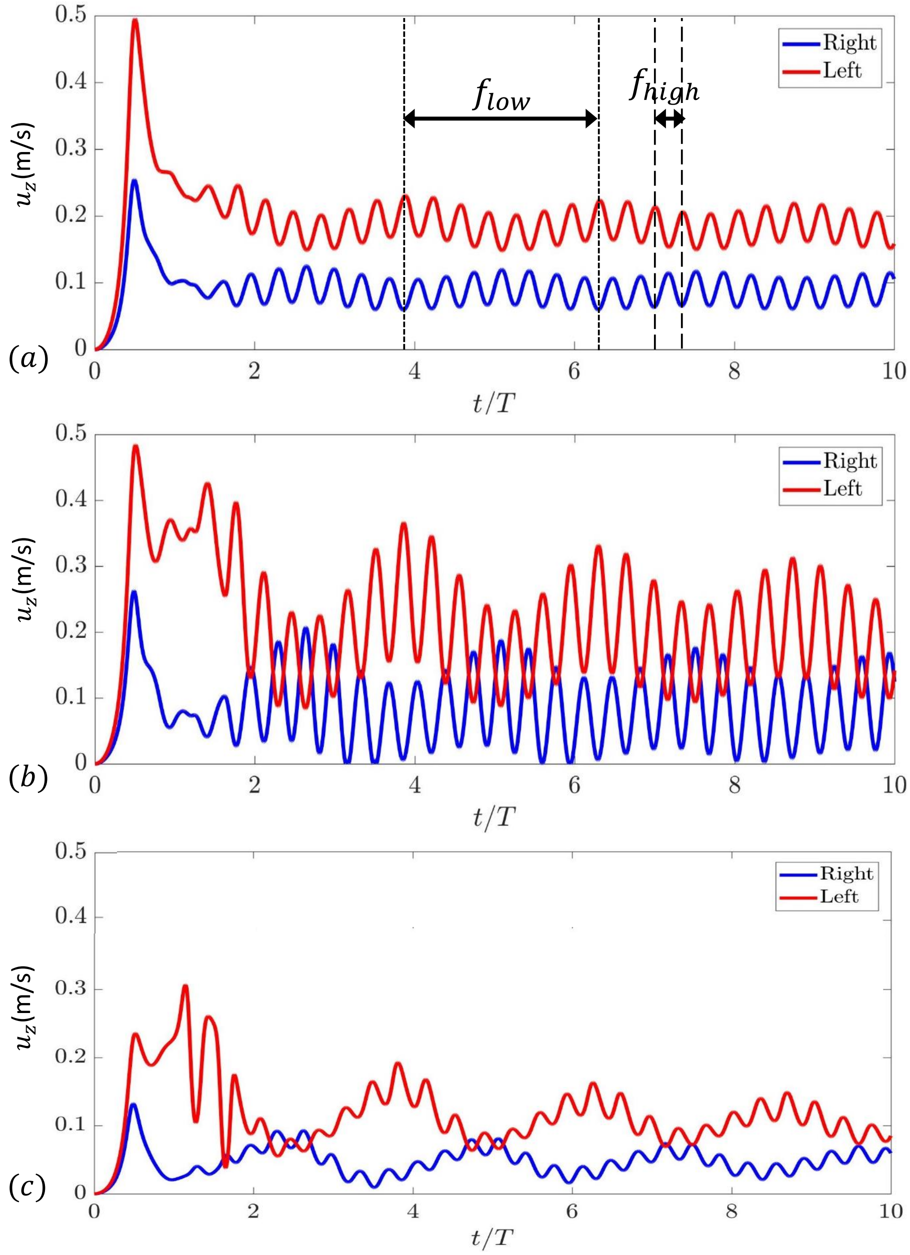

Figure 4.4: Average velocity of the airflow in right side and left side of the elastic column at **a**. $L/3$, **b**. $2L/3$, and **c**. L distances measured from the bottom of the channel. Arrows and dash lines show the period of low and high-frequency oscillations. Parameters are $K_G = 0.1$, $Re = 100$, $m = 850$, and $\chi = 0.5$. Time is scaled by $T = L/V$.

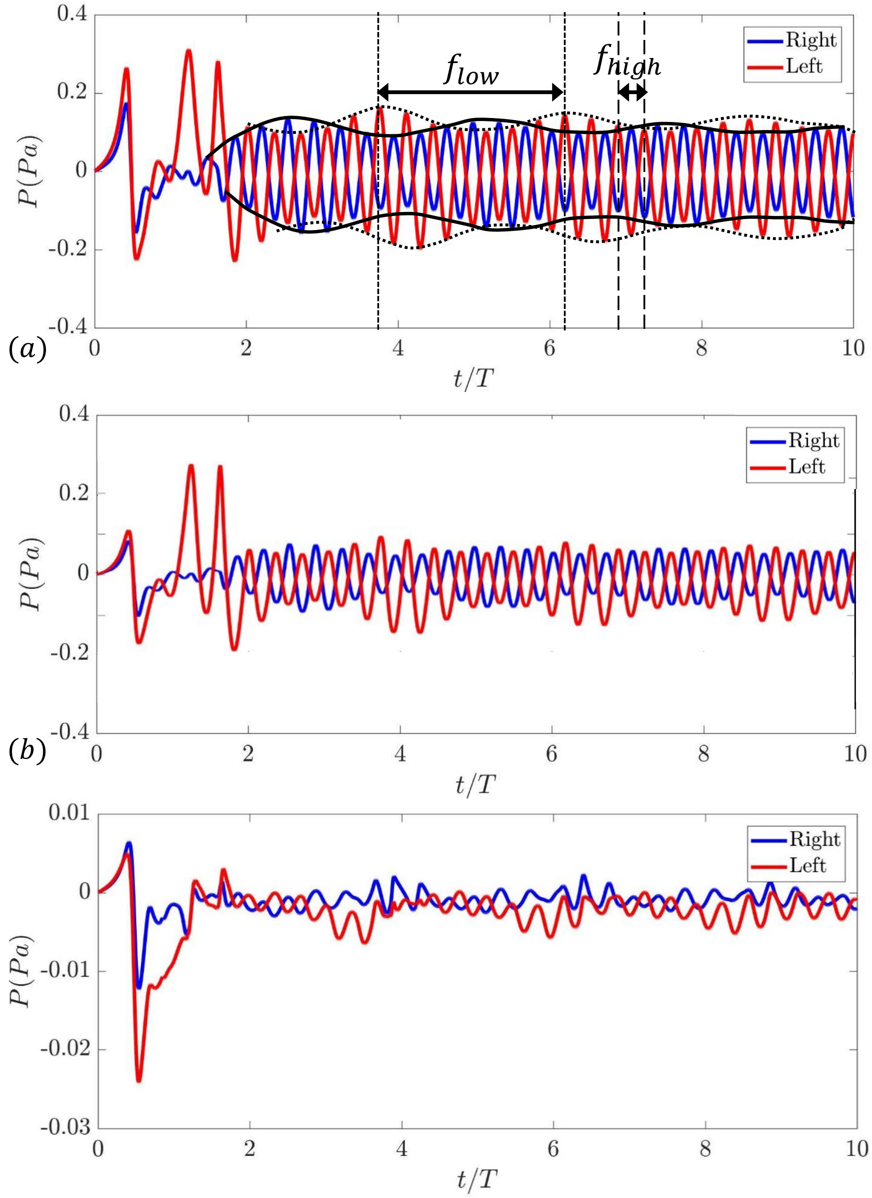

Figure 4.5: Pressure variations of the airflow in right and left sides of the elastic column at **a**. $L/3$, **b**. $2L/3$, and **c**. L distances measured from the bottom of the channel. The solid and dashed black lines present the pressure envelopes at the right and left the side of the channel, respectively. Arrows and straight dash lines show the period of low and high-frequency oscillations.

4.2.2 Parametric study

Similar to forcing eccentricity e defined in Chapter 2, velocity ratio $\chi = V_R/V_L$ is a metric for the 2D asymmetry of the flow adjacent to both sides of the elastic column. Reynold's number Re is a metric for the available kinetic energy transferred to the column by the imposed gas flow. The Bending rigidity K_G is a metric for the importance of spring stiffness of the column compared to the dynamic pressure of the flow, and density ratio m defines the inertia of the column. In this section, we study the sensitivity of column response to these non-dimensional variables. To this end, in the following figures, we change one of the variables and hold the rest fixed.

Velocity ratio (χ):

In this set of simulations non-dimensional parameters are as $K_G = 1$, $Re = 1000$, $m = 850$, and we change velocity ratio between 0.3, 0.5, and 0.7. Note that $\chi = 1$ is equivalent to symmetric forcing, and as $\chi \to 0$ represents greater asymmetric forcing. Figure 4.6 a. shows column top displacement. There is only a low-frequency oscillation observed in displacement time series. By decreasing χ, the amplitude of oscillation increases, but its frequency is not affected. Decreasing χ causes the column to bend further to the left, and the center of the oscillation moves further to the left side of the column.

Figure 4.6 b. shows flow velocity variations and Fig 4.6 c. shows flow pressure variations at distance of $2L/3$ from the bottom of the channel. Velocity time series show that by decreasing χ, the flow variation at two sides of the column increases, and the flow becomes more asymmetric.

High frequency and low-frequency oscillation are observed at both velocity and pressure time series. Similar to high-frequency oscillation, the amplitude of low-frequency oscillation increases by decreasing the velocity ratio χ while its frequency is intact.

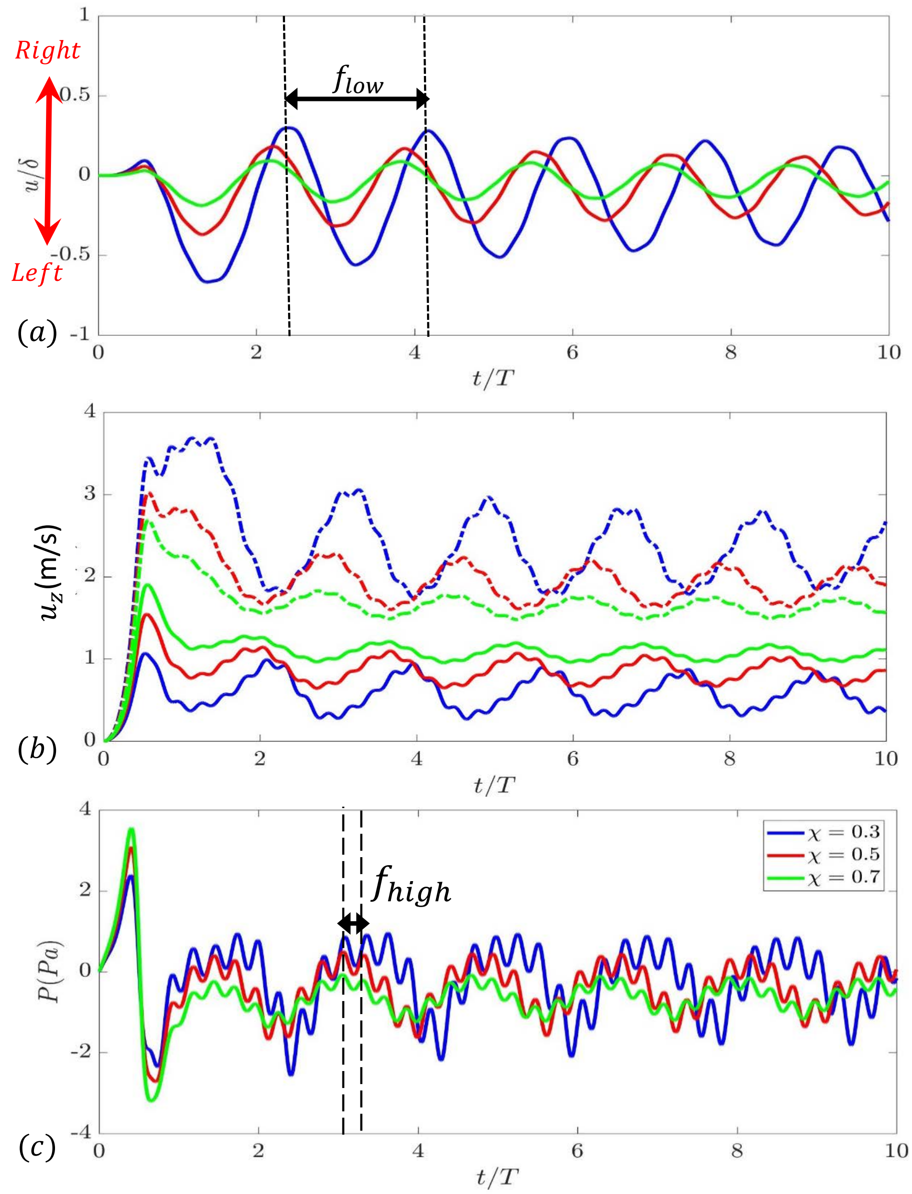

Figure 4.6: **a**.Top displacement of the column, **b**. average flow velocity, and **c**. pressure variation of the flow in the right channel at $2L/3$ from the bottom of the channel. Dashed lines in **b**. represent velocity at the left channel. Arrows and dash lines show the period of low and high-frequency oscillations. Non-dimensional parameters for these simulations are $K_G = 1$, $Re = 1000$, $m = 850$, and χ changes for each simulation. Time is scaled by $T = L/V$.

Reynolds number Re:

In this set of simulations non-dimensional parameters are as $\chi = 0.1$, $K_G = 1$, $m = 1000$, and we change flow Reynold's number Re between 10, 100, and 1000. Figure 4.7 a. shows column top displacement. We observe low-frequency oscillations in all three displacement time series, and the amplitude of the oscillation increases by increasing the Reynolds number. Also, the period of low-frequency oscillation slightly increases by increasing the Re number.

Figure 4.7 b. shows flow velocity variations and Fig 4.7 d. shows flow pressure variations at distance $2L/3$ from the bottom of the channel. We magnified velocity time series of cases with $Re = 10$ and $Re = 100$ by $100\times$ and $10\times$, respectively, for visibility purposes. Also, pressure time series of cases with $Re = 10$ and $Re = 100$ are magnified by $10^4\times$ and $100\times$, respectively. The amplitude of oscillation for both high and low-frequency oscillations in velocity and pressure time series increase by increasing Reynolds's number. The period of high-frequency oscillations does not vary by varying Reynolds number, while the period of low-frequency oscillation gradually increases by increasing Reynolds number.

Bending rigidity K_G:

In this set of simulations non-dimensional parameters are as $\chi = 0.1$, $Re = 1000$, $m = 1000$, and we change bending rigidity K_G between 1, 4, and 10. Figure 4.8 a. shows column top displacement. Cases with smaller bending rigidity bend further, and the amplitude of oscillation increases by decreasing bending rigidity K_G. In the displacement time series, high-frequency oscillation is only observed when $K_G = 1$, and the period of low-frequency oscillations, broadly consistent with the results and analysis in Chapter 3. In addition to these spectral results, however, the amplitude of the oscillations declines with increasing K_G as well as their amplitude decrease by increasing K_G.

Figure 4.8 b. shows flow velocity and Fig 4.8 d. shows flow pressure variations at a distance of $2L/3$ from the bottom of the channel. The am-

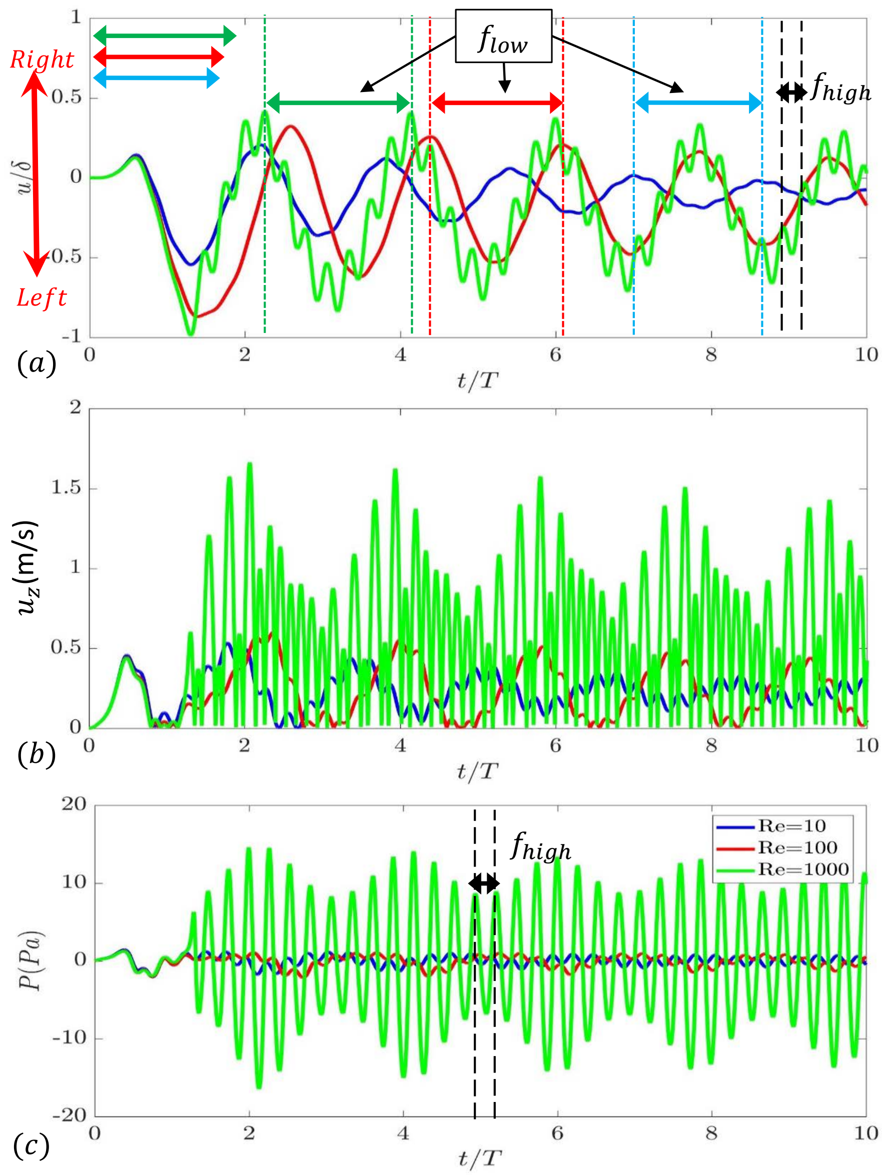

Figure 4.7: **a**.Top displacement of the column, **b**. average flow velocity, and **c**. pressure variation of the flow in the right of the channel at $2L/3$ from the bottom of the channel. Parameters are $K_G = 1$, $\chi = 0.1$, $m = 1000$, and for different Re. Arrows and dash lines show the period of low and high-frequency oscillations. Flow velocity is magnified $100\times$ and $10\times$ for $Re = 10$ and $Re = 100$, respectively. Pressure variations for $Re = 10$ and $Re = 100$ is $10^4\times$ and $100\times$ magnified, respectively.

plitude and period of both low and high-frequency oscillations decrease by increasing bending rigidity. For the case with $K_G = 10$, still, high-frequency oscillations does not occur.

To be consistent with the our high De experiments and to capture the high Ω limit identified in §3.5.3, We investigate the column response with a $K_G < 1$ and ideally $K_G \ll 1$. However, in these limits, large column accelerations cause the column to interact with the walls over time scales that are sufficiently small to lead to the growth challenging numerical instabilities (violations of the CFL condition). One way to slow the growth rate of these instabilities and enable at least a qualitative exploration of this limit is to reduce Re to 1. Figure 4.9 shows a simulation where corresponding non-dimensional parameters are as $\chi = 0.9$, $Re = 1$, $m = 100$, and $K_G = 0.01$. In contrary to all previous simulations, the amplitude of the oscillation in column top displacement as well as in pressure and velocity variations increase over time.

Density ratio m:

In this set of simulations non-dimensional parameters are as $K_G = 1$, $Re = 1000$, $\chi = 0.5$, and we change density ratio between 300, 600, and 850. Figure 4.10 a. shows column top displacement. We observe that decreasing m causes the column to bend further to the left, and the center of the oscillation moves further to the left side of the column (toward greater average flow velocity). The period of low-frequency oscillations increases by decreasing the density ratio as simulation with $m = 850$ has the shortest period, and $m = 300$ has the longest period. In the displacement time series, high-frequency oscillations are much more significant when the density ratio decreases.

Figure 4.10 b. shows flow velocity, and Fig 4.10 d. shows flow pressure variations at a distance of $2L/3$ from the bottom of the channel. We observe that high-frequency oscillations are with the same period for all three cases, while by increasing density ratio, the amplitude of oscillation decreases.

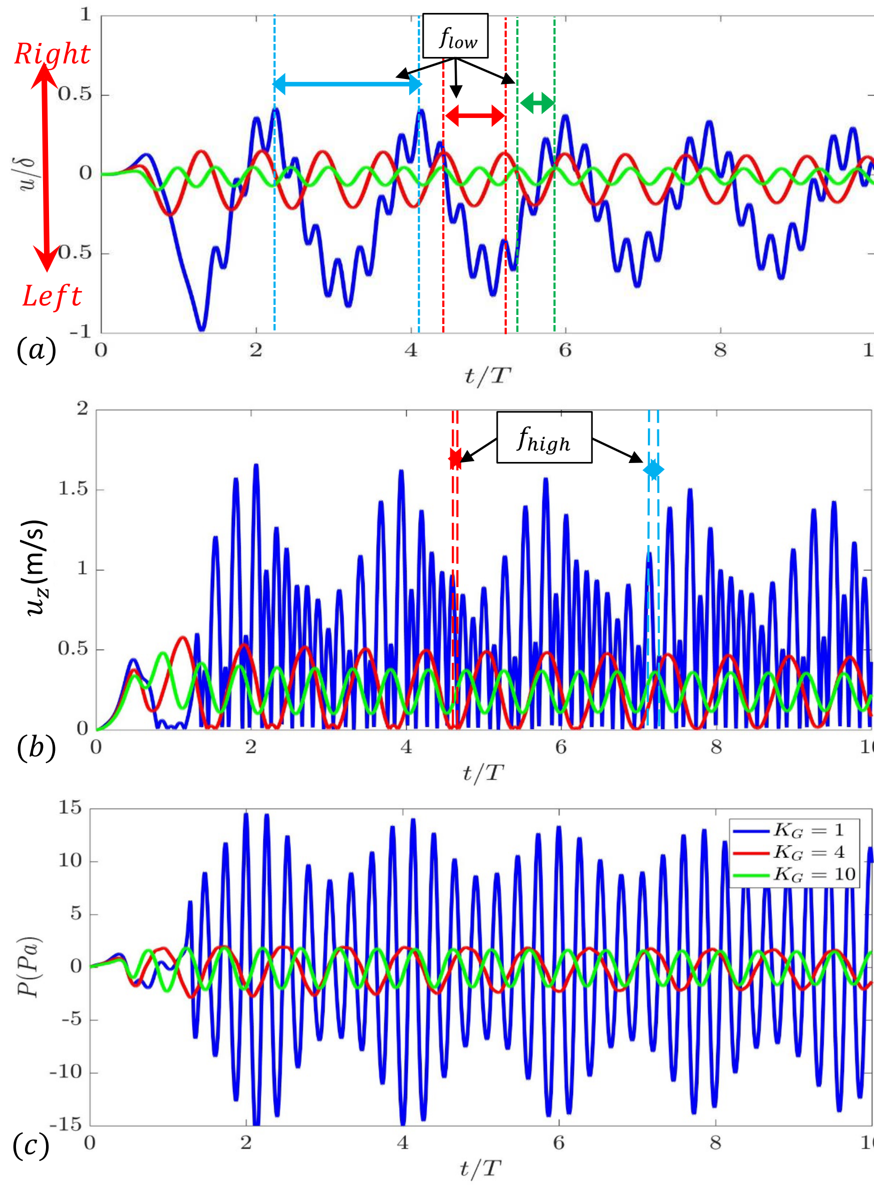

Figure 4.8: **a**.Top displacement of the column, **b**. average flow velocity, and **c**. pressure variation of the flow in the right channel at $2L/3$ from the bottom of the channel. Arrows and dash lines show the period of low and high-frequency oscillations. Non-dimensional parameters for these simulations are $\chi = 0.1$, $Re = 1000$, $m = 1000$, and K_G changes for each simulation. Time is scaled by $T = L/V$.

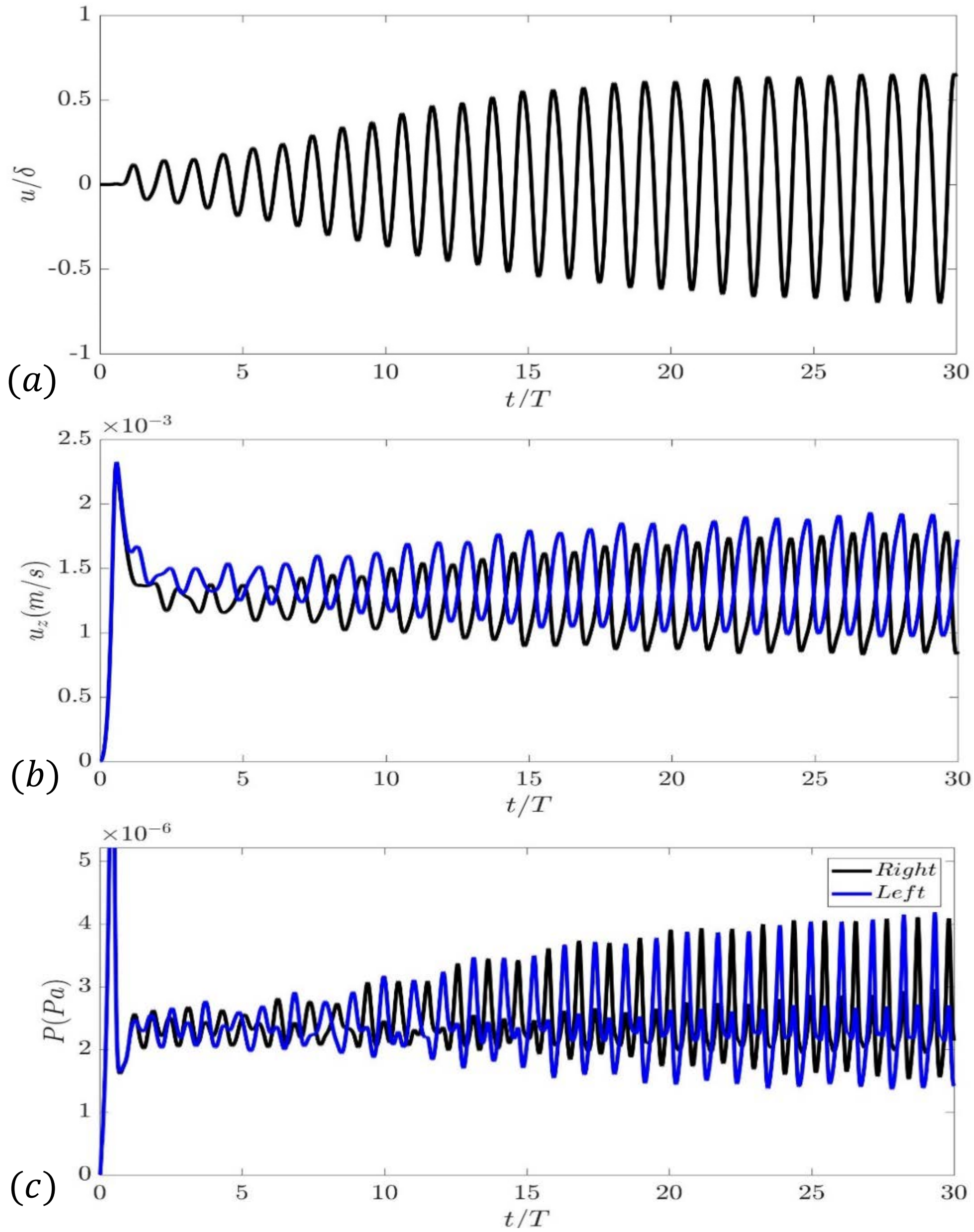

Figure 4.9: **a**.Top displacement of the column, **b**. average flow velocity, and **c**. pressure variation of the flow in the right channel at $2L/3$ from the bottom of the channel. Non-dimensional parameters for these simulations are $\chi = 0.9$, $Re = 1$, $m = 100$, and $K_G = 0.01$. Time is scaled by $T = L/V$.

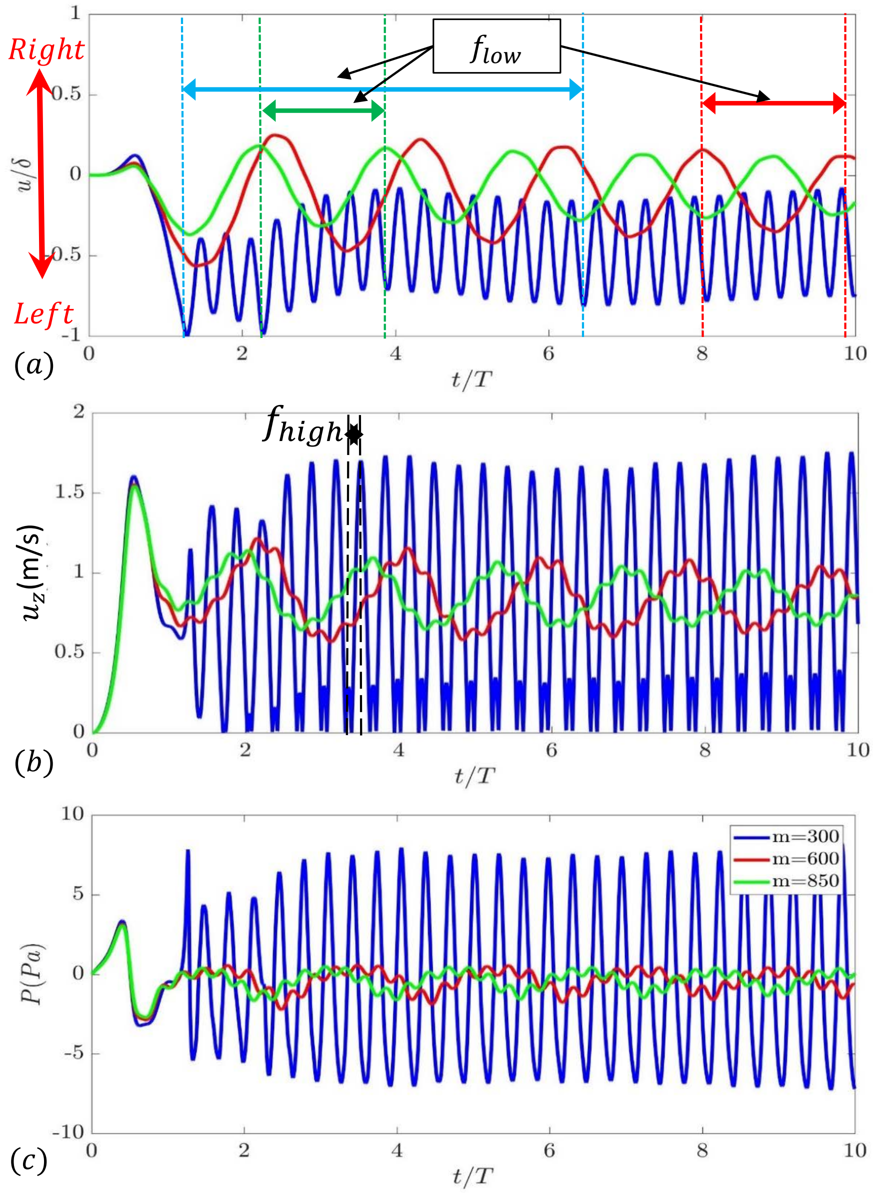

Figure 4.10: **a**.Top displacement of the column, **b**. average flow velocity, and **c**. pressure variation of the flow in the right channel at $2L/3$ from the bottom of the channel. Arrows and dash lines show the period of low and high-frequency oscillations. Non-dimensional parameters for these simulations are $K_G = 1$, $Re = 1000$, $\chi = 0.5$, and m changes for each simulation. Time is scaled by $T = L/V$.

4.3 Discussions and summary

In this discussion we first overview the response of an elastic column regarding to different dimensionless control parameters we defined at the beginning of this chapter. We then address: **i**. when do both high-frequency wagging and low-frequency Bernoulli mode appear?; **ii**. how can we relate the 2D numeric solution to the experiments in terms of different class of responses?

4.3.1 Overview

In this chapter, we studied the response of an elastic column to parallel flow in a channel with a Cartesian geometry as an approximation to our experiments. We first introduce four governing dimensionless parameters using the equation of motion for the elastic column and Navier-Stokes equations in the fluid flow. Then, we investigate how these parameters affect the column response using a case study and parametric studies.

Through varied case studies, (Figs.4.3–4.5) we observe that the elastic column oscillates with two distinct frequencies provided $K_G \leq 1$. In contrast to the experiments, whereas high-frequency oscillations correspond to the natural frequency of the column and low-frequency oscillation, which corresponds to Bernoulli's effect of the flow adjacent to the column. Simulation results show that Bernoulli modes will always occur with the existence of flow adjacent to the column. In contrast, high-frequency wagging mode is not always observed. Dimensional analysis of equation 4.2 shows that the column's period of oscillation grows with $\propto \sqrt{1/K_G}$. When K_G increases, frequency of high-frequency oscillations increases, and higher amount of energy is required to excite the oscillation. As a result, the mechanical energy transferred from low-frequency Bernoulli mode to high-frequency wagging mode has to be large enough to be able to excite wagging. Based on our simulations, lowering the column's bending rigidity ($K_G \downarrow$), increasing the flow Reynolds number ($Re \uparrow$), increasing flow asymmetry ($\chi \to 0$), and decreasing the mass ratio between column and the flow ($m \downarrow$) can increase the chance of wagging modes to occur.

In more details, we investigate Velocity ratio χ, Reynold's number Re, bending rigidity K_G, and density ratio between column and gas m. Velocity ratio $\chi = V_R/V_L$ is a metric that shows the asymmetric of the flow adjacent to the elastic column. Based on our definition, when $\chi = 1$ flow is distributed evenly adjacent to the column, and the most asymmetric flow is when $\chi = 0$. Varying velocity ratio χ does not change the frequency of high-frequency or low-frequency oscillations but decreasing velocity ratio χ, enhancing the flow asymmetric, cause the amplitude of both oscillations to increase, see Fig.4.6.

Investigation of Reynolds number Re, which is a metric for the available kinetic energy in the flow to be transferred to the elastic column, shows that period of high-frequency oscillations does not change by varying Reynolds number while its amplitude increase if Reynolds number increases. On the other hand, not only the amplitude of low-frequency oscillation does increase with increasing Reynolds number, but also the period of the low-frequency oscillation increases with increasing Reynolds number, see Fig.4.7.

Increasing density ratio m causes the period of low-frequency oscillation to decrease, but the period of high-frequency oscillations are constant. And the amplitude of both low and high-frequency oscillations increases when density ratio decreases, see Fig. 4.8.

Bending rigidity K_G represents the ratio of elastic stresses in the column to dynamic pressure in the flow. Consistent with the discussion and analysis in §3.5.3, we find bending rigidity to be the only parameter that affects periods of both low and high-frequency oscillation. Increasing bending rigidity reduces the period and amplitude of low and high-frequency oscillations in the displacement time series as well as in velocity and pressure variations, see Fig. 4.8.

Whereas the natural high-frequency oscillations of wagging are excited for $K_G \leq 1$ and are insensitive to all other parameters, the lower frequency Bernoulli mode depends on all the dimensionless parameters, and just its variation with the velocity ratio χ is negligible. Dimensional analysis of equation 4.2 and equation 4.9 shows that the time scale of elastic column displacement and fluid flow variations is a function of Re, K_G, and m.

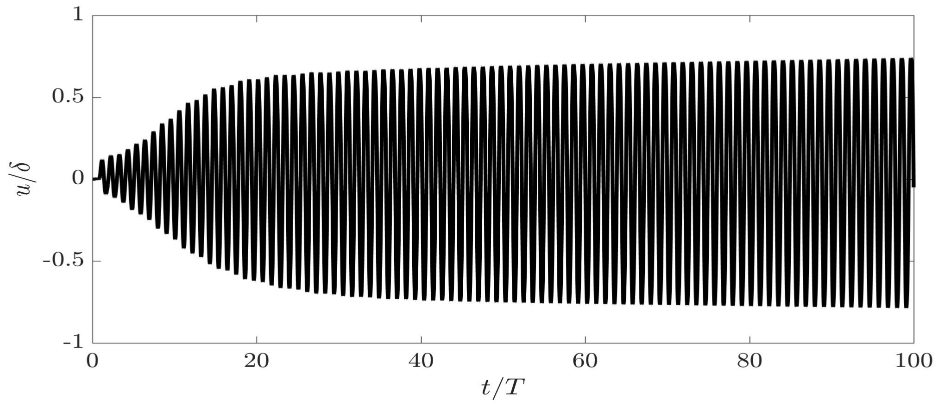

Figure 4.11: Top displacement of the column. Non-dimensional parameters for this simulation are $K_G = 0.01$, $Re = 1$, $\chi = 0.9$, and $m = 100$.

4.3.2 The relation between the 2D numeric solution and experiments in terms of different class of responses:

As we discussed in Chapter 3, a rotational response can occur in a high De limit or equivalently where $\Omega \gg 1$ (or $K_G \ll 1$). In this condition the column accelerates and oscillation continues. While in low De airflow ($\Omega \ll 1$) oscillation is a superposition of a series of arbitrary free oscillation and cause a chaotic solution.

From the simulations, although the Bernoulli mode excites a high-frequency oscillation where $K_G = 1$, we observe that the only case that amplitude of the oscillation increases (column accelerates) over time is when $K_G = 0.01$ ($\Omega = 100$). Figure 4.11 shows the top displacement of the column for a simulation with $K_G = 0.01$, $Re = 1$, $\chi = 0.9$, and $m = 100$ for a longer time than in Fig. 4.9. In this case, the amplitude of oscillation increases for the whole simulation. This case can potentially refer to a rotational response as the flow is approximately symmetric ($\chi = 0.9$), the amplitude of the column displacement is nearly equal at both sides of the channel, and most important, oscillation is growing not damping.

Chapter 5

Implication for Real Volcanoes

Bercovici et al. [6] and Liao et al. [26] have shown that there is a correlation between column displacement inside a volcano and corresponding seismic tremors. Assuming that the magma column inside the volcano oscillates with one of the rotational, mixed-mode, or chaotic responses, the related tremor would have different seismic signatures. If there are a series of seismometers installed around a volcanic vent with the same radial distance, and the magma column is in a rotational mode, received tremor signals could be correlated to each other with a constant lag [26]. If the magma column is in a mixed-mode response, seismic signals could be correlated with varying time lags in time. During a chaotic response, tremor will be observed with transient periods of spatial correlation across the vent.

Figure 5.2 shows how forcing exerted to a magma column inside an active volcano can evolve from a constant and initially low eccentricity through a range of $e - De$ conditions with pre-eruptive gas pressurization and through the eruption itself. Initially, Degassing through the annulus is plausibly slow and uniformly distributed around the column (see Figs. 1.2 and 5.1) long times before an eruption happens.Gas flow forcing is at the low eccentricity indicated, and small Deborah number, $De \rightarrow 0$. Consequently, the magma column is expect to oscillate in a chaotic mode with progressive gas-

Figure 5.1: Some snapshots of observed gas ring at the edge of Karymsky volcano. Captured from https://www.newsflare.com/video/227079/weather-nature/magnificent-ash-plumes-at-russias-karymsky-volcano

pressurization. Degassing becomes more intense over time. Increasing gas flow rate causes Deborah number to increase, $De \uparrow$, with the eccentricity unchanged. Through this evolution, column displacements transition smoothly into mixed mode. Transient spatial correlations in seismic signals of wagging across as well as around the volcanic event emerge and become more frequent as an eruption approaches. As degassing rates increase towards a pre-eruptive maximum, De becomes large and column displacements will enter an increasingly rotational regime. As a result, tremors become correlated azimuthally, and a constant lag at different directions around the volcanic vent can be observed.

The smooth evolution at constant e changes with the first explosions that destroy parts of the annulus locally. The resulting spatial heterogeneity in permeability causes asymmetry in the gas flux thus e to increase. In addition to natural wagging frequencies becoming spatially variable (see Chapter 1), the spatially complex gas flux forcing of these modes will drive wagging into a chaotic mode. Consequently, the correlation between tremor signals decreases and finally disappears.

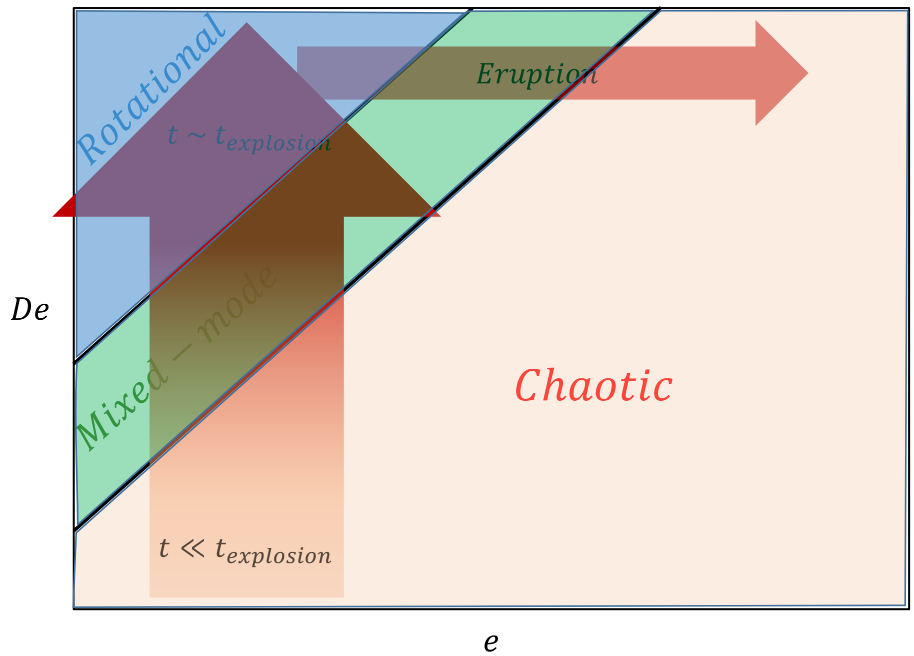

Figure 5.2: Volcano's activity in eccentricity e, Deborah De number regime. A long time before the eruption, ($t \ll t_{explosion}$, volcanic degassing is inefficient, $De \approx 0$, and degassing is uniform, $e \approx 0$. Closer to eruption time, degassing enhances, $De \uparrow$, while annulus structure does not change. Eventually, enhancing degassing causes bubbles strain rate to increases above a critical strain rate, and fragmentation and explosion occur. Fragmentation and explosion cause annulus to become heterogeneous and lead to non-uniform degassing around the volcano, $e \to 1$. Each colored area corresponds to the ideal condition for one of the rotational, mixed-mode, or chaotic regimes based on the results in Chapter 3.

Chapter 6

Concluding Remarks and Future Research Directions

This thesis has investigated magma wagging model experimentally and numerically. The experimental setup and results are in Chapter 2 and Chapter 3, which studied Bernoulli mode and three distinct oscillation responses. Numerical modeling and results are presented in Chapter 4, which investigated Bernoulli and wagging modes in depth. These results are summarized first in §6.1. Secondly, we discuss some limitations of the approach in the thesis, together with possible means of improvement (§6.2). The thesis closes with suggestions for future research directions in this area (§6.3).

6.1 Summary

In this work, in Chapter 1 we have reintroduced magma wagging model studied in [6, 21, 26]. The main control parameters of the model, see equation (1.6, are as following; the ratio of hydrostatic and dynamic gas pressure γ, the ratio of magma and gas densities β, ratio of the annulus thickness to the magma column width λ, and the ratio of viscous forces arising in the magma column to the gas spring force in the annulus η.

In Chapter 2 & Chapter 3, we have studied magma wagging model experimentally to verify that the proposed mechanism of theory is a complete description of the phenomena. Critically, to investigate whether the long period Bernoulli mode can continuously drive the predicted magma wagging. Also, experimental studies can help to identify new modes of oscillation including torsional and lateral wagging modes.

We have introduced Deborah number De through equation 2.35 which is a metric of airflow forcing in our experiments. Also, Deborah number is related to rate of available energy in the airflow to the rate of dissipation of energy in the column. It is analogues to η and captures the basic mechanical properties of magma wagging model.

The other important feature that the experiments investigate is the distribution of non-uniform gas flux around the column. The non-uniform gas flux is related to explosion and fragmentation. The fragmentation modifies the annulus structure and changes permeability of the annulus. We extend the model by introducing heterogeneous gas flux around the column. We have defined forcing eccentricity e, equation 2.34, as the parameter for characterizing the asymmetry of the airflow around the column.

We have used energy components of the trajectory of top of the column to characterize the response of the elastic column to airflow forcing by using dimensionless energy ratio ER equation 2.49. Then, we have mapped the experimental results on a $De-e$ parameter space and investigate the favorite conditions for each of the rotational, mixed-mode, and chaotic responses.

In Chapter 4, we have studied magma wagging numerically in a 2D Cartesian geometry. We have derived the control parameters of Re, m, and K_G, through governing equations of solid and fluid domains. We have extended the study by adding velocity ratio χ between average flow speed at two sides of the column as a metric similar to forcing eccentricity e to the problem. We then investigate the column response to variety of control parameters in terms of frequency and amplitude of the oscillation.

Here are the main conclusion from our study:

Experimental results:

- Displacements in the unforced damping regime confirm essential spectral predictions made by [21] and [6] that wagging oscillation occurs with an amplitude that declines over time scale of T_d. These experiments also show that the preferred mode of unforced oscillation is a rotational displacement.

- During steady-state regime, there is a relatively high frequency Bernoulli mode which occurs along with lower frequency wagging. Mechanical energy is transferred from high frequency Bernoulli mode to lower frequency wagging to sustain oscillations through a reverse energy cascade.

- Rotational responses in a symmetric airflow forcing $e = 0$ with high De, and in damping regime, confirms qualitatively the model presented by Liao et al.[26] that column goes under different whirling motions.

- Rotational modes only occur with symmetric airflow $e \to 0$ for strong gas forcing, high De, where flow timescale is shorter than column response time ($\Omega \gg 1$) and column accelerates.

- We extend the predicted motion by [26] for a symmetric airflow $e = 0$ and find new classes of chaotic and mixed-mode responses corresponding to low and intermediate De, respectively.

- Chaotic responses with $e = 0$ and low De are a consequence of **i**. lack of total kinetic energy to stabilize the massive column into rotational, or **ii**. larger flow timescale than column reaction time scale leads to a series of arbitrary free oscillation. The superposition of these arbitrary free oscillations will be a chaotic response.

- When airflow eccentricity increases as $e \to 1$, trajectories become increasingly chaotic, and rotational responses are impossible where $e > 0.5$.

- Chaotic responses for $e > 0.5$ are driven by lateral strong pressure gradients or non-zero net pressure forces related to these boundary conditions. Non-zero net pressure forces or lateral pressure gradients drive linear motions that perturb displacements that are otherwise rotational.

Numerical results:

- A relatively low frequency Bernoulli mode is observed that provides the energy for higher frequency wagging mode (energy cascade from lower frequency to higher frequency oscillations, similar to predictions in Bercovici et al.[6]).

- The frequency of the wagging mode is only a function of column properties (K_G) and wagging frequency increases by increasing K_G.

- The amplitude of the wagging mode depends on coupled physics of fluid flow and solid mechanics. By lowering the column's bending rigidity ($K_G \downarrow$), increasing the flow Reynolds number ($Re \uparrow$), increasing flow asymmetry ($\chi \to 0$), and decreasing the mass ratio between the column and the flow ($m \downarrow$) the amplitude of wagging increases.

- Low frequency Bernoulli mode is a function of coupled physics between fluid flow and the elastic column. Increasing Re, decreasing K_G, and decreasing m cause the the frequency of Bernoulli mode to increase.

- Simulations with very small K_G (equivalent to very large Ω) confirms that the acceleration can occur in column displacement and probably lead to a rotational solution.

6.2 Limitations of the experiments

Analog experiments of magma wagging are challenged by scaling issues we discuss in Chapter 2. Although we have made several advances doing the experiments and numerical modelings, we must also acknowledge some improvements that can be added:

- The permeable vesicular annulus can vary in space, particularly during an eruption. We modeled this heterogeneity with imposing asymmetric airflow, however, the elasticity of the column is assumed homogeneous.

This assumption is not necessarily correct and non-homogeneous elastic property can be included in the model. It can affect the spring forcing which results in different wagging frequency.

- A potential weakness is that the column is viscoelastic in our experiments and more likely viscoplastic in real life with elasticity on the outside. However, the magma column can be modeled as a highly viscous fluid encircled by an elastic layer. This design leads to another control parameter, viscosity of the fluid, which can be easily adjusted.

- The magma column buoyancy forces are not included in the original model, while it has influenced our experiments as we observed some unexpected behaviors, see more details in §3.5.4. Similar to our experiments that the column wants to bend because of the gravity, magma column wants to spread out into the annulus. This problem can be investigated in more details.

6.3 Future research directions: exploring volcano seismic data

This study can be extended to a real volcano by testing the predictions made in Chapter 5. If there is a well instrumented volcano to monitor tremor activity, received tremor signals can be studied and correlation between them can be monitored. For example, there are a series of seismic stations around the crater of Redoubt volcano. And the tremor signals related to recent activities are available from these station. Bercovici et al.[6] studied the tremor signals measured at two station across the Redoubt vent prior to its 2009 eruption and showed that the signals are out of phase by approximately half the dominant oscillation period. Later, Liao et al.[26] studied the cross correlation between the tremor signals from pairs of stations around Redoubt vent and suggested a circular wagging that can explain the observed radiation pattern.

As an extension to these studies, the evolution of magma column motion at early stages of volcanic activity, prior to the eruption, and during the eruption can be investigated through studying the correlation of tremor signals around an active volcano. If tremor signal are correlated between stations with a constant time lag, the magma column is wagging in rotational mode. Columns wagging in the mixed-mode response will be characterized by transient correlated tremor among stations with time-varying time lags. Chaotic wagging is characterized by no correlation of tremor signals among different stations.

Bibliography

[1] K. Aki and R. Koyanagi. Deep volcanic tremor and magma ascent mechanism under Kilauea, Hawaii. *J. Geophys. Res.*, 86(B8):7095, 1981. → page 2

[2] N. S. Bagdassarov, D. B. Dingwell, and S. L. Webb. Viscoelasticity of crystal- and bubble-bearing rhyolite melts. *Phys. Earth Planet. Inter.*, 83(2):83–99, 1994. → page 7

[3] C. K. Batchelor and G. K. Batchelor. *An Introduction to Fluid Dynamics*. Cambridge University Press, 2000. → page 45

[4] C. F. Beards. *Engineering Vibration Analysis with Application to Control Systems*. Elsevier, 1995. → page 76

[5] J. P. Benoit and S. R. McNutt. New constraints on source processes of volcanic tremor at arenal volcano, costa rica, using broadband seismic data. *Geophys. Res. Lett.*, 24(7194):449–452, 1997. → pages 2, 15

[6] D. Bercovici, A. M. Jellinek, C. Michaut, and D. C. Roman. Volcanic tremors and magma wagging: gas flux interactions and forcing mechanism. *Geophys. J. Int.*, 195(2):1001–1022, 2013. → pages iii, xiii, xiv, 5, 7, 10, 11, 12, 13, 14, 15, 16, 17, 18, 22, 44, 74, 96, 100, 102, 103, 104

[7] B. A. Chouet. Long-period volcano seismicity: its source and use in eruption forecasting. *Nature*, 380(6572):309–316, 1996. → pages 2, 4

[8] L. Collier, J. W. Neuberg, N. Lensky, V. Lyakhovsky, and O. Navon. Attenuation in gas-charged magma. *J. Volcanol. Geotherm. Res.*, 153 (1-2):21–36, 2006. → pages xii, 6

[9] R. S. Crosson and D. A. Bame. A spherical source model for low frequency volcanic earthquakes. *J. Geophys. Res.*, 90(B12):10237, 1985. → page 4

[10] R. P. Denlinger and R. P. Hoblitt. Cyclic eruptive behavior of silicic volcanoes. *Geology*, 27(5):459–462, 1999. → page 4

[11] C. Donaldson, C. Caudron, R. G. Green, W. A. Thelen, and R. S. White. Relative seismic velocity variations correlate with deformation at Kīlauea volcano. *Sci. Adv.* , 3(6):e1700219, 2017. → page 9

[12] D. Dzurisin. A comprehensive approach to monitoring volcano deformation as a window on the eruption cycle. *Rev. Geophys.*, 41(1), 2003. → pages 1, 2

[13] J. C. Eichelberger, C. R. Carrigan, H. R. Westrich, and R. H. Price. Non-explosive silicic volcanism. *Nature*, 323(6089):598–602, 1986. → page 5

[14] A. P. French. *Vibrations and Waves.* CRC Press, 2017. → pages 68, 69

[15] H. M. Gonnermann and M. Manga. The fluid mechanics inside a volcano. *Annu. Rev. Fluid Mech.*, 39(1):321–356, 2007. → pages xii, 6, 9

[16] A. Goto. A new model for volcanic earthquake at Unzen Volcano: Melt Rupture Model. *Geophys. Re. Lett.*, 26(16):2541–2544, 1999. → page 4

[17] M. T. Gudmundsson, R. Pedersen, K. Vogfjörd, B. Thorbjarnardóttir, S. Jakobsdóttir, and M. J. Roberts. Eruptions of Eyjafjallajökull Volcano, Iceland. *EOS, Trans. American Geophys. Union*, 91(21):190, 2010. → page 1

[18] M. Hellweg. Physical models for the source of Lascar's harmonic tremor. *J. Volcanol. Geotherm. Res.*, 101(1):183 – 198, 2000. → page 4

[19] R. E. Holasek, S. Self, and A. W. Woods. Satellite observations and interpretation of the 1991 Mount Pinatubo eruption plumes. *J. Geophys. Res.: Solid Earth*, 101(B12):27635–27655, 1996. → page 1

[20] A. J. Hotovec, S. G. Prejean, J. E. Vidale, and J. Gomberg. Strongly gliding harmonic tremor during the 2009 eruption of Redoubt Volcano. *J. Volcanol. Geotherm. Res.*, 259:89–99, 2013. → pages xi, 2, 3

[21] A. M. Jellinek and D. Bercovici. Seismic tremors and magma wagging during explosive volcanism. *Nature*, 470(7335):522–525, 2011. → pages iii, xii, 4, 5, 6, 7, 9, 10, 17, 22, 44, 74, 100, 102

[22] J. B. Johnson and J. M. Lees. Plugs and chugs-seismic and acoustic observations of degassing explosions at Karymsky, Russia and Sangay, ecuador. *J. Volcanol. Geotherm. Res.*, 101(1-2):67–82, 2000. → pages xiii, 4, 15, 16

[23] C. Klug and K. V. Cashman. Permeability development in vesiculating magmas: implications for fragmentation. *Bull. Volcanol.*, 58(2-3):87–100, 1996. → pages xii, 6

[24] K. I. Konstantinou and V. Schlindwein. Nature, wavefield properties and source mechanism of volcanic tremor: a review. *J. Volcanol. Geotherm. Res.*, 119(1-4):161–187, 2003. → page 2

[25] R. C. Leet. Saturated and subcooled hydrothermal boiling in groundwater flow channels as a source of harmonic tremor. *J. Geophys. Res.: Solid Earth*, 93(B5):4835–4849, 1988. → page 4

[26] Y. Liao and D. Bercovici. Magma wagging and whirling: excitation by gas flux. *Geophys. J. Int.*, 215(1):713–735, 2018. → pages iii, xiv, xv, 17, 19, 20, 21, 22, 45, 96, 100, 102, 104

[27] Z. Lu and D. Dzurisin. Ground surface deformation patterns, magma supply, and magma storage at okmok volcano, alaska, from InSAR analysis: 2. coeruptive deflation, july–august 2008. *J. Geophys. Res.*, 115, 2010. → pages 2, 9

[28] S. R. McNutt. Volcanic seismology. *Annu. Rev. Earth Planet. Sci.*, 33 (1):461–491, 2005. → page 2

[29] S. R. McNutt and T. Nishimura. Volcanic tremor during eruptions: Temporal characteristics, scaling and constraints on conduit size and processes. *J. Volcanol. Geotherm. Res.*, 178(1):10–18, 2008. → page 2

[30] P. A. Nadeau, J. L. Palma, and G. P. Waite. Linking volcanic tremor, degassing, and eruption dynamics via SO_2 imaging. *Geophys. Res. Lett.*, 38(1):L01304, 2011. → pages xiv, 15, 17

[31] J. Neuberg. Characteristics and causes of shallow seismicity in andesite volcanoes. *Phil. Trans. Math. Phys. Engin. Sci.*, 358(1770): 1533–1546, 2000. → page 2

[32] S. Okumura, M. Nakamura, and A. Tsuchiyama. Shear-induced bubble coalescence in rhyolitic melts with low vesicularity. *Geophys. Res. Lett.*, 33(20), 2006. → page 5

[33] S. Okumura, M. Nakamura, A. Tsuchiyama, T. Nakano, and K. Uesugi. Evolution of bubble microstructure in sheared rhyolite: Formation of a channel-like bubble network. *J. Geophys. Res.*, 113 (B7), 2008. → page 5

[34] A. C. Rust, N. J. Balmforth, and S. Mandre. The feasibility of generating low-frequency volcano seismicity by flow through a deformable channel. *Geol. Soc. Lond. Spec. Publ.*, 307(1):45–56, 2008. → page 4

[35] R. S. J. Sparks. Dynamics of magma degassing. *Geol. Soc. Lond. Spec. Publ.*, 213(1):5–22, 2003. → pages 2, 5

[36] H. Tuffen, R. Smith, and P. R. Sammonds. Evidence for seismogenic fracture of silicic magma. *Nature*, 453:511–514, 2008. → page 9

[37] K. Unglert and A. M. Jellinek. Feasibility study of spectral pattern recognition reveals distinct classes of volcanic tremor. *J. Volcanol. Geotherm. Res.*, 336:219–244, 2017. → page 2

[38] S. R. Young, R. S. J. Sparks, W. P. Aspinall, L. L. Lynch, A. D. Miller, R. E. A. Robertson, and J. B. Shepherd. Overview of the eruption of Soufriere Hills Volcano, Montserrat, 18 July 1995 to December 1997. *Geophys. Res. Lett.*, 25(18):3389–3392, 1998. → page 1